# Interactive chemistry in the Laboratoire de Météorologie Dynamique general circulation model: Description and background tropospheric chemistry evaluation

D. A. Hauglustaine,[1] F. Hourdin,[2] L. Jourdain,[3] M.-A. Filiberti,[4] S. Walters,[5] J.-F. Lamarque,[5] and E. A. Holland[5]

Received 7 July 2003; revised 11 December 2003; accepted 29 December 2003; published 26 February 2004.

[1] We provide a description and evaluation of LMDz-INCA, which couples the Laboratoire de Météorologie Dynamique general circulation model (LMDz) and the Interaction with Chemistry and Aerosols (INCA) model. In this first version of the model a $CH_4-NO_x-CO-O_3$ chemical scheme representative of the background chemistry of the troposphere is considered. We derive rapid interhemispheric exchange times of 1.13–1.38 years and 0.70–0.82 years, based on surface and pressure-weighted mixing ratios of inert tracers, respectively. The general patterns of the nitrogen deposition are correctly reproduced by the model. However, scavenging processes remain a major source of uncertainty in current models, with convective precipitation playing a key role in the global distribution of soluble species. The global and annual mean methane (7.9 years) and methylchloroform (4.6 years) chemical lifetimes suggest that OH is too high by about 19–25% in the model. This disagreement with previous estimates is attributed to the missing nonmethane hydrocarbons in this version of the model. The model simulates quite satisfactorily the distribution and seasonal cycle of CO at most stations. At several tropical sites and in the Northern Hemisphere during summer, the OH overestimate leads, however, to a too intense CO chemical destruction. LMDz-INCA reproduces fairly well the distribution of ozone throughout most of the troposphere. A main disagreement appears in the Northern Hemisphere upper troposphere during summer, due to a too high tropopause in the GCM. When the GCM winds are relaxed toward assimilated meteorology, a much higher variability is obtained for ozone in the upper troposphere, reflecting more frequent stratospheric intrusions. The stratospheric influx of ozone increases from 523 Tg/yr in the base case simulation to 783 Tg/yr in the nudged version. *INDEX TERMS:* 0322 Atmospheric Composition and Structure: Constituent sources and sinks; 0365 Atmospheric Composition and Structure: Troposphere—composition and chemistry; 0368 Atmospheric Composition and Structure: Troposphere—constituent transport and chemistry; *KEYWORDS:* global modeling, tropospheric ozone budget, climate-chemistry interactions

**Citation:** Hauglustaine, D. A., F. Hourdin, L. Jourdain, M.-A. Filiberti, S. Walters, J.-F. Lamarque, and E. A. Holland (2004), Interactive chemistry in the Laboratoire de Météorologie Dynamique general circulation model: Description and background tropospheric chemistry evaluation, *J. Geophys. Res.*, *109*, D04314, doi:10.1029/2003JD003957.

## 1. Introduction

[2] On the basis of the most recent estimates, the radiative forcing of climate associated with increasing greenhouse gas concentration in the atmosphere since preindustrial times totals 2.78 $W/m^2$ on a global and annual mean basis [*Ramaswamy et al.*, 2001]. About half of this forcing is associated with carbon dioxide ($CO_2$) concentration increase. The other half of the radiative forcing is attributed to methane ($CH_4$), nitrous oxide ($N_2O$), halocarbons ((H)CFCs), and tropospheric ozone ($O_3$) increase due to anthropogenic activities and directly involves atmospheric chemistry through the destruction or production of these radiatively active species. The recent simulations performed with global climate models clearly indicate that all anthropogenic forcings, including well-mixed greenhouse gases, tropospheric ozone, stratospheric ozone, direct and indirect aerosol forcings, have to be accounted for in order to

[1]Laboratoire des Sciences du Climat et de l'Environnement, Gif-sur-Yvette, France.
[2]Laboratoire de Météorologie Dynamique, Université de Paris 6, Paris, France.
[3]Service d'Aéronomie, Université de Paris 6, Paris, France.
[4]Institut Pierre Simon Laplace, Université de Paris 6, Paris, France.
[5]National Center for Atmospheric Research, Boulder, Colorado, USA.

Copyright 2004 by the American Geophysical Union.
0148-0227/04/2003JD003957$09.00

reconstruct the observed global temperature change since the nineteenth century [*Tett et al.*, 2002; *Hansen et al.*, 2002].

[3] Ozone absorbs both shortwave and longwave radiation and contributes directly to the radiative budget of the atmosphere [*Lacis et al.*, 1990; *Hauglustaine et al.*, 1994]. Recent work estimates a direct contribution of tropospheric $O_3$ to the anthropogenic radiative forcing of 0.35 W/m$^2$, or 18% to the aforementioned total greenhouse forcing since preindustrial times [*Ramaswamy et al.*, 2001]. In addition to that, as a primary source of the main oxidizing radicals (OH, O($^1$D)), ozone plays a key role in atmospheric chemistry by controlling the residence time in the atmosphere of the main greenhouse gases such as $CH_4$, $N_2O$, and HCFCs, and hence providing indirect radiative forcings of climate [*Prather et al.*, 2001; *Ramaswamy et al.*, 2001]. Ozone is produced in the troposphere during the oxidation of $CH_4$, carbon monoxide (CO) and nonmethane hydrocarbons (NMHCs) in the presence of nitrogen oxides ($NO_x$ = NO + $NO_2$) and sunlight. These ozone precursors (CO, $NO_x$, NMHCs) which have small direct radiative forcings [*Sinha and Toumi*, 1996; *Highwood et al.*, 1999; *Solomon et al.*, 1999] are therefore viewed as indirect climate gases through ozone formation in the troposphere and impact on OH [*Fuglestvedt et al.*, 1999].

[4] Because of limited available observations, estimates of tropospheric ozone distribution, budget, time evolution, and associated radiative forcing of climate have often relied on global three-dimensional (3-D) Chemical-Transport Models (CTMs) [e.g., *Müller and Brasseur*, 1995; *Berntsen et al.*, 2000; *Lelieveld and Dentener*, 2000; *Wang and Jacob*, 1998; *Hauglustaine and Brasseur*, 2001]. These CTMs are driven by meteorology provided either by their parent General Circulation Model (GCM) [e.g., *Brasseur et al.*, 1998a; *Wang et al.*, 1998] or issued from assimilated meteorological fields [e.g., *Berntsen and Isaksen*, 1997; *Lawrence et al.*, 1999; *Law et al.*, 1998; *Bey et al.*, 2001; *Horowitz et al.*, 2003]. Several studies have suggested the significant role played by climate changes (i.e., temperature, winds, water vapor) on tropospheric ozone and radicals and on their time evolution [*Brasseur et al.*, 1998b; *Stevenson et al.*, 2000; *Johnson et al.*, 2001; *Zeng and Pyle*, 2003], and also the importance of interannual variability of atmospheric dynamics and in particular of its internal oscillation modes (NAO, ENSO) on the distribution of pollutants and their export out of source regions [*Chandra et al.*, 1998; *Li et al.*, 2002]. These studies clearly emphasize the strong coupling existing between atmospheric composition and climate-dynamical processes.

[5] In order to further investigate the coupling between climate and chemistry, to account for atmospheric composition changes in GCMs, and conversely to account for the impact of climate and dynamical changes on atmospheric composition, atmospheric chemistry has been introduced on-line in GCMs. This effort has been initiated for the stratosphere and the study of polar ozone chemistry, which provides a prominent example of chemistry-climate coupling [*Austin et al.*, 2001; *Rasch et al.*, 1995; *Shindell et al.*, 1998; *Dameris et al.*, 1998; *Nagashima et al.*, 2002]. Recently, this on-line coupling between climate models and chemistry has been extended to the troposphere. The first simulations were limited to a few year duration with no feedback of tropospheric composition on climate [*Roelofs and Lelieveld*, 1995]. However, more recent work has reported multidecadal simulations with interactively calculated ozone fields used in the GCM radiation code [*Mickley et al.*, 1999; *Shindell et al.*, 2001]. A similar approach has also been adopted to calculate interactively sulfate and other aerosols in GCMs [*Feichter et al.*, 1996; *Roelofs et al.*, 1998; *Koch et al.*, 1999; *Rasch et al.*, 2000; *Boucher and Pham*, 2002].

[6] In order to investigate the impact of atmospheric composition changes due to anthropogenic activities on climate and how climate changes can in turn dampen or amplify the chemical perturbations, we have developed the need in our institute for a coupled climate-chemistry model. This modeling system should account for long-lived greenhouse gases, tropospheric and stratospheric ozone chemistry, and the different types of aerosol on-line in a coupled atmosphere-ocean-biosphere GCM. An additional prerequisite was the option to drive the model with assimilated meteorological fields in order to allow the evaluation of calculated composition and aerosols fields against observations for a specific period of time, as well as for interpretation or support for large-field campaigns or satellite data.

[7] In this study, we present this new climate-chemistry model. The development of this model involved the Laboratoire de Météorologie Dynamique GCM (LMDz) adapted for the transport of species by *Hourdin and Armengaud* [1999], and the newly developed chemistry and aerosol model Interaction with Chemistry and Aerosols (INCA).

[8] For this first version of the model, we focus our attention on the $CH_4-NO_x-CO-O_3$ photochemistry in the troposphere. No interactive coupling between chemistry and climate are currently considered. This paper provides a description and a general evaluation of the model. It is intended to provide a reference for the simulation of transport and mixing in the LMDz GCM and the background for other ongoing studies involving more elaborated versions of INCA including NMHCs, aerosols, and stratospheric chemistry.

## 2. Model Description

### 2.1. LMDz General Circulation Model

#### 2.1.1. Model Framework

[9] LMDz is a grid point global climate model initially described by *Sadourny and Laval* [1984] and evaluated, for instance, by *Le Treut and Li* [1991] and *Harzallah and Sadourny* [1995]. The model has been used for a large number of sensitivity experiments including changes in solar insolation [*Nesmes-Ribes et al.*, 1993], $CO_2$ doubling [*Le Treut et al.*, 1994], ozone perturbation [*Chalita et al.*, 1996], and sulfate aerosol forcing [*Le Treut et al.*, 1998]. The GCM constitutes the atmospheric component of the IPSL Earth system model recently used for long-term integrations by *Dufresne et al.* [2002] and *Friedlingstein et al.* [2001].

[10] The dynamical part of the code is based on a finite-difference formulation of the primitive equations. The equations are discretized on a staggered latitude-longitude Arakawa C-grid. The dynamical code has been widely used not only for the Earth atmosphere but also for the numerical simulation of the general circulation of other planetary

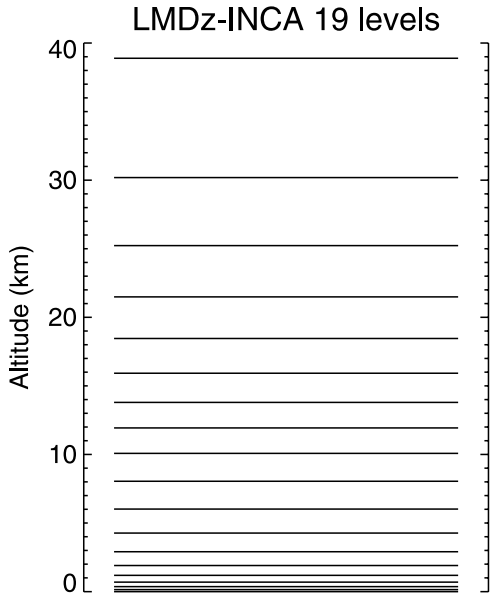


**Figure 1.** Vertical levels in LMDz-INCA.

atmospheres [*Hourdin et al.*, 1993]. The radiative calculation is based on the European Centre for Medium-Range Weather Forecasts (ECMWF): a refined version of the scheme developed by *Fouquart and Bonnel* [1980] in the solar part of the spectrum and by *Morcrette* [1991] in the thermal infrared. In this version of the GCM, the surface conditions over land are treated using a simple bucket parameterization for soil moisture. The monthly mean sea-surface temperatures and sea-ice coverage are prescribed according to the GISST data described by *Rayner et al.* [1996].

[11] A major improvement of the LMDz GCM is its newly implemented capability to simulate the on-line atmospheric transport of species. The large-scale advection of all tracers (including vapor and liquid water) is calculated on the basis of the finite-volume second-order scheme proposed by *Van Leer* [1977] as described by *Hourdin and Armengaud* [1999]. Deep convection is parameterized according to the scheme of *Tiedtke* [1989] and the turbulent mixing in the planetary boundary layer is based on a local second-order closure formalism. The model has been used recently by *Boucher et al.* [2002] and *Boucher and Pham* [2002] for simulation of the sulfur cycle. The model has also been used for the transport of inert tracers by *Hourdin and Issartel* [2000] with winds and temperature relaxed toward ECMWF reanalysis (nudging). The relaxation of the GCM winds toward ECMWF meteorology is performed by applying a correction term to the GCM winds according to

$$\frac{\partial X}{\partial t} = G\left(X^{\star} - X\right), \tag{1}$$

where $X$ is the model nudged variable (u and v), $X^{\star}$ the ECMWF reanalysis, and $G$ the relaxation coefficient fixed to $6.67 \times 10^{-3}$ s$^{-1}$ (corresponding to a relaxation time of 2.5 h) for both variables and over the whole model domain. The ECMWF fields are provided every 6 hours and interpolated onto the LMDz grid. In this study, we present the results obtained with the climatological version of LMDz. However, in order to illustrate the impact of different wind fields on the distribution of species, the simulated ozone profiles from the climatological and nudged versions of the GCM will be compared.

[12] The LMDz version (referred to as 3.3) implemented in this study has an horizontal resolution of 3.8 degrees in longitude and 2.5 degrees in latitude (96 × 72). On the vertical, the model uses σ-p coordinates with 19 levels extending from the surface up to about 3 hPa (Figure 1). This corresponds to a vertical resolution of about 300–500 m in the planetary boundary layer (first level at 70 m height) and to a resolution of about 2 km at the tropopause (with 7–9 levels located in the stratosphere). The primitive equations in the GCM are solved with a 3 min time step, large-scale transport of species is performed every 15 min, and physical processes (including unresolved subgrid-scale mixing) are calculated with a time step of 30 min.

#### 2.1.2. Transport Processes

[13] In this section, and before any chemical application is undertaken with this newly developed model, we use several tracers to evaluate the model horizontal and vertical transports. Different tracers are used in order to allow comparison with previous modeling work and intercomparison exercises. In particular, we use fossil fuel $CO_2$, $SF_6$, CFC11 and $^{85}$Kr, all of them having primarily Northern Hemisphere sources and a long residence time, to test horizontal and interhemispheric transport. In addition to that, $^{222}$Rn is used to test the vertical transport and the convection in the model. As done for the other tracers and for water vapor, these tracers are introduced on-line in LMDz-INCA.

##### 2.1.2.1. $CO_2$

[14] *Rayner and Law* [1995] have summarized the results of the first TRANSCOM intercomparison exercise aiming at evaluating the large-scale and subgrid-scale transports of 12 global models in the case of $CO_2$ like tracers. In our study, we focus on the fossil fuel $CO_2$ experiment. The fossil fuel emissions for $CO_2$ are taken from the EDGAR v3.2 emission database [*Olivier and Berdowski*, 2001]. These emissions are representative of the year 1995 and total 6.4 PgC/yr. These emissions are spatially distributed in the model according to EDGAR with no seasonality. As for the other tracers included in the model, LMDz-INCA has been run for a total of 25 years with constant emissions and the last year of integration is used for this evaluation. Figure 2 shows the zonal and annual mean $CO_2$ surface mixing ratio calculated with LMDz-INCA together with the envelope provided by the 12 models from TRANSCOM. As in the study by *Rayner and Law* [1995], the results are normalized to correct from drift in the global mean caused by slight differences in the experimental set-up and remove the effect of the initial conditions. It was chosen to normalize the mixing ratio by the global mean and pressure-weighted mixing ratio for January. In the Southern Hemisphere, LMDz-INCA provides a gradient similar to the other models. In the Northern Hemisphere, LMDz-INCA generally gives mixing ratios at the lower range of the TRANSCOM results, indicating a smaller interhemispheric gradient and a more efficient atmospheric transport. The interhemispheric difference calculated at the surface with LMDz-INCA is 2.9 ppmv. This value can be compared with

the 2.35–4.72 ppmv range provided by TRANSCOM. On the basis of the model results *Rayner and Law* [1995] have calculated, the interhemispheric exchange time as a measure of large-scale transport. The exchange time is defined as the difference between the mean mixing ratio in the Northern and Southern Hemisphere boxes divided by half the difference in source strength between them. On the basis of the surface mean mixing ratio, the calculated exchange time from TRANSCOM lies in the range 1.06–2.14 years. With LMDz-INCA, we derive an exchange time of 1.128 years. This number shows a small interannual variability, ranging from 1.106 to 1.145 years over the last 5 years of the simulation. Two experiments have been performed to investigate the sensitivity of the interhemispheric exchange time to subgrid-scale mixing. When convective mixing is suppressed the exchange time increases to a value of 1.256 years, a 11% increase. In this case, the zonal mean mixing ratio increases slightly in source regions (Figure 2). When boundary layer mixing is suppressed, the exchange time increases by more than a factor of 2 to a value of 2.370 years. The zonal mean mixing ratio increases from 4 ppmv in the reference case to more than 10 ppmv in source regions. This extreme experiment emphasizes the major role played by boundary layer mixing on the export of pollutants from midlatitude regions. It also suggests that a large fraction of the spread reported in the TRANSCOM results is associated with the parameterization of mixing in the global models.

#### 2.1.2.2. $SF_6$

[15] Sulfur hexafluoride ($SF_6$) is a very long-lived tracer (residence time of 3200 years [*Prather et al.*, 2001]) used in electrical equipment and industry. Since its emissions are purely anthropogenic and mostly located in the Northern Hemisphere, $SF_6$ has been used for evaluating large-scale transport in global models [*Maiss et al.*, 1996; *Levin and Hesshaimer*, 1996; *Denning et al.*, 1999; *Kjellström et al.*, 2000] or derive the age-of-air in the stratosphere [*Waugh et al.*, 1997]. In LMDz-INCA, the $SF_6$ emissions are geographically distributed on the basis of the electrical power usage, and the global mean emission rate is scaled to the 1993 value of 5.686 Gg/yr provided by *Levin and Hesshaimer* [1996]. Additional information is provided in the online auxiliary material[1]. The interhemispheric exchange time (calculated as in the case of $CO_2$ as the difference between the mean mixing ratio in the Northern and Southern Hemisphere boxes divided by half the difference in source strength between them) is 1.19 years based on surface mixing ratios. This value is 20–30% lower than the 1.5–1.7 year range provided by *Levin and Hesshaimer* [1996] and confirms the efficient transport in LMDz. On the basis of pressure-weighted hemispheric mean mixing ratios the exchange time decreases to 0.74 years, a value also 18% shorter than the 0.9 years calculated by *Kjellström et al.* [2000].

#### 2.1.2.3. Krypton 85

[16] This radioisotope is emitted into the atmosphere by nuclear reprocessing plants. Since all known sources are located in the Northern Hemisphere between 33° and 56°, this tracer (mean radioactive lifetime of 15.6 years) has also been used to estimate the interhemispheric transport in the atmosphere and the corresponding exchange time [*Weiss et al.*, 1983; *Jacob et al.*, 1987; *Levin and Hesshaimer*, 1996; *Rind and Lerner*, 1996]. In LMDz-INCA, we distribute the 9 individual emitting plants with the magnitude estimated by *Levin and Hesshaimer* [1996] for the year 1982, with a total emission of 6757 kCi/yr. Figure 3 shows the calculated meridional distribution of $^{85}Kr$ and compares to the measurements reported by *Jacob et al.* [1987] for March and October conditions. As in the study by *Jacob et al.* [1987], the model results are shown for two longitude bands in order to bracket the measurements (i.e., 30W and 7.5W) and are normalized as described in the case of $SF_6$. In March, the interhemispheric difference and latitudinal gradient in the tropics are reasonably well simulated by the model. In October, the steep tropical gradient appears shifted by 10–15 degrees in the model, suggesting a reduced seasonal cycle in the Intertropical Convergence Zone (ITCZ) location in the GCM. The high concentrations measured in October 1983 at 50N are not reproduced in this climatological simulation. On the basis of these calculations we derive an interhemispheric exchange time of 1.38 years based on surface concentrations and corrected from the radioactive lifetime as described by *Jacob et al.* [1987] and *Levin and Hesshaimer* [1996]. On the basis of the pressure-weighted mixing ratio, we calculate an exchange time of 0.82 years. This value is 25% shorter than the 1.1 years derived by *Jacob et al.* [1987] and *Müller and Brasseur* [1995], confirming an efficient large-scale transport and mixing in the GCM.

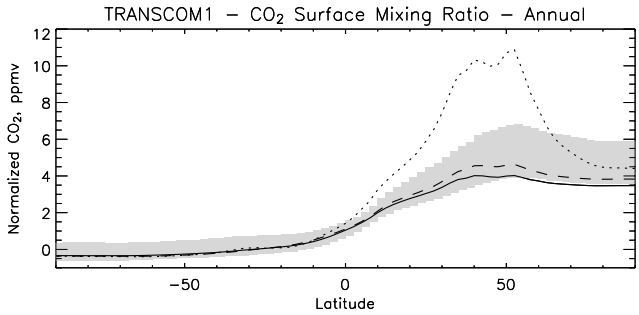


**Figure 2.** Zonal and annual mean normalized $CO_2$ surface mixing ratio (ppmv) calculated in LMDz-INCA (solid line) and envelope of TRANSCOM1 model results (grey area). The LMDz-INCA results are also reported for sensitivity simulations without convective (dashed line) and boundary layer (dotted line) mixing.

#### 2.1.2.4. $CCl_3F$

[17] $CCl_3F$ (CFC-11) has also been used in several GCMs and CTMs to evaluate the transport processes [*Prather et al.*, 1987; *Hartley et al.*, 1994; *Rind and Lerner*, 1996; *Mahowald et al.*, 1997a]. The CFC-11 emissions in LMDz-INCA are distributed according to the EDGAR v2.0 database without seasonal cycle and with a global and annual mean emission of 0.358 Tg/yr representative of 1986. Additional information is provided in the online auxiliary material. On the basis of calculated $CCl_3F$ distributions, we derive in LMDz-INCA an interhemispheric exchange time of 1.16 years based on surface mixing ratios. On the basis of pressure-weighted hemispheric mean mixing ratios we derive an interhemispheric exchange time of 0.70 years, a value to be compared to 0.74 years and 0.58–0.75 years

[1] Auxiliary material is available at ftp://ftp.agu.org/apend/jd/2003JD003957.

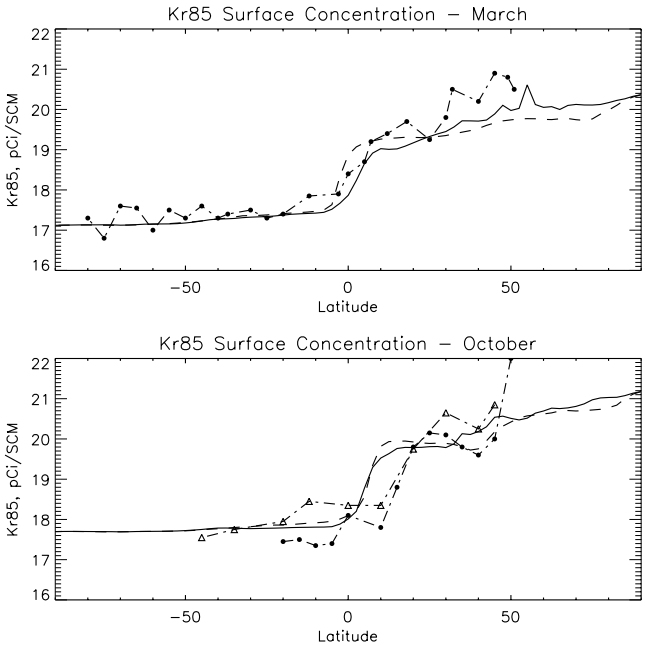


**Figure 3.** Normalized $^{85}$Kr surface concentration (pCi/SCM) calculated in LMDz-INCA at 7.5W (solid line) and 30W (dashed line). (top) March conditions and measurements reported by *Jacob et al.* [1987] for March 1983 (solid circles); (bottom) October conditions and measurements for October 1983 (solid circles) and October 1980 (triangles).

for *Prather et al.* [1987] and *Mahowald et al.* [1997a], respectively.

**2.1.2.5. Radon 222**

[18] $^{222}$Rn is a radioactive isotope which has been used in many transport models to evaluate the synoptic-scale motion and convective mixing [e.g., *Feichter and Crutzen*, 1990; *Jacob and Prather*, 1990; *Genthon and Armengaud*, 1995; *Mahowald et al.*, 1997b; *Rind and Lerner*, 1996; *Jacob et al.*, 1997; *Stevenson et al.*, 1998; *Dentener et al.*, 1999; *Taguchi et al.*, 2002]. This tracer is simulated in LMDz-INCA according to the World Climate Research Program (WCRP) intercomparison exercise reported by *Jacob et al.* [1997]. The emission flux is specified to be 1 atom/cm$^2$/s over land in the latitude band 60N–60S and 0.005 atom/cm$^2$/s over the ocean. The flux is prescribed to be 0.005 atom/cm$^2$/s between 60 and 70 and set to 0 poleward of 70 degrees. The global emission over land is rescaled to a global mean of 72 mol/yr. Radioactive decay occurs with a first-order rate constant $k = 2.1 \times 10^{-6}$ s$^{-1}$. The zonal mean $^{222}$Rn cross-section calculated for June–August and depicted in Figure 4 can be compared to the corresponding results from 14 transport models as illustrated by *Jacob et al.* [1997]. For a sake of comparison with previous work the radon distribution are expressed in units of $10^{-21}$ mol/mol (=1.52 pCi/m$^3$STP). The distribution calculated with LMDz-INCA is in close agreement with the other 3-D models with maximum mixing ratios of 20–30 $\times$ $10^{-21}$ mol/mol at the surface at northern midlatitudes. In the upper troposphere, because of efficient redistribution by convective mixing, maximum mixing ratios of 5 $\times$ $10^{-21}$ mol/mol are calculated at 200 hPa. In contrast, results from the sensitivity experiment performed with suppressed convective mixing shows mixing ratios in this region of about 2 $\times$ $10^{-21}$ mol/mol and higher mixing ratios at the surface reaching 50 $\times$ $10^{-21}$ mol/mol at midlatitudes in the Northern Hemisphere. Boundary layer mixing significantly affects the calculated distribution. When this mixing is suppressed, $^{222}$Rn accumulates at the surface where it reaches more than 100 $\times$ $10^{-21}$ mol/mol. In this

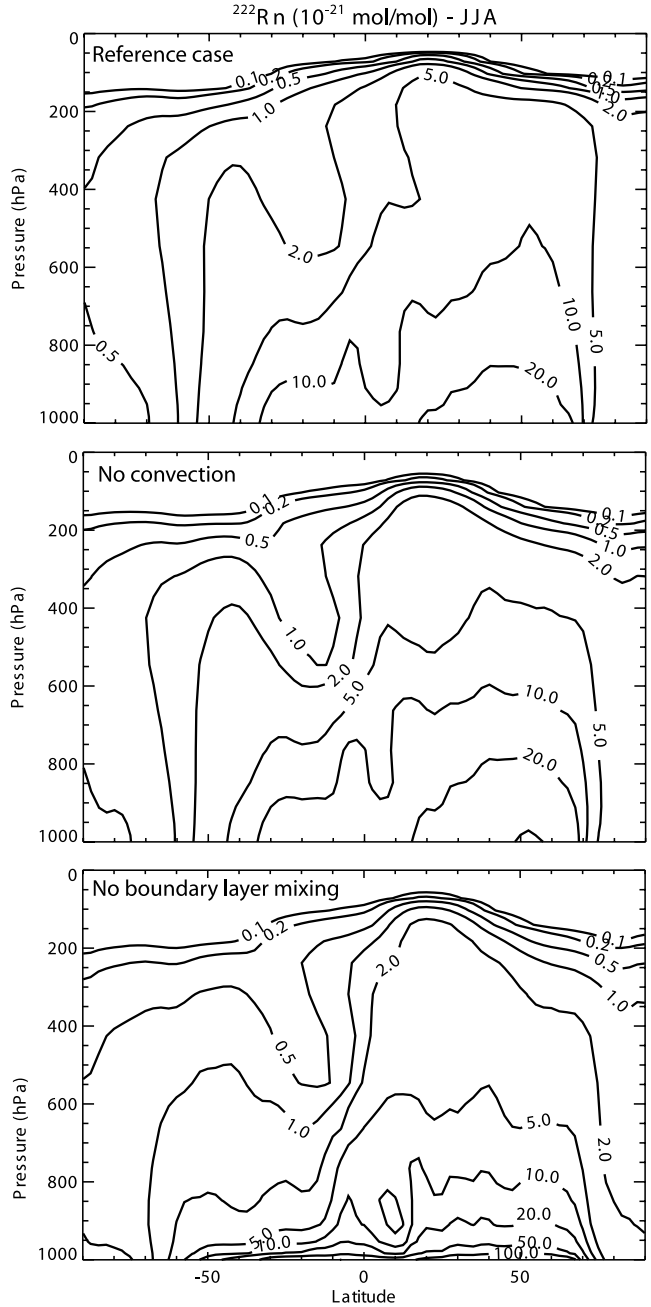


**Figure 4.** Zonal mean radon mixing ratio ($10^{-21}$) calculated by LMDz-INCA for Northern Hemisphere summer conditions (JJA). The distributions are illustrated for the reference simulation (upper panel) and for the cases without convective (middle panel) and boundary layer (lower panel) mixing.

case, the mixing ratio in the upper troposphere is decreased to $0.2 \times 10^{-21}$ mol/mol and $2 \times 10^{-21}$ mol/mol in the Southern and Northern Hemispheres, respectively. Figure 5 compares the simulated $^{222}$Rn surface mixing ratio to climatological measurements at selected marine and continental stations. At remote marine stations (Amsterdam, Dumont d'Urville), the background mixing ratio is generally well reproduced by the model. We note however, as obtained in previous studies [*Genthon and Armengaud*, 1995; *Brasseur et al.*, 1998a; *Taguchi et al.*, 2002], a significant underestimate of $^{222}$Rn during summer at Dumond d'Urville. The $^{222}$Rn mixing ratio is also fairly well simulated at coastal stations or marine stations under continental air influence (Bermuda, Cape Grim, Mace Head). We note, however, that the transport is somewhat overestimated during spring as revealed by the comparison at Mace Head and Bermuda stations. At continental sites the comparison shows that the seasonal cycle is well reproduced at Bombay and Livermore. At Chester, Socorro, and to a lesser extent Livermore, the calculated mixing ratios significantly underestimate the measurements during winter, suggesting too much mixing out of the boundary layer during this period. At the free tropospheric site of Mauna Loa, the calculated seasonal cycle shows a very good agreement in comparison to the observations. However, as obtained by previous work [*Brasseur et al.*, 1996; *Jacob et al.*, 1997; *Taguchi et al.*, 2002], the calculated values underestimate observations during all year. Figure 6 shows the $^{222}$Rn vertical profiles at selected Northern American locations for summer and winter conditions and comparisons with measurements. During summer, the model successfully simulates the measured profiles. In particular, the free tropospheric mixing ratios as well as the apparent boundary layer height are fairly well reproduced at Moffett Field (California). During winter, because of reduced convective mixing, the calculated profiles exhibit a stronger gradient than in summer with lower mixing ratios in the free and upper troposphere. However, the measurements suggest even less mixing and steeper gradient during this season than calculated with the GCM. This feature is consistent with the simulated seasonal cycle at the surface suggesting too much venting out of the boundary layer during this season. Comparison with the profiles simulated with convective or boundary layer mixing removed confirms this finding. A better agreement with the measurements is achieved in winter with suppressed convection and boundary layer mixing. In contrast, mixing is clearly needed to explain the profiles observed in summer. Again, a proper treatment of mixing and in particular of boundary layer mixing appears as a crucial point in global models.

## 2.2. INCA Chemistry and Aerosol Model

[19] Interaction with Chemistry and Aerosols (INCA) is a chemistry and aerosol model introduced on-line in the LMDz general circulation model. INCA is called by the GCM with a time step of 30 min and prepares the surface and in-situ (e.g., lightning) emissions, calculates wet and dry deposition rates and integrates in time the concentration of species to account for atmospheric photochemistry. As used in most CTMs [*Jacob et al.*, 1993; *Müller and Brasseur*, 1995; *Brasseur et al.*, 1998a], a sequential operator approach is adopted in LMDz-INCA. The preprocessor used for INCA is a follow-up of the earlier version of the code developed in the framework of MOZART by *Brasseur et al.* [1998a].

### 2.2.1. Chemistry

[20] In this first version of the INCA model, we use a $CH_4-NO_x-CO-O_3$ chemical scheme representative of the background chemistry of the troposphere. The model calculates the distribution of tropospheric ozone and its precursors as well as the main greenhouse gases and several inert tracers allowing the evaluation of transport and physical processes. The simulated distributions of radiatively active species (i.e., $CH_4$, $N_2O$, (H)CFCs, $O_3$) can then be used in the GCM radiation code in order to calculate the cooling and heating rates and provide a full coupling between chemistry and climate (this option of the model is not activated in the scope of this study). The species considered in this model version are listed in Table 1. As indicated, species with a very short photochemical lifetime are not subject to transport, and only one photochemical family is formed ($O_x = O_3 + O(^1D) + O(^3P)$). A total of 33 species (27 transported species including gas and liquid phase water) is considered in this version of LMDz-INCA.

[21] The chemical scheme used in LMDz-INCA is given in Tables 2, 3, and 4. The scheme includes 19 photolytic reactions (Table 2), 62 gas phase reactions (Table 3) and 4 heterogeneous reactions (Table 4). The reaction rates are specified according to *DeMore et al.* [1997] and subsequent updates [*Sander et al.*, 2000, 2002]. These reaction rates are updated at each model time step on the basis of the temperature, pressure, and water vapor distributions provided by the GCM. Photolysis frequencies $j$ are determined at each time step and model grid-cell on the basis of pretabulated values with a multivariate log-linear interpolation through a Taylor series expansion [*Burden and Faires*, 1985]. This look-up table is prepared with the Troposphere Ultraviolet-Visible (TUV) model (version 4.1) from *Madronich and Flocke* [1997] using a pseudo-spherical 16 stream discrete-ordinate method, 137 spectral intervals and 70 vertical levels. As in the studis by *Müller and Brasseur* [1995] and *Brasseur et al.* [1998a], the clear-sky photodissociation coefficients are tabulated for 18 pressure levels, 7 total ozone columns, 8 solar zenith angles, 4 surface albedo, 3 temperatures at 500 hPa and 2 temperatures at 200 hPa. The surface albedo, temperature and pressure fields are provided by the GCM. The total ozone is based on either prescribed climatologies or the model-calculated ozone fields. The effect of cloudiness on the photolysis frequencies is parameterized according to *Chang et al.* [1987] as described by *Brasseur et al.* [1998a], with cloud fractional cover and liquid water content provided by the GCM at each time step.

[22] Following the recommendations of *Jacob* [2000], four heterogeneous reactions are considered in the chemical scheme. The aerosol distribution is determined on the basis of monthly averaged sulfate fields from *Boucher et al.* [2002]. The aerosol surface density is calculated assuming a log-normal size distribution of dry aerosols in the accumulation mode with a modal radius $r_0 = 0.035 \times 10^{-6}$ m and a geometric standard deviation of 2. We assume an aerosol mass density of $1.780 \times 10^3$ kg/m$^3$ representative of

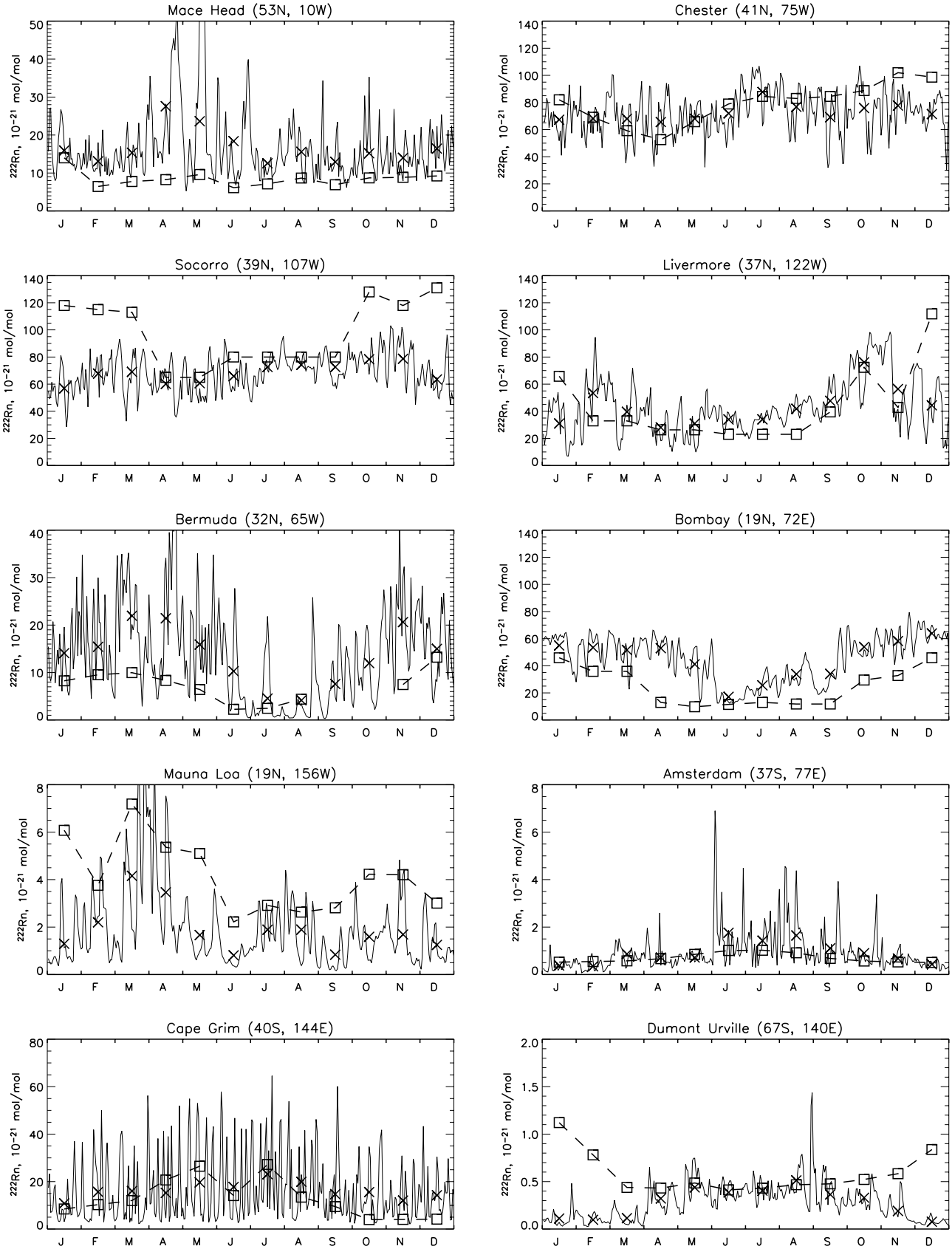


**Figure 5.** Observed (squares) and calculated (solid line is for day-to-day variation, and crosses are for monthly means) seasonal cycle of $^{222}$Rn mixing ratio ($10^{-21}$) at selected stations. Measurements as reported by *Genthon and Armengaud* [1995], *Dentener et al.* [1999], and M. Ramonet (personal communication, 2000).

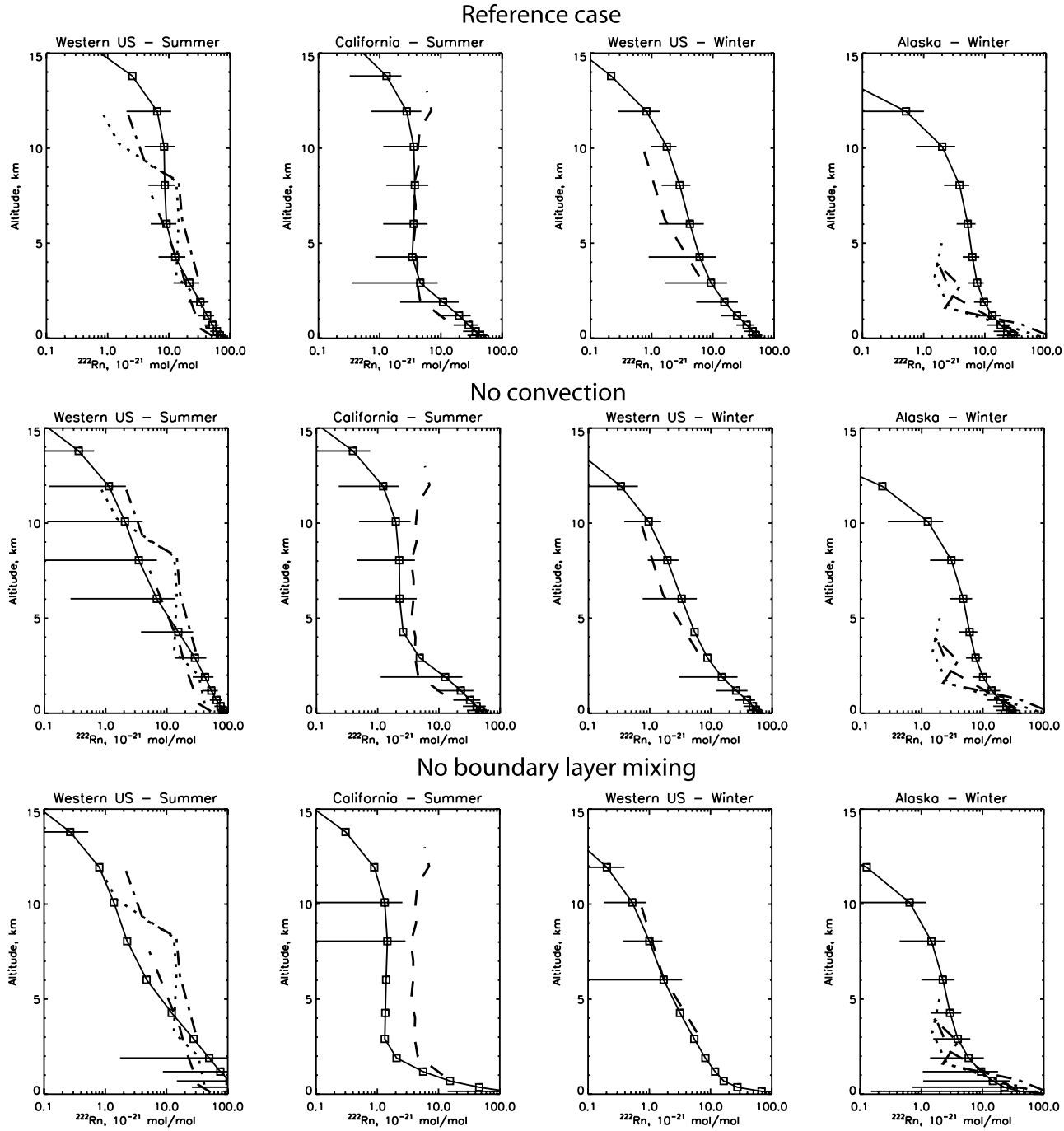


**Figure 6.** Observed (dashed and dotted lines) and calculated (solid lines with squares for monthly mean and 1σ standard deviation) $^{222}$Rn vertical profiles ($10^{-21}$) over the western United States and Alaska during summer and winter. Measurements are taken from *Liu et al.* [1984] and *Kritz et al.* [1998]. The model results are illustrated for the reference simulation (upper panel) and for the cases without convective (middle panel) and boundary layer (lower panel) mixing.

$(NH_4)HSO_4$ [*Boucher and Anderson*, 1995]. At a given relative humidity, a new equilibrium size distribution is recalculated on the basis of *Hänel* [1976]:

$$r = r_0(1 - RH)^{-e_w}, \tag{2}$$

where $r$ is the modal radius of the hydrated aerosol, $RH$ is the relative humidity, and $e_w$ = 0.285. We assume that efflorescence occurs at 35% relative humidity regardless of temperature [*Hess et al.*, 2000]. The reaction rates are calculated using [*Dentener and Crutzen*, 1993]

$$k = \int_r \left(\frac{r}{D_g} + \frac{4}{v\gamma}\right)^{-1} 4\pi r^2 N(r)dr, \tag{3}$$

with $k$ the first-order reaction rate ($s^{-1}$), $D_g$ the gas phase diffusion coefficient ($m^2$/s), $v$ the Boltzman velocity (m/s)

**Table 1.** Trace Gases in LMDz-INCA

| | Species | Transport | Numerical Method |
|---|---|---|---|
| 1 | $H_2O$ (gas phase) | yes | |
| 2 | $H_2O$ (liquid phase) | yes | |
| 3 | $^{222}Rn$ | yes | Euler forward |
| 4 | $^{210}Pb$ | yes | Euler forward |
| 5 | $^{85}Kr$ | yes | Euler forward |
| 6 | $CO_2$ | yes | Euler forward |
| 7 | $SF_6$ | yes | Euler forward |
| 8 | CFC11 | yes | Euler forward |
| 9 | $CH_3CCl_3$ | yes | Euler forward |
| 10 | HCFC22 | yes | Euler forward |
| 11 | $O_x = O(^3P) + O(^1D) + O_3$ | yes | Euler backward |
| 12 | $O_x$ stratosphere | yes | Euler forward |
| 13 | $O_x$ inert | yes | Euler forward |
| 14 | $H_2$ | yes | Euler forward |
| 15 | H | no | Euler backward |
| 16 | OH | no | Euler backward |
| 17 | $HO_2$ | no | Euler backward |
| 18 | $H_2O_2$ | yes | Euler backward |
| 19 | $N_2O$ | yes | Euler forward |
| 20 | N | no | Euler backward |
| 21 | NO | yes | Euler backward |
| 22 | $NO_2$ | yes | Euler backward |
| 23 | $NO_3$ | yes | Euler backward |
| 24 | $HNO_3$ | yes | Euler backward |
| 25 | $HNO_4$ | yes | Euler backward |
| 26 | $N_2O_5$ | yes | Euler backward |
| 27 | $CH_4$ | yes | Euler forward |
| 28 | CO | yes | Euler forward |
| 29 | $CH_2O$ | yes | Euler backward |
| 30 | $CH_3O$ | no | Euler backward |
| 31 | $CH_3O_2$ | yes | Euler backward |
| 32 | $CH_3OH$ | no | Euler backward |
| 33 | $CH_3OOH$ | yes | Euler backward |

calculated on the basis of the considered species molecular mass and local temperature, and $\gamma$ the dimensionless reaction probability. The temperature dependence of the reaction probability of $N_2O_5$ hydrolysis is taken from *Hallquist et al.* [2000]. The resulting zonal and annual mean reaction rate for this heterogeneous reaction is depicted in Figure 7. The reaction rate reaches a maximum of $48 \times 10^{-5}$ $s^{-1}$ in polluted regions at northern midlatitudes and values in the range $2-10 \times 10^{-5}$ $s^{-1}$ in the Southern Hemisphere. Above 500 hPa, the calculated rate is in the range $1-3 \times 10^{-5}$ $s^{-1}$. Because of increasing reaction probability at lower temperatures, a secondary maximum reaching $4 \times 10^{-5}$ $s^{-1}$ is predicted in the upper troposphere. This distribution is generally in line with the earlier results by *Dentener and Crutzen* [1993]. Reaction probabilities used for other reactions are given in Table 4 and are based on *Jacob* [2000] and *Bey et al.* [2001].

[23] The chemical equations are integrated forward in time with a time step of 30 min on the basis of five possible numerical algorithms depending on the considered species: explicit Euler forward [*Brasseur et al.*, 1999], linearized Euler Backward Iterated (EBI) with the Gauss-Seidel scheme [*Shimazaki*, 1985], Quasi-Steady-State Approximation (QSSA) [*Hesstvedt et al.*, 1978], fully implicit Euler backward with Newton-Raphson iteration [*Brasseur et al.*, 1999], and implicit Runge-Kutta (RODAS solver described by *Sandu et al.* [1996]). In the present configuration, long-lived species are integrated with the explicit method and the other species are solved with the implicit Euler backward with Newton-Raphson iteration scheme (Table 1). A convergence check is performed for each grid-cell at each time step.

### 2.2.2. Emissions

[24] Surface emission inventories have been compiled for LMDz-INCA on the basis of various compilations reported on different grids. These compilations are combined, redistributed on the LMDz-INCA grid with a mass preserving algorithm, and rescaled if needed. After interpolation, the emissions are redistributed along the coasts according to the GCM land-sea mask ensuring mass conservation as described by *Gurney et al.* [2000]. For these climatological simulations the emissions are prepared on a monthly mean basis when available. Table 5 summarizes the magnitude of the emissions used for the various species considered in LMDz-INCA.

[25] Anthropogenic emissions (industry, fossil fuel, and industrial biofuel) representative of the year 1995 are based on the EDGAR v3.2 emission database [*Olivier and Berdowski*, 2001]. In the case of CO the global emissions are rescaled to the values given by *Prather et al.* [2000]. Since NMHCs are not included in this version of the model, secondary CO produced by these species is injected directly as a surface source as was done by *Roelofs and Lelieveld* [1995], *Lawrence et al.* [1999], and *Shindell et al.* [2001]. The global amount of secondary CO emitted by anthropogenic NMHCs is taken from *Prather et al.* [2001] and distributed as the EDGAR direct fossil fuel emissions. These emissions are introduced in the model as annual mean without seasonal cycle. In addition to these emissions, $NO_x$ emissions from oceangoing ships are based on *Corbett et al.* [1999] and aircraft $NO_x$ emissions are based on the ANCAT/EC2 inventory [*Gardner et al.*, 1998] and modified to be representative of the year 2000 (D. Lee, personal communication, 2003).

[26] Biomass burning emissions are introduced on the basis of the emission factors compiled for each species by *Andreae and Merlet* [2001] and on the spatial and temporal distribution of the amount of biomass burnt. In the tropics, the biomass burnt by savanna fires, deforestation, agricultural waste burning, and biofuel use are taken from *Hao and*

**Table 2.** Photodissociative Reactions Included in LMDz-INCA

| | Reaction |
|---|---|
| j1 | $O_2 + h\nu \rightarrow O + O$ |
| j2 | $O_3 + h\nu \rightarrow O(^1D) + O_2$ |
| j3 | $O_3 + h\nu \rightarrow O + O_2$ |
| j4 | $NO + h\nu \rightarrow N + O$ |
| j5 | $NO_2 + h\nu \rightarrow NO + O$ |
| j6 | $NO_3 + h\nu \rightarrow NO + O_2$ |
| j7 | $NO_3 + h\nu \rightarrow NO_2 + O$ |
| j8 | $N_2O_5 + h\nu \rightarrow NO_2 + NO_3$ |
| j9 | $HNO_3 + h\nu \rightarrow NO_2 + OH$ |
| j10 | $HNO_4 + h\nu \rightarrow NO_2 + HO_2$ |
| j11 | $N_2O + h\nu \rightarrow O(^1D) + N_2$ |
| j12 | $CH_3OOH + h\nu \rightarrow CH_2O + H + OH$ |
| j13 | $CH_2O + h\nu \rightarrow CO + 2H$ |
| j14 | $CH_2O + h\nu \rightarrow CO + H_2$ |
| j15 | $H_2O_2 + h\nu \rightarrow 2\ OH$ |
| j16 | $H_2O + h\nu \rightarrow H + OH$ |
| j17 | CFC11 + $h\nu \rightarrow$ (products) |
| j18 | HCFC22 + $h\nu \rightarrow$ (products) |
| j19 | $CH_3CCl3 + h\nu \rightarrow$ (products) |

**Table 3.** Gas Phase Reactions Included in LMDz-INCA

| | Reaction |
|---|---|
| k1 | $O(^1D) + N_2 \rightarrow O + N_2$ |
| k2 | $O(^1D) + O_2 \rightarrow O + O_2$ |
| k3 | $O(^1D) + H_2O \rightarrow 2\ OH$ |
| k4 | $O + O + M \rightarrow O_2 + M$ |
| k5 | $O + O_2 + M \rightarrow O_3 + M$ |
| k6 | $O + O_3 \rightarrow 2\ O_2$ |
| k7 | $O(^1D) + O_3 \rightarrow 2\ O_2$ |
| k8 | $O + OH \rightarrow H + O_2$ |
| k9 | $O + HO_2 \rightarrow OH + O_2$ |
| k10 | $H + O_2 + M \rightarrow HO_2 + M$ |
| k11 | $H + O_3 + M \rightarrow OH + O_2$ |
| k12 | $H + NO_2 + M \rightarrow OH + NO$ |
| k13 | $H + HO_2 + M \rightarrow 2\ OH$ |
| k14 | $H + HO_2 + M \rightarrow H_2 + O_2$ |
| k15 | $H + HO_2 + M \rightarrow H_2O + O$ |
| k16 | $OH + O_3 \rightarrow HO_2 + O_2$ |
| k17 | $HO_2 + O_3 \rightarrow OH + 2\ O_2$ |
| k18 | $HO_2 + HO_2 \rightarrow H_2O_2$ |
| k19 | $H_2O_2 + OH \rightarrow H_2O + HO_2$ |
| k20 | $OH + HO_2 \rightarrow H_2O + O_2$ |
| k21 | $OH + OH \rightarrow H_2O + O$ |
| k22 | $H_2 + OH \rightarrow H_2O + H$ |
| k23 | $H_2 + O(^1D) \rightarrow H + OH$ |
| k24 | $N_2O + O(^1D) \rightarrow 2\ NO$ |
| k25 | $N_2O + O(^1D) \rightarrow N_2 + O_2$ |
| k26 | $N + O_2 \rightarrow NO + O$ |
| k27 | $N + NO \rightarrow N_2 + O$ |
| k28 | $N + NO_2 \rightarrow N_2O + O$ |
| k29 | $NO + HO_2 \rightarrow NO_2 + OH$ |
| k30 | $NO + O_3 \rightarrow NO_2 + O_2$ |
| k31 | $NO_2 + O \rightarrow NO + O_2$ |
| k32 | $NO_2 + O_3 \rightarrow NO_3 + O_2$ |
| k33 | $NO_3 + HO_2 \rightarrow 0.4\ HNO_3 + 0.6\ OH + 0.6\ NO_2$ |
| k34 | $NO_2 + NO_3 + M \rightarrow N_2O_5 + M$ |
| k35 | $N_2O_5 + M \rightarrow NO_2 + NO_3 + M$ |
| k36 | $NO_2 + OH + M \rightarrow HNO_3 + M$ |
| k37 | $HNO_3 + OH \rightarrow NO_3 + H_2O$ |
| k38 | $NO_3 + NO \rightarrow 2\ NO_2$ |
| k39 | $NO_2 + HO_2 + M \rightarrow HNO_4 + M$ |
| k40 | $HNO_4 + M \rightarrow HO_2 + NO_2 + M$ |
| k41 | $HNO_4 + OH \rightarrow H_2O + NO_2 + O_2$ |
| k42 | $CH_4 + OH \rightarrow CH_3O_2 + H_2O$ |
| k43 | $CH_4 + O(^1D) \rightarrow CH_3O_2 + OH$ |
| k44 | $CH_4 + O(^1D) \rightarrow H_2 + CH_2O$ |
| k45 | $CH_3O + O_2 \rightarrow CH_2O + HO_2$ |
| k46 | $CH_3OH + OH \rightarrow CH_2O + HO_2 + H_2O$ |
| k47 | $CH_3O_2 + NO \rightarrow CH_3O + NO_2$ |
| k48 | $CH_3O_2 + NO_3 \rightarrow CH_3O + NO_2 + O_2$ |
| k49 | $CH_3O_2 + CH_3O_2 \rightarrow CH_3OH + CH_2O + O_2$ |
| k50 | $CH_3O_2 + HO_2 \rightarrow CH_3OOH + O_2$ |
| k51 | $CH_3O_2 + CH_3O_2 \rightarrow 2\ CH_3O + O_2$ |
| k52 | $CH_3OOH + OH \rightarrow CH_2O + OH + H_2O$ |
| k53 | $CH_3OOH + OH \rightarrow CH_3O_2 + H_2O$ |
| k54 | $CH_2O + OH \rightarrow CO + H_2O + HO_2$ |
| k55 | $CH_2O + O \rightarrow CO + OH + HO_2$ |
| k56 | $CH_2O + NO_3 \rightarrow CO + HO_2 + HNO_3$ |
| k57 | $CO + OH \rightarrow CO_2 + H$ |
| k58 | $SF_6 + O(^1D) \rightarrow$ (products) |
| k59 | $CH_3CCl_3 + OH \rightarrow$ (products) |
| k60 | $CFC11 + O(^1D) \rightarrow$ (products) |
| k61 | $HCFC22 + O(^1D) \rightarrow$ (products) |
| k62 | $HCFC22 + OH \rightarrow$ (products) |

*Liu* [1994]. The annual cycle of the *Hao and Liu* [1994] emissions has been moved forward by one month as suggested by *Lawrence et al.* [1999], providing peak emissions in March and September associated with the Northern and Southern Hemisphere burning seasons, respectively. In the extratropics, the biofuel and agricultural waste burning emissions are taken from the EDGAR database. The boreal forest fire emissions are based on *Müller* [1992]. As was done in the case of fossil fuel emissions, secondary CO from biomass burning NMHCs are introduced on the basis of the magnitude suggested by *Prather et al.* [2001].

[27] Soil emissions of NO are based on *Yienger and Levy* [1995]. Secondary CO from biogenic Volatile Organic Compounds (VOCs) oxidation (isoprene, monoterpenes, and other reactive compounds) is distributed according to *Guenther et al.* [1995] on the basis of the global estimates of *Prather et al.* [2001]. The spatial and temporal distribution of CO oceanic emissions is taken from *Erickson and Taylor* [1992] and scaled to a global mean of 50 Tg/yr [*Prather et al.*, 2001]. Emissions of $CH_4$ from rice paddies, wetlands, termites, wild animals and ruminants, and ocean are taken from *Fung et al.* [1991]. $N_2O$ emissions are based on *Bouwman and Taylor* [1996] and *Kroeze et al.* [1999] for continental emissions and on *Nevison and Weiss* [1995] for oceanic emissions. As in the study by *Hauglustaine and Ehhalt* [2002], $H_2$ emissions are spatially and temporally distributed on the basis of CO emissions with global magnitude taken from this earlier study.

[28] As described by *Jourdain and Hauglustaine* [2001], lightning NO emissions are calculated interactively in LMDz-INCA on the basis of the occurrence of convection and cloud top heights diagnosed at each time step by the GCM. The lightning flash rate is determined according to the *Price and Rind* [1992] parameterization. Figure 8 compares the flash rate predicted by the model for the December–February and June–August periods to the composite measurements collected by the Optical Transient Detector (OTD) and the Lightning Intensity Sensor (LIS) spaceborne instruments over the period 1996–2001 (version 0.1) and described by *Christian et al.* [2003]. The model reproduces the main features of the observed seasonal cycle and the general location of convective regions. Several disagreements clearly appear. During the northern winter, the model significantly underestimates the lightning activity in central Africa. On the other hand, the flash rate is overestimated over northern Australia and South America. During the northern summer, the model strongly overestimates the lightning flashes during the Indian monsoon. The lightning activity is reasonably well simulated over North America and to a lesser extent during the West African monsoon. These features are directly linked to the simulated convection location and magnitude (cloud top) in the GCM and should be improved in future versions of LMDz. On the basis of the partitioning between intracloud (IC) and cloud-to-ground (CG) flashes proposed by *Price and Rind* [1992], and adopting a production of $6.7 \times 10^{25}$ and $6.7 \times 10^{26}$ NO molecules per IC and CG flash, respectively

**Table 4.** Heterogeneous Reactions Included in LMDz-INCA

| | Reaction | Reaction Probability |
|---|---|---|
| h1 | $N_2O_5 \rightarrow 2\ HNO_3$ | $\gamma_{200K} = 0.185$, $\gamma_{300K} = 0.03$ |
| h2 | $NO_3 \rightarrow HNO_3$ | $\gamma = 0.1$ |
| h3 | $NO_2 \rightarrow 0.5\ HNO_3 + 0.5\ HNO_2$ | $\gamma = 0.1$ |
| h4 | $HO_2 \rightarrow 0.5\ H_2O_2 + 0.5\ O_2$ | $\gamma = 1 \times 10^{-3}$ |

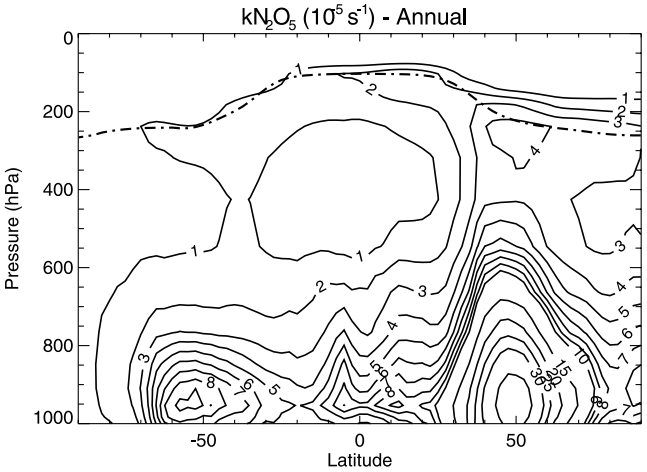


**Figure 7.** Zonal and annual mean distribution of calculated heterogeneous reaction rate of $N_2O_5$ on sulfate aerosols ($10^{-5}$ $s^{-1}$). The dash-dotted line represents the model tropopause.

[*Price et al.*, 1997], we derive a global annual NO production of only 1.07 TgN/yr [*Jourdain and Hauglustaine*, 2001]. This value is lower than the range of 2–20 TgN provided by previous estimates [*Lee et al.*, 1997; *Price et al.*, 1997; *Allen and Pickering*, 2002]. The reasons for this disagreement have been mainly attributed to an underestimate of cloud top height in the GCM, and it was decided to rescale the global production to an annual value of 5 TgN for this work [*Lee et al.*, 1997; *Prather et al.*, 2001]. The NO production is vertically distributed in the convective column on the basis of the empirical profiles derived by *Pickering et al.* [1998].

### 2.2.3. Dry Deposition

[29] Dry deposition velocities ($v_d$) are calculated interactively at each time step following the resistance-in-series approach [*Wesely*, 1989]:

$$v_d = \frac{1}{R_a + R_b + R_c}, \tag{4}$$

where $R_a$, $R_b$ and $R_c$ (s/m) are the aerodynamical, quasi-laminar, and surface resistances, respectively. $R_a$ and $R_b$ are calculated on the basis of *Walcek et al.* [1986]. The surface resistances are determined for all species included in LMDz-INCA according to their Henry law equilibrium constant and reactivity factor for oxidation of biological substances. The surface resistances are calculated using the vegetation map classification from *De Fries and Townshend* [1994] interpolated to the model grid and redistributed into the classification proposed by *Wesely* [1989]. The lower and upper canopy resistances (including stomata, mesophyll, and cuticle resistances) as well as ground resistances are all parameterized according to *Wesely* [1989]. Meteorological variables needed to calculate $R_a$, $R_b$ and $R_c$ (including temperature, specific humidity, wind speed, precipitation, snow cover, and solar radiation at the surface) are provided by the GCM at each time step.

[30] Figure 9 shows the resulting 24-hour averaged dry deposition velocity of $O_3$ and $HNO_3$ calculated for July conditions. Low deposition velocities are calculated for ozone over the ocean (0.05–0.1 cm/s). Over the continents the deposition velocities reach 0.4–0.5 cm/s. $HNO_3$ has a much larger deposition velocity largely controlled by the atmospheric stability because of its high solubility. Maximum values of 2–3 cm/s are predicted over land. Comparison with previous global model results [*Müller*, 1992; *Wang et al.*, 1998; *Ganzeveld and Lelieveld*, 1995; *Brasseur et al.*, 1998a] suggests that deposition velocities are underestimated by 20–30% over forested regions (Amazon forest, northeastern United States) in LMDz-INCA.

[31] The soil uptake of $H_2$ and CO is parameterized as a dry deposition process. As in the study by *Hauglustaine and Ehhalt* [2002], the seasonal and geographical distributions of deposition velocities for these two species is prescribed according to the Net Primary Productivity (NPP) calculated over land by the ORCHIDEE vegetation model (G. Krinner et al., A dynamical global vegetation model for studies of the coupled atmosphere-biosphere system, submitted to *Global Change Biology*, 2003). The calculated $H_2$ deposition velocity (Figure 10) shows a strong seasonal cycle with maximum values reaching 0.1–0.12 cm/s over temperate and boreal forests in summer. In winter, low values (<0.02 cm/s) are calculated over land in the Northern Hemisphere. These values appear somewhat lower than those obtained by *Hauglustaine and Ehhalt* [2002]. High values are calculated in the tropics during all seasons.

### 2.2.4. Wet Removal

[32] The LMDz general circulation model distinguishes between stratiform and convective precipitation. The wet scavenging of soluble species is calculated in INCA for both types of precipitation separately and parameterized as a first-order loss process [*Giorgi and Chameides*, 1985]:

$$\frac{d}{dt}C_g = -\beta C_g, \tag{5}$$

where $C_g$ is the gas phase concentration of the considered species and $\beta$ the scavenging coefficient (1/s). The scavenging associated with large-scale stratiform precipitation is calculated adopting the falling raindrop approach and calculating the amount of gas removed by the drop falling through each model layer located below the cloud level [*Seinfeld and Pandis*, 1998]. The increase of the aqueous phase concentration $C_{aq}^m$ of an irreversibly scavenged gas in a droplet originating from level $m$ and falling through a model layer $i$ (such as layer $i$ < layer $m$) can be estimated by a mass balance between the rate of increase of the mass of species in the droplet and the rate of transfer of species to the drop so that [*Seinfeld and Pandis*, 1998]

$$\left[\frac{d}{dt}C_{aq}^m\right]_i = \frac{6K_c}{D_p}C_g^i, \tag{6}$$

where $C_g^i$ is the gas phase concentration in layer $i$ encountered by the drop originating from level $m$, $D_p$ is the rain droplet diameter fixed to a constant value of $3 \times 10^{-3}$ m in this version of INCA, and $K_c$ the mass transfer coefficient (m/s). The mass transfer is calculated until equilibrium of the dissolved gas is eventually reached in the falling drop. $K_c$ is calculated with the empirical relation of *Bird et al.* [1960] as given by *Brasseur et al.* [1998a]. In this relation, we assume a constant value for the drop terminal

**Table 5.** Global Surface Emissions of Trace Gases in LMDz-INCA

| | Emission |
|---|---|
| *$NO_x$, TgN/yr* | |
| Fossil fuel + industry + biofuel | 24.66 |
| Biomass burning | 8.07 |
| Soils | 5.48 |
| Ships | 3.08 |
| Total | 41.29 |
| *$N_2O$, TgN/yr* | |
| Fossil fuel + industry + biofuel | 0.78 |
| Biomass burning | 1.14 |
| Soils | 7.20 |
| Excecra | 1.02 |
| Ocean | 3.50 |
| Total | 13.64 |
| *$CH_4$, Tg/yr* | |
| Fossil fuel + industry + biofuel | 98.71 |
| Biomass burning | 25.36 |
| Landfills | 56.34 |
| Rice paddies | 79.55 |
| Wetlands | 240.24 |
| Animals | 88.85 |
| Termites | 20.00 |
| Ocean | 15.00 |
| Total | 624.05 |
| *CO, Tg/yr* | |
| Fossil fuel + industry + biofuel | 650.00 |
| Biomass burning | 514.00 |
| Biogenic | 150.00 |
| Ocean | 50.00 |
| Total | 1364.00 |
| *Secondary CO, Tg/yr* | |
| VOC Fossil fuel + industry + biofuel | 110.00 |
| VOC Biomass burning | 30.00 |
| VOC Biogenic | 290.00 |
| Total | 430.00 |
| *$H_2$, Tg/yr* | |
| Fossil fuel + industry + biofuel | 17.00 |
| Biomass burning | 15.00 |
| Soils | 6.00 |
| Ocean | 6.00 |
| Total | 44.00 |
| *$CH_2O$, Tg/yr* | |
| Fossil fuel + industry + biofuel | 0.31 |
| Biomass burning | 2.33 |
| Total | 2.64 |

velocity of 8 m/s. From equation (5) we derive, for the scavenging coefficient associated with large-scale precipitation in layer $i$,

$$\beta_i^{ls} = -\frac{1}{C_g^i}\sum_{m>i}\left[\frac{d}{dt}C_g^i\right]_m = \frac{1}{C_g^i}\sum_{m>i}L^m\left[\frac{d}{dt}C_{aq}^m\right]_i, \qquad (7)$$

where $L^m$ is the dimensionless liquid rain water content of layer $m$. It should be noted that the above formalism neglects a possible re-evaporation of the drop with transfer of the dissolved gas back to the gas phase [*Roelofs and Lelieveld*, 1995; *Liu et al.*, 2001]. The rain liquid water content ($L$) is derived from the total (solid + liquid) water flux calculated by the GCM. However, as in the studies by *Koch et al.* [1996], *Liu et al.* [2001], and *Hess et al.* [2000], we assume that rainout is suppressed at temperatures below 258 K.

[33] The scavenging by convective precipitation is calculated as part of the upward convective mass flux on the basis of a modified version of the scheme proposed by *Balkanski et al.* [1993]. On the basis of this formulation and on the basis of equation (5), we derive, for the scavenging coefficient associated with convective precipitation,

$$\beta^{cv} = -f\mathcal{F}_u\frac{g}{p}, \qquad (8)$$

where $f$ is the fraction of soluble gas removed from the gas phase, $\mathcal{F}_u$ the upward convective mass flux diagnosed by the GCM (kg/m$^2$/s), $p$ the pressure and $g$ the gravity constant.

[34] As in the study by *Liu et al.* [2001], we assume that in the convective column,

$$f = 1 - e^{-\alpha\Delta z}, \qquad (9)$$

where $\Delta z$ (m) is the height in the convective tower calculated from the cloud base. The scavenging efficiency $\alpha$ (m$^{-1}$) is calculated as the ratio of the rate constant for conversion of cloud water to precipitation ($C_{pr}$) and the updraft velocity $w$. On the basis of *Mari et al.* [2000] and *Liu et al.* [2001], we adopt $C_{pr} = 5 \times 10^{-3}$ s$^{-1}$, $w = 10$ m/s leading $\alpha = 5 \times 10^{-4}$ m$^{-1}$.

[35] Nitric acid is used as a reference and the scavenging rate for any other species $x$ (in this version of INCA, $x$ stands for $H_2O_2$, $CH_3OOH$, $CH_2O$, and $HNO_4$) is scaled to the scavenging rate of $HNO_3$ according to its effective Henry law equilibrium constant $\mathcal{H}_x$ on the basis of *Seinfeld and Pandis* [1998].

[36] Figure 11 shows the resulting nitric acid lifetime associated with wet scavenging calculated by the model. The removal is efficient at midlatitudes in the lower troposphere with an associated lifetime of only 1–2 days below 2 km. At these latitudes, the scavenging rapidly decreases with altitude with corresponding lifetimes longer than 10 days above about 5 km. A very efficient removal associated mainly with convective precipitation is also predicted in the Intertropical Convergence Zone (ITCZ) with characteristic lifetimes of 2–4 days up to about 8 km. The calculated removal lifetime is in general agreement with the results presented by *Brasseur et al.* [1998a]. However, with LMDz-INCA we predict a more efficient removal in the lower troposphere. This feature is associated in the tropics with the adopted vertical profile for wet scavenging by convective precipitation and to the stratiform precipitation simulated by the GCM at midlatitudes. Another difference with this previous work arises from the temperature threshold imposed on the washout rate in our scheme imposing a more rapid decrease with altitude and at high latitudes. The role of convective precipitation is illustrated by comparing these results with the washout removal time obtained for a sensitivity experiment performed with convective washout turned off. In this case, the removal time in the tropics increases to 25–75 days, in sharp contrast with the reference simulation. Stratiform precipitation is generally confined in the lower troposphere and no significant washout is predicted above 5 km in the

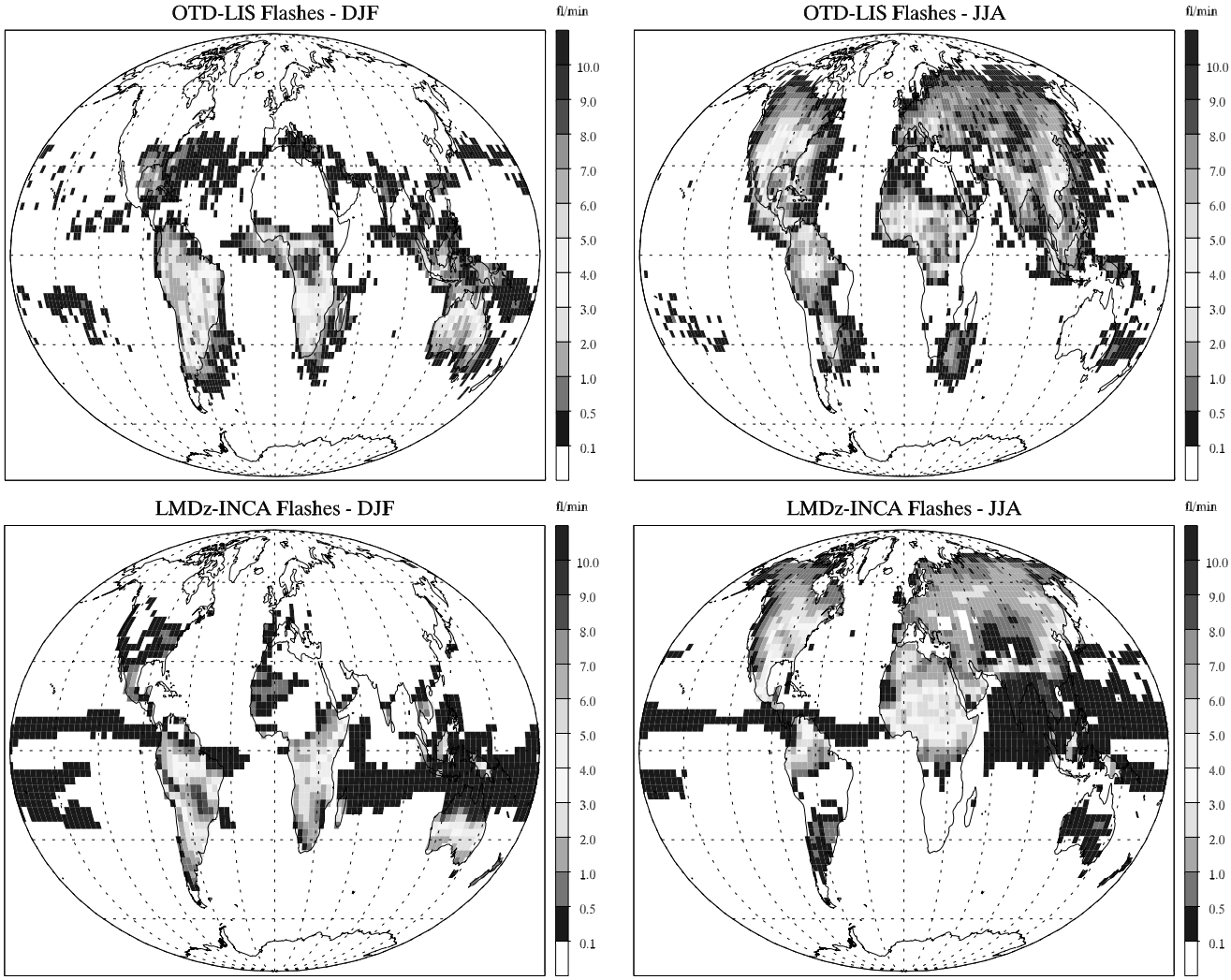


**Figure 8.** Gridded composite of lightning flashes (flashes/min) detected by the LIS (December 1997 to November 2000) and OTD (April 1995 to March 2000) instruments (version 0.1 prepared by *Christian et al.* [2003]) for DJF and JJA conditions (upper panels) and lightning flashes calculated by LMDz-INCA (lower panels). See color version of this figure at back of this issue.

tropics for this sensitivity simulation. At midlatitudes, the removal time is also significantly affected by convection and is generally larger than 5 days above 1–2 km when only stratiform precipitation is considered.

[37] In Figure 12, we evaluate the model performance in terms of wet scavenging simulation by comparing $^{210}$Pb calculated surface concentration with measurements. $^{210}$Pb is calculated on the basis of the radioactive disintegration of $^{222}$Rn with a rate constant of $2.1 \times 10^{-6}$ s$^{-1}$, an imposed dry deposition of 0.2 cm/s over land and of 0.05 cm/s over the ocean and frozen surfaces (latitudes higher than 70). We assume that the wet removal for aerosols (and hence $^{210}$Pb which aggregates on aerosols) is identical to that of nitric acid [*Balkanski et al.*, 1993; *Lee and Feichter*, 1995; *Rehfeld and Heimann*, 1995; *Brasseur et al.*, 1998a]. The background $^{210}$Pb concentration is reasonably well simulated by the model at marine and remote stations (Kerguelen, Dumont d'Urville). As was already pointed out for $^{222}$Rn, the concentrations are underestimated during summer at Dumont d'Urville. The model also captures fairly well the seasonal cycles observed at most marine and continental midlatitude and high-latitude stations. In the tropics and extratropics, the model reproduces very well the observed concentrations at Mauna Loa and Lamto and to a lesser extent at La Réunion island. The concentrations are also well simulated over the Pacific at Norfolk and Midway islands (not shown). The model tends, however, to underestimate the concentration at the Bermuda station (and Barbados, not shown) during summer, pointing to a too efficient scavenging in the western Atlantic region. We obtain, however, a good agreement with observations at Izana (not shown) in the eastern Atlantic. A significant underestimate of $^{210}$Pb is also obtained at Calcutta. This underestimate appears all the year and not only during the monsoon season. Figure 12 shows the major impact of convective precipitation on the distribution of $^{210}$Pb. Without convective washout a general overestimate arises in the model results. This disagreement appears not only in the tropics (Mauna Loa, Lamto) or during the monsoon season (Calcutta) but also at northern midlatitudes during summer (Chester, Bermuda).

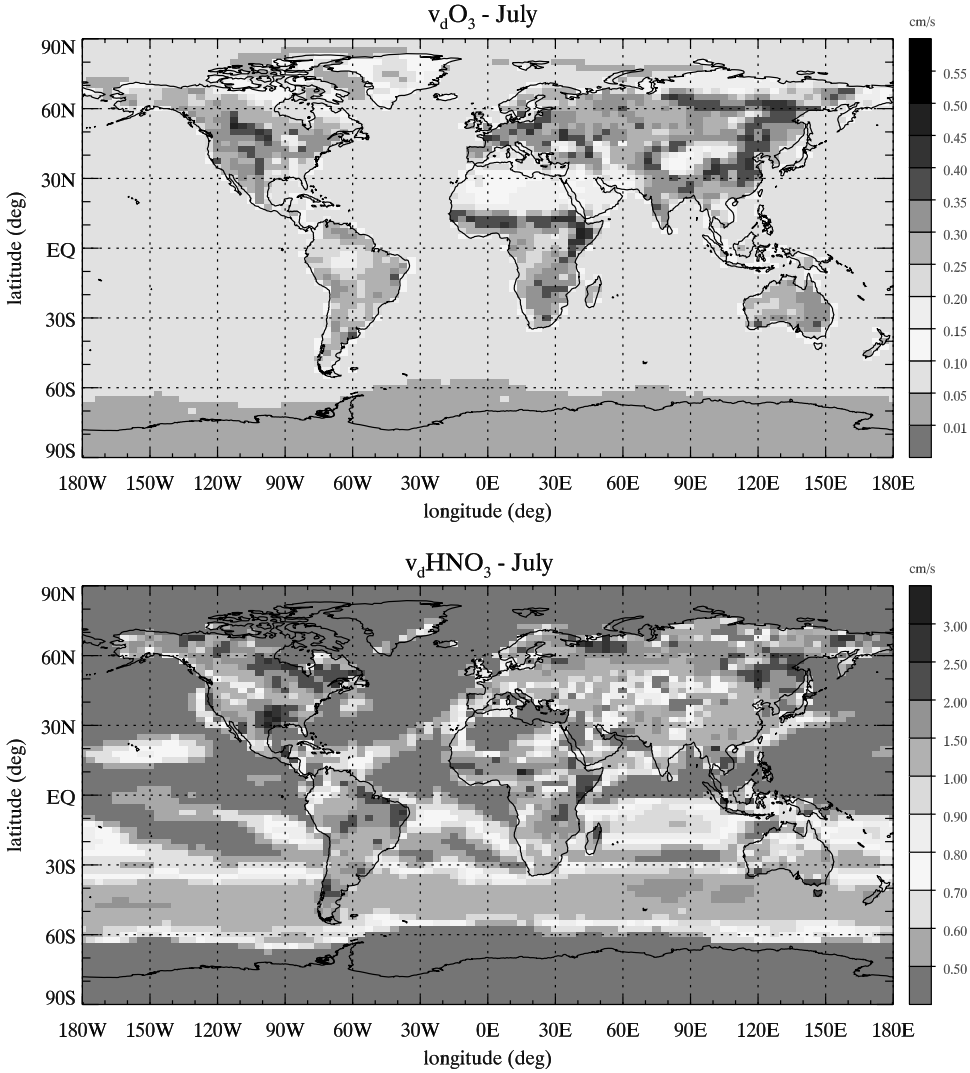


**Figure 9.** Monthly mean $O_3$ and $HNO_3$ surface dry deposition velocity (cm/s) calculated in LMDz-INCA for July conditions. See color version of this figure at back of this issue.

[38] Figure 13 shows the calculated concentrations and comparisons with selected vertical profiles measured over the central United States and Alaska [*Moore et al.*, 1973] and over the northwestern Pacific during the PEM-West A (fall 1991) and PEM-West B (spring 1994) campaigns by *Dibb et al.* [1996, 1997]. Above 12 km the calculated concentrations are generally in line with the measurements. In the middle troposphere, the model significantly overestimates the observations during winter over the central United States. The measurements collected during the PEM-West campaigns show a high variability. The model results generally fall within the observed values in the middle and upper troposphere. In the lower troposphere, the calculated values underestimate the observations during PEM-West A and over Japan during PEM-West B. The measured vertical gradients are generally captured by the model during these campaigns. *Guelle et al.* [1998b] suggested that the underprediction would be associated with excessive removal by convective precipitation during PEM-West A and by stratiform precipitation during PEM-West B. Comparison with the model results obtained for stratiform precipitation only suggest that convective washout plays a dominant role during all seasons. In this sensitivity experiment, $^{210}Pb$ is significantly overestimated over the whole model domain. Note that this comparison is only intended to provide a general evaluation of the calculated profiles since this version of the model is run in a climate mode and not with the meteorological conditions prevailing during the campaigns.

[39] Figure 14 illustrates the total (wet + dry) annual nitrogen deposition at the surface calculated with LMDz-INCA. The maximum deposition reaches 10–12 kgN/ha/yr and is predicted close to source regions in Northern America, Western Europe, and Southeast Asia. A regional budget analysis provides integrated depositions of 5.8 TgN/yr (12% of global deposition), 4.5 TgN/yr (9%), and 7.6 TgN/yr (15%) over these 3 regions respectively. A significant amount (19.7 TgN/yr, 40% of global deposition) of the nitrogen is deposited over the ocean. Secondary deposition maxima of 3–5 kgN/ha/yr are calculated over biomass burning regions in Africa and South America.

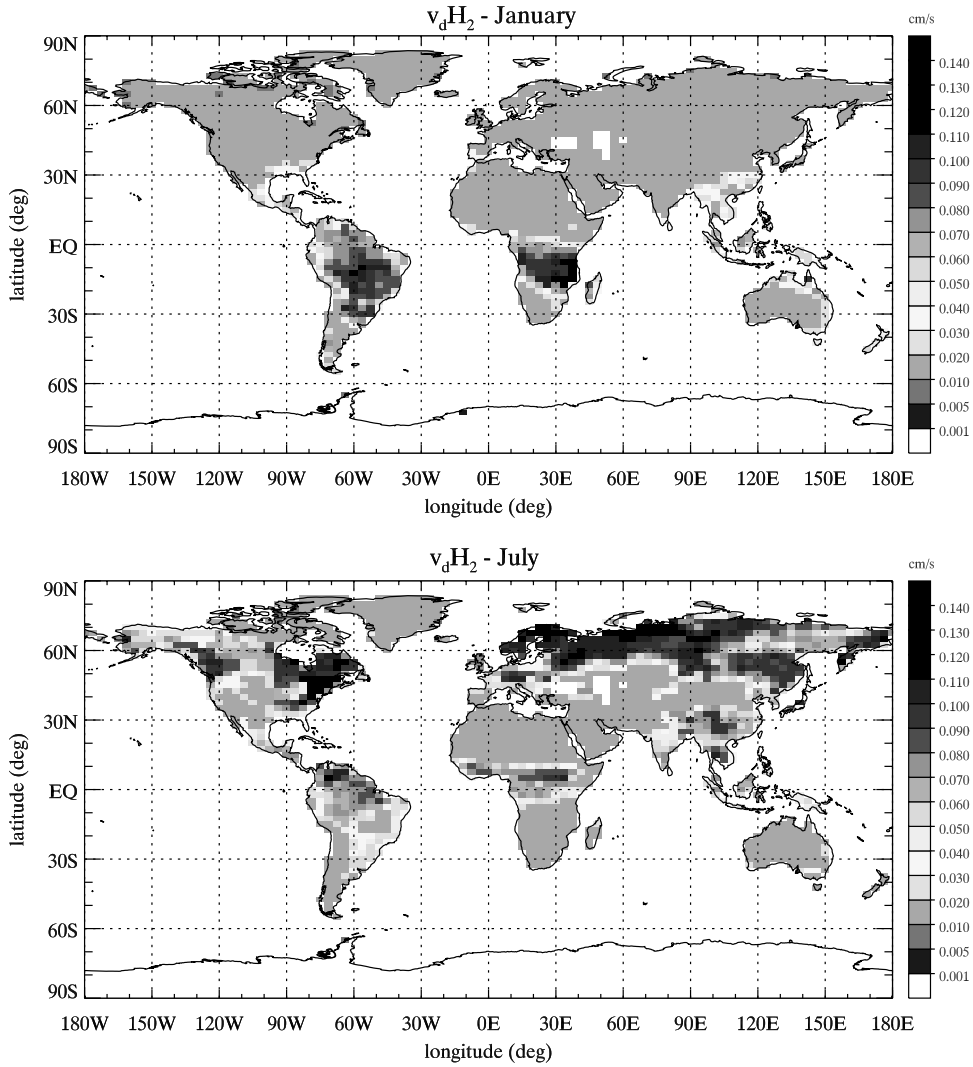


**Figure 10.** Monthly mean $H_2$ surface dry deposition velocity (cm/s) calculated in LMDz-INCA for January and July conditions. See color version of this figure at back of this issue.

The calculated nitrogen deposition is almost equally distributed between wet and dry deposition. This spatial distribution is in general agreement with previous model estimates [*Penner et al.*, 1991; *Kraus et al.*, 1996; *Galloway et al.*, 1994; *Holland et al.*, 1997, 1999; *Rodhe et al.*, 2002]. The comparison with maps of N deposition fluxes from site-network observations produced for the United States and Western Europe by E. A. Holland et al. (Nitrogen deposition onto the United States and western Europe: A synthesis of observations and models, submitted to *Ecological Applications*, 2003) (hereinafter referred to as Holland et al., submitted manuscript, 2003) also shows a fairly good agreement over the northeastern United States. In Europe, the calculated maximum is somewhat shifted north in comparison to the observations. Figure 15 provides a more quantitative comparison nitrogen deposition measurements. Wet deposition measurements of $NO_3^-$ for the United States and western Europe were compiled for the 1978–2002 time period to calculate monthly average deposition of nitrate. In the United states, wet deposition data were provided by the National Atmospheric Deposition Program [*Lamb and Van Bowersox*, 2000]. In Europe, measurements of wet deposition fluxes of $NO_3^-$ were provided by the European Monitoring and Evaluation Programme (EMEP). In Europe the method of sampling varied from location to location, country to country, and, in general, differed from the method used in the United States. The samples of precipitation were collected daily using either the precipitation-only samplers (described above) or bulk sampling devices which are continually open to the atmosphere, and are thus more subject to contamination [*Erisman et al.*, 1994; *van Leeuwen et al.*, 1996]. For this comparison, the calculated nitrogen wet deposition was interpolated on each collecting site for each month. Both comparisons show a high variability in the data as well as in the modeled depositions. Over the United States at the NADP monitoring sites, the model generally reproduces the general behavior of the measurements with a correlation coefficient $r^2$ of 0.47. The figure indicates that the deposition is overesti-

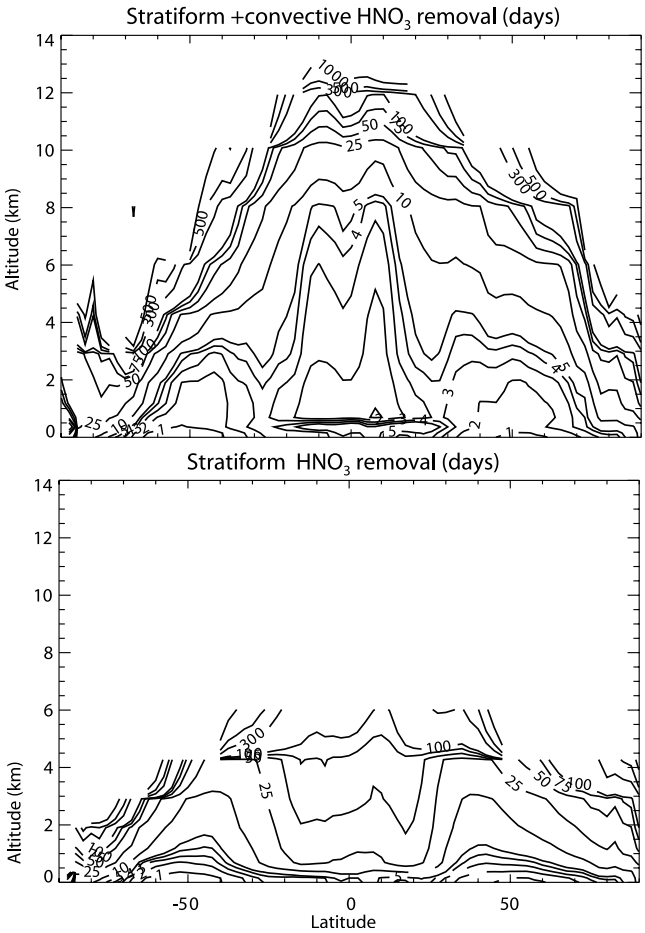


**Figure 11.** Zonal and annual mean $HNO_3$ lifetime (days) associated with wet removal processes calculated in LMDz-INCA for the reference case (upper panel) and for a sensitivity experiment including only removal by stratiform precipitation (lower panel).

mated by up to a factor of two during summer (JJA). This feature is mainly associated with an overestimate of precipitation over the continents during summer as was also pointed out by *Boucher et al.* [2002]. Over Europe at the EMEP monitoring stations, the variability is large and a low correlation between the model and the measurements is obtained. Several data points characterized by $NO_3^-$ deposition higher than about 0.5 kgN/ha are not reproduced by the model. On the other hand, as was the case for NADP data, an overestimate of the measurements by the model is obtained during summer. As illustrated by *Bauer et al.* [2004], it should be noted that the formation of PAN, which is not considered in our model, reduces surface $HNO_3$ by 10–25% in source region. The resulting decreased nitrogen deposition in these regions would, however, not fully reconcile the model and the measurements. This comparison indicates that, even if the general patterns of the nitrogen deposition are correctly reproduced by the model, scavenging and transport of nitrogen species could be improved in the model. This conclusion was also reached by previous model evaluations against measured nitrogen deposition [*Roelofs and Lelieveld*, 1995; *Holland et al.*, 1997; *Horowitz et al.*, 2003].

### 2.2.5. Boundary Conditions in the Stratosphere

[40] Transport of species and chemistry are calculated interactively up to the model upper level. However, since no chlorine or bromine chemistry nor heterogeneous reactions on polar stratospheric clouds are considered in this version of LMDz-INCA, ozone concentrations are relaxed toward observations at the uppermost model levels at each time step. This relaxation is performed above a potential temperature $\theta$ = 380K. As in the study by *Horowitz et al.* [2003], we adopt a relaxation time constant of 10 days. The ozone observations are taken from the monthly mean 3D climatologies of *Li and Shine* [1995] that are based on ozone soundings and different satellite data. Because of the coarse vertical resolution of the model at the tropopause, this approach overestimates the cross-tropopause ozone influx into the troposphere. To overcome this difficulty, we adopt an adjustment inspired from *McLinden et al.* [2000] and *Bey et al.* [2001]. According to this method, ozone is reduced by 25% above $\theta$ = 380K before the advection calculation and reset to its initial value after the large-scale transport. This method results in a satisfactory simulation of the ozone influx, as illustrated below. In the case of nitrogen species, $N_2O$ is treated explicitly in the model and the stratospheric source of $NO_y$ is directly calculated from reaction $k_24$ (Table 3). In order to investigate the contribution of the stratospheric influx to the calculated ozone levels in the troposphere, a stratospheric ozone-like tracer is included in LMDz-INCA. As described by *Roelofs and Lelieveld* [1997] and *Hauglustaine and Brasseur* [2001], this tracer is imposed to be identical to the modeled real ozone above the model tropopause. Below the tropopause, the photochemical production is set equal to zero while a photochemical loss is attributed to ozone photolysis followed by the reaction of $O(^1D)$ with water vapor, and to the reaction of ozone with OH and $HO_2$. Dry deposition is also considered for this "stratospheric ozone" tracer.

[41] The simulation of ozone in the upper troposphere is very sensitive to the tropopause height simulated by the GCM. Figure 16 illustrates the tropopause calculated in LMDz-INCA for January and July conditions. The thermal tropopause is calculated according to the *World Meteorological Organization* (WMO) [1992] criterion and corrected at latitudes higher than 60 degrees in the winter hemisphere as in the study by *Steil et al.* [1998]. The model results are in general agreement with the NCEP [*Randel et al.*, 2000] and ECMWF [*Hoinka*, 1998] derived tropopause. Two belts with strong meridional gradients can be seen between 30° and 60°. In the tropics, the tropopause reaches 110 hPa. A disagreement appears at midlatitudes in the Northern Hemisphere summer where the model underestimates the tropopause pressure compared to both NCEP and ECMWF by 30–40 hPa.

[42] As described by *Brasseur et al.* [1998a], the water vapor mixing ratio calculated by the GCM is corrected in the stratosphere in order to account for methane and molecular hydrogen oxidation:

$$\mu_{H_2O} = 6 \times 10^{-6} - 2\mu_{CH_4} - \mu_{H_2}, \qquad (10)$$

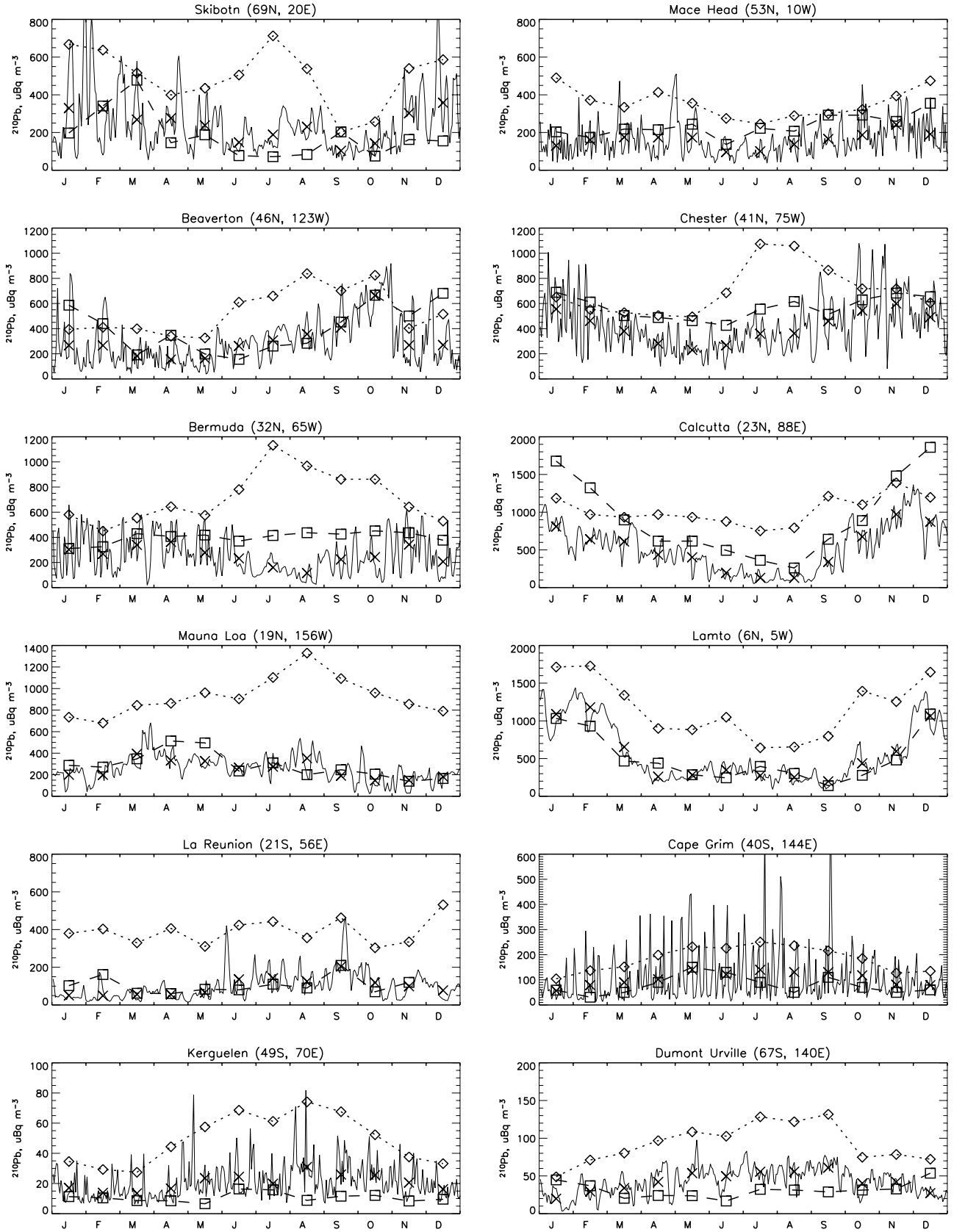


**Figure 12.** Observed (squares) and calculated (solid line is day-to-day variation, and crosses are monthly mean) $^{210}$Pb surface concentration ($\mu$Bq/m$^3$) at selected stations. Measurements as reported by *Guelle et al.* [1998a]. Monthly mean model results obtained when convective washout is suppressed are also shown for comparison (diamonds and dotted line).

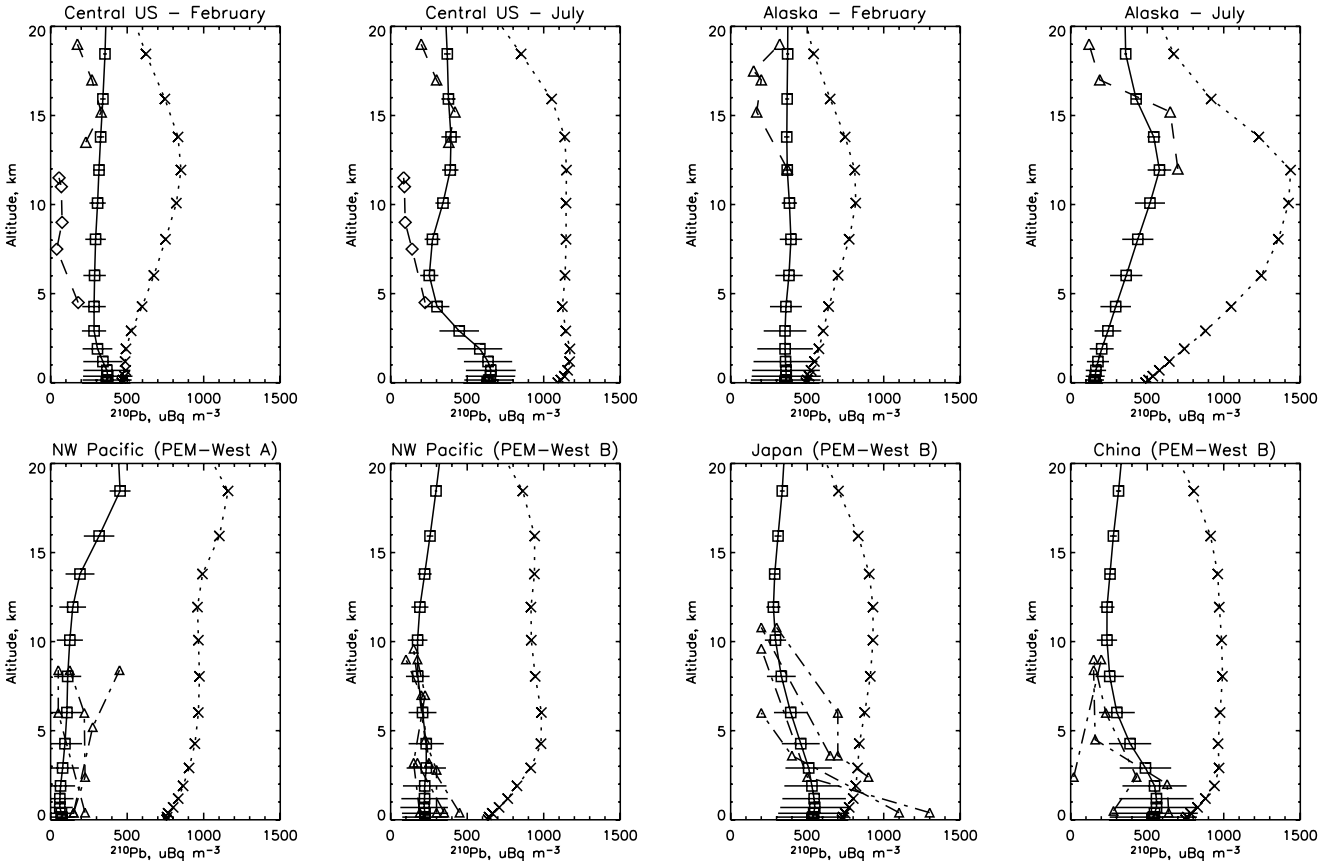


**Figure 13.** Observed (dashed lines with diamonds or triangles) and calculated (solid lines with squares) $^{210}$Pb profiles ($\mu$Bq/m$^3$) at selected locations. Measurements over the central United States and Alaska are from *Moore et al.* [1973], and those over the northwestern Pacific are from *Dibb et al.* [1996, 1997]. Model results obtained when convective precipitation is suppressed are also shown for comparison (crosses and dotted line).

where $\mu_{H_2O}$, $\mu_{CH_4}$, and $\mu_{H_2}$ denote water vapor, methane and molecular hydrogen volume mixing ratios, respectively.

## 3. Model Evaluation

[43] A total of 25 years has been simulated during the development phase of the model with initial conditions taken from the MOZART CTM [*Hauglustaine et al.*, 1998] and interpolated on the LMDz-INCA model grid. The results presented here are taken from the last year of the simulation unless otherwise stated.

### 3.1. Long-Lived Species

[44] In the following section we illustrate the distribution of long-lived species calculated on the basis of the a priori emission inventory. Since the interhemispheric exchange rate in the model has been studied in a previous section, we focus this evaluation on the simulated seasonal cycle for these species. As mentioned earlier, in the current version of the model the distribution of radiatively active species ($N_2O$, $CH_4$, (H)CFCs, and $O_3$) does not feedback on the GCM climate.

[45] $N_2O$ is calculated explicitly in the model considering the surface emissions (Table 5), transport and mixing, and photochemistry. Figure 17 illustrates the seasonal evolution of $N_2O$ at selected stations from the CMDL and ALE-GAGE network. In order to compare the measurements and the climatological state simulated by the model, the measurements are averaged over the whole recording period for each month. The comparison is then performed by subtracting the annual mean at each site for both data sets, focusing on the seasonal cycle. However, it should be noted that the absolute $N_2O$ mixing ratio simulated by the model shows a fairly small offset of about −3 ppbv (about 1%) compared to observations. The seasonal cycle of this long-lived greenhouse gas is extremely small (a few tenths of a percent) in both the model and the measurements and often does not even show a discernible seasonal pattern as in Samoa islands. The seasonal cycle of surface emissions is dominated by the oceanic and soil contributions and shows a maximum in local summer as discussed by *Bouwman and Taylor* [1996]. This signal is visible in the simulated mixing ratio at several stations, such as Niwot Ridge, which shows a peak in summer and a higher variability because of source influence during this season. However, at most stations a small seasonal cycle showing a slight summer minimum is measured and simulated (e.g., Mace Head, Barrow, Mauna Loa). This minimum is associated with increased convective activity during summer and mixing of upper tropospheric air somewhat depleted in $N_2O$ from downdrafts. This

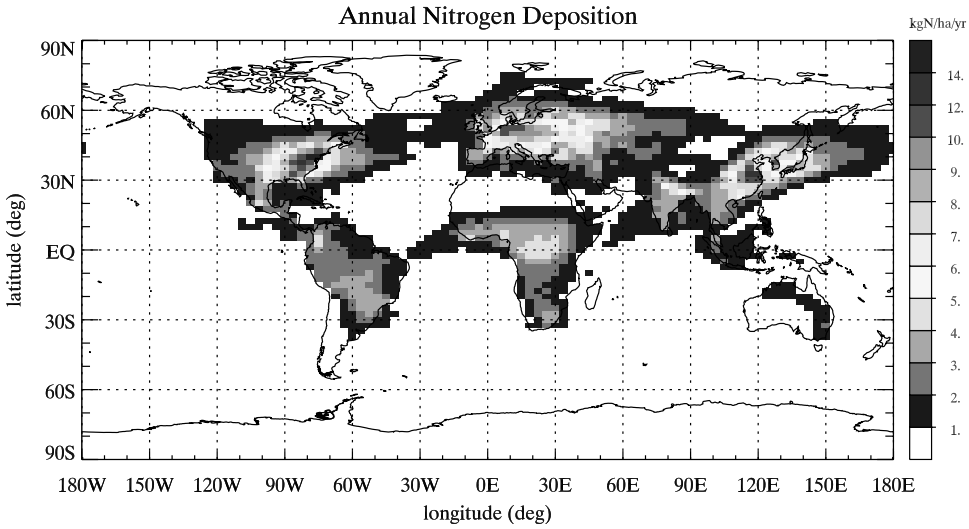


**Figure 14.** Annual and total (wet + dry) nitrogen deposition calculated with LMDz-INCA (kgN/ha/yr). See color version of this figure at back of this issue.

seasonal cycle is somewhat overestimated by the model at Alert and Trinidad Head. The local summer maximum observed at the South Pole is not reproduced by the model. A similar disagreement has also been obtained for the simulation of $^{222}$Rn and $^{210}$Pb at this station.

[46] Methane is also simulated explicitly in the model, considering the surface emissions (Table 5), transport and mixing, atmospheric oxidation, and soil uptake. The $CH_4$ seasonal cycle illustrated in Figure 18 shows a pronounced cycle in both the model and the CMDL measurements with a minimum during local summer when oxidation by OH is more active. The observed amplitude and phase of the seasonal variation is well reproduced by LMDz-INCA at most sites indicating a reasonable behavior of transport processes, oxidation by OH. A more systematic analysis of the simulated and observed $CH_4$ variability also indicates that the model reproduces fairly well the variability and its seasonal cycle at most sites affected by surface emissions. Work is also underway with LMDz-INCA to further improve the simulation of methane and refine the surface emissions and global OH on the basis of inverse modeling techniques as was done by *Hein et al.* [1997] and *Houweling et al.* [2000]. In the case of methane, it should be noted that an offset of about −150 ppbv (8–10%) is obtained for the absolute mixing ratio compared to the measurements (averaged over 10–15 years). Part of this offset is attributed to the atmospheric trend (reaching 10–15 ppbv/yr in the 1980s) and not accounted for in our study and emission inventory. The remaining of this offset is associated to too much oxidation by OH (see section 3.2).

[47] Figure 19 compares the observed and simulated molecular hydrogen mixing ratio at selected CMDL sta-

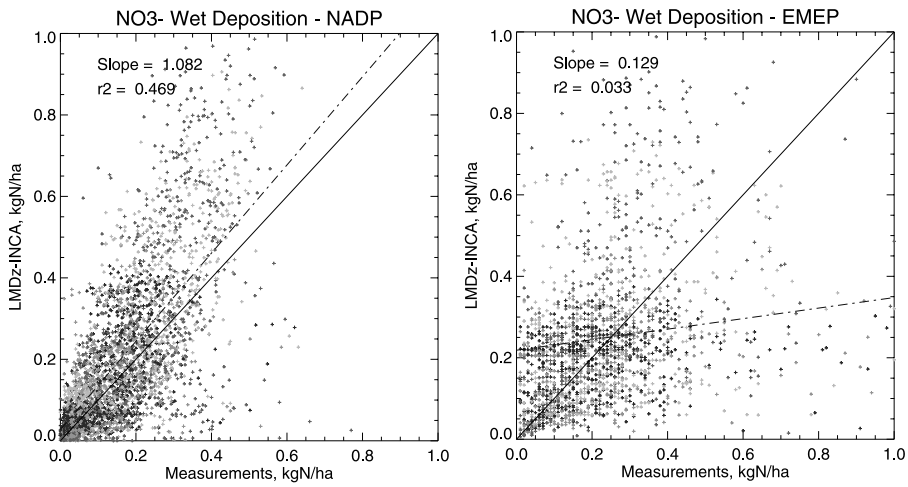


**Figure 15.** Correlation between $NO_3^-$ wet deposition (kgN/ha) calculated with LMDz-INCA and measured from surface networks (measurements reported by Holland et al. (submitted manuscript, 2003)). (left) Northern United States NADP network and (right) Europe EMEP network. The correlation coefficients ($r^2$) and slopes of the linear fit (dashed line) are provided for both regions. Solid line denotes the 1:1 line. Red crosses, summer (JJA) data; light blue, fall (SON); dark blue, winter (DJF); and green, spring (MAM). See color version of this figure at back of this issue.

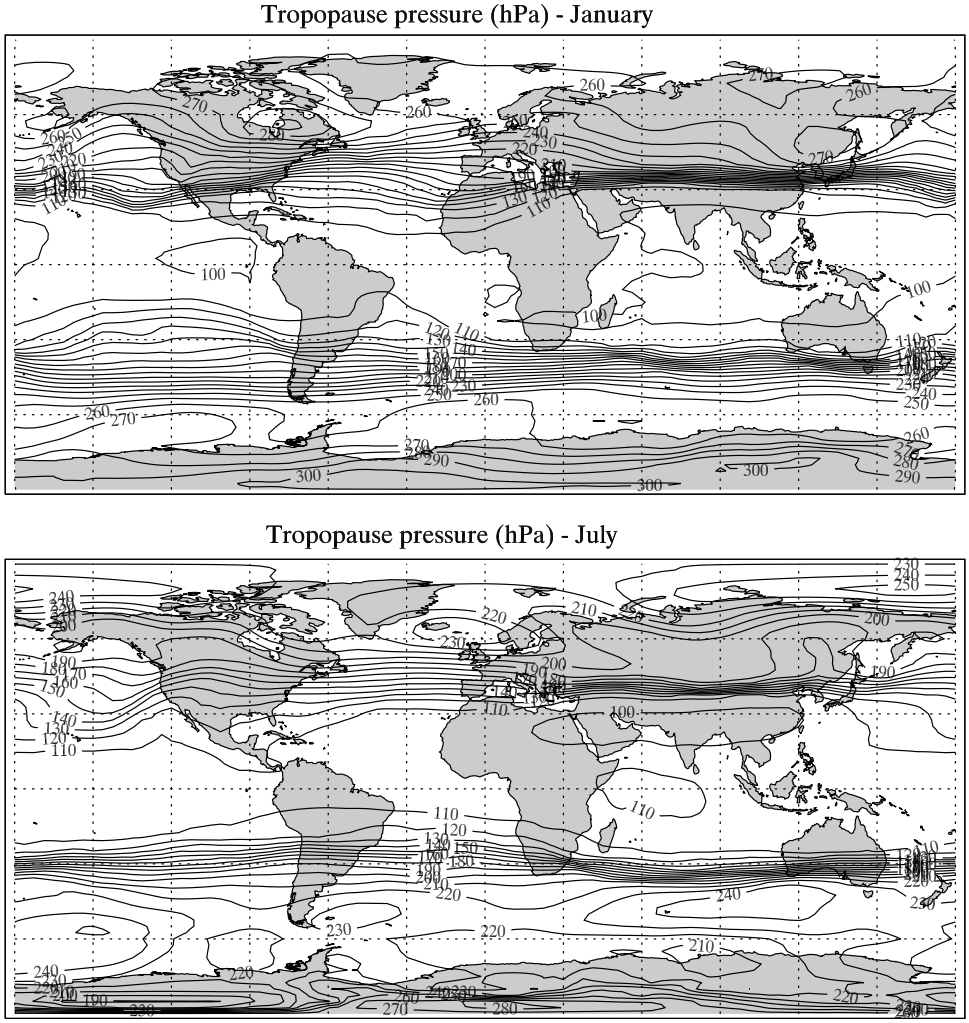


**Figure 16.** Pressure at the tropopause (hPa) calculated by LMDz-INCA for January and July conditions.

tions. As discussed by *Hauglustaine and Ehhalt* [2002], the major difficulty in the simulation of $H_2$ arises from the parameterization of soil uptake. This limitation is responsible for an overestimate of the measured mixing ratio by the model at continental sites (Utah) in the Northern Hemisphere during winter. The underestimate of $H_2$ by the model at tropical stations (Ascension, Samoa) also reflects the difficulty to represent the soil uptake in the model. As illustrated in Figure 10, the use of NPP as a proxy for soil microbial activity results in high deposition velocities over tropical forests (Africa, South America) leading to an underestimate of $H_2$ by 20–30 ppbv in tropical regions. As indicated by *Sanderson et al.* [2003], soil diffusion and moisture also affect the $H_2$ uptake. In the tropics, the impact of NMHCs (and in particular of biogenic NMHCs as isoprene) on $CH_2O$ levels and hence on $H_2$ photochemical production is another potential cause for the underestimate obtained in the model.

### 3.2. Hydroxyl Radical

[48] Figure 20 illustrates the seasonal cycle of the globally averaged methane, methylchloroform, and HCFC-22 chemical lifetimes and OH concentration. As in the study by *Prather et al.* [2001], the global and annual mean photochemical lifetime is defined here as the global burden of the considered species divided by its global sink through OH oxidation. The global burden is integrated over the whole model domain and the chemical sink is integrated from the surface up to the model tropopause. On the basis of this definition, we calculate a global methane lifetime of 7.9 years in annual mean. This lifetime ranges from 6.5 years in July during the Northern Hemisphere summer to 9 years in January. The global methane lifetime is quite stable in our model and ranges between 7.921 and 7.953 years over the last five years of integration. This global methane lifetime is within 5% of the global number of 8.23 years reported by *Lawrence et al.* [2001] on the basis of the empirical OH field from *Spivakovsky et al.* [2000]. However, it is lower by 18% compared to the 9.6 years reported by *Prather et al.* [2001]. We note, however, that the spread of the calculated $CH_4$ lifetime among the models is large and the recent survey by *Prather et al.* [2001] provides a range of 6.5–13.8 years for this number. The global and annual $CH_3CCl_3$ and HCFC-22 lifetimes are 4.6 years and 10.3 years, respectively. The calculated global OH is $12.8 \times 10^5$ molecules $cm^{-3}$.

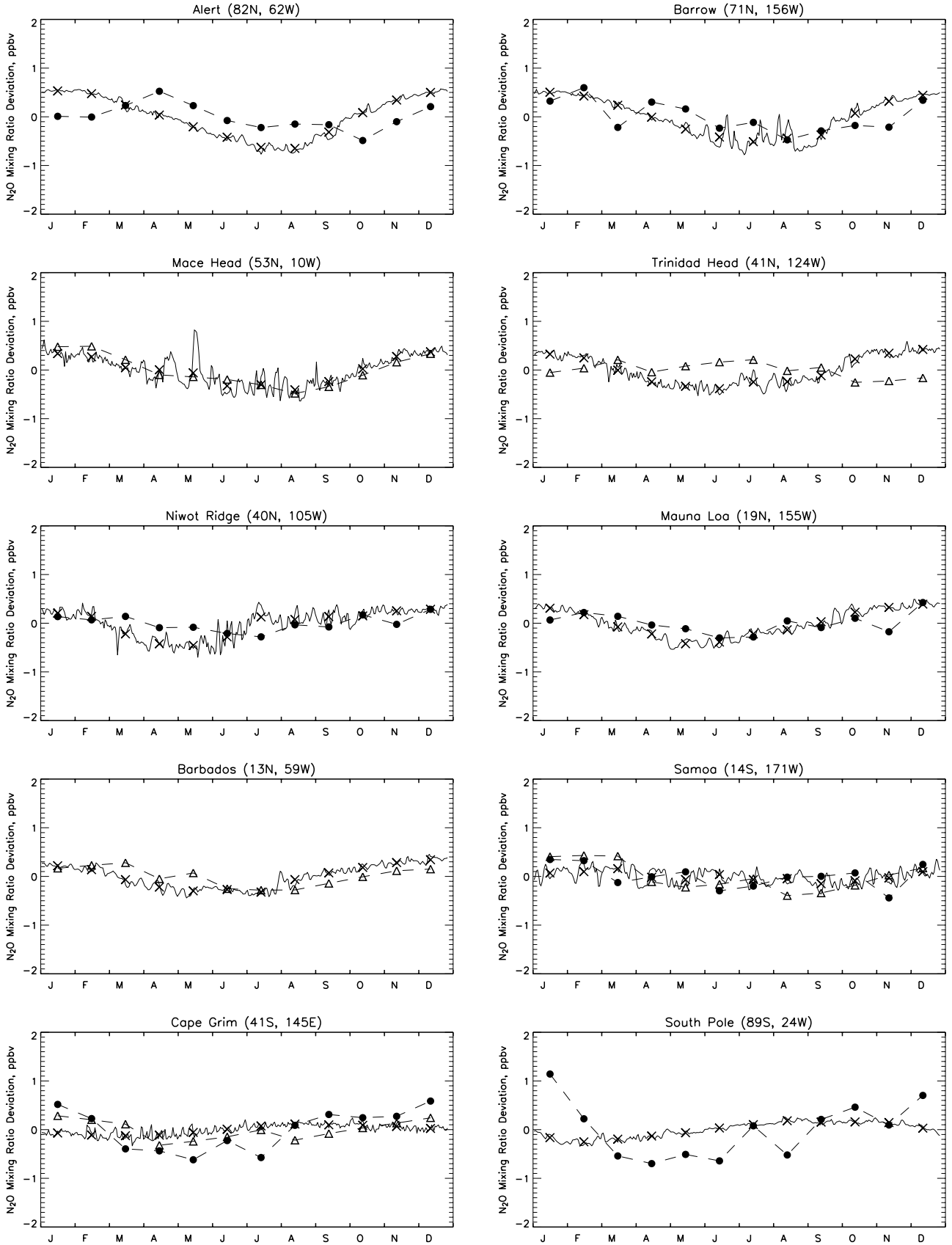


**Figure 17.** Calculated (solid line is day-to-day variation, and crosses denote monthly mean) and measured $N_2O$ mixing ratio deviation from annual mean ( ppbv) at selected surface sites. Measurements from the ALE-GAGE (triangles) [*Prinn et al.*, 2000] and CMDL [*Hall et al.*, 2001] (solid circles) networks.

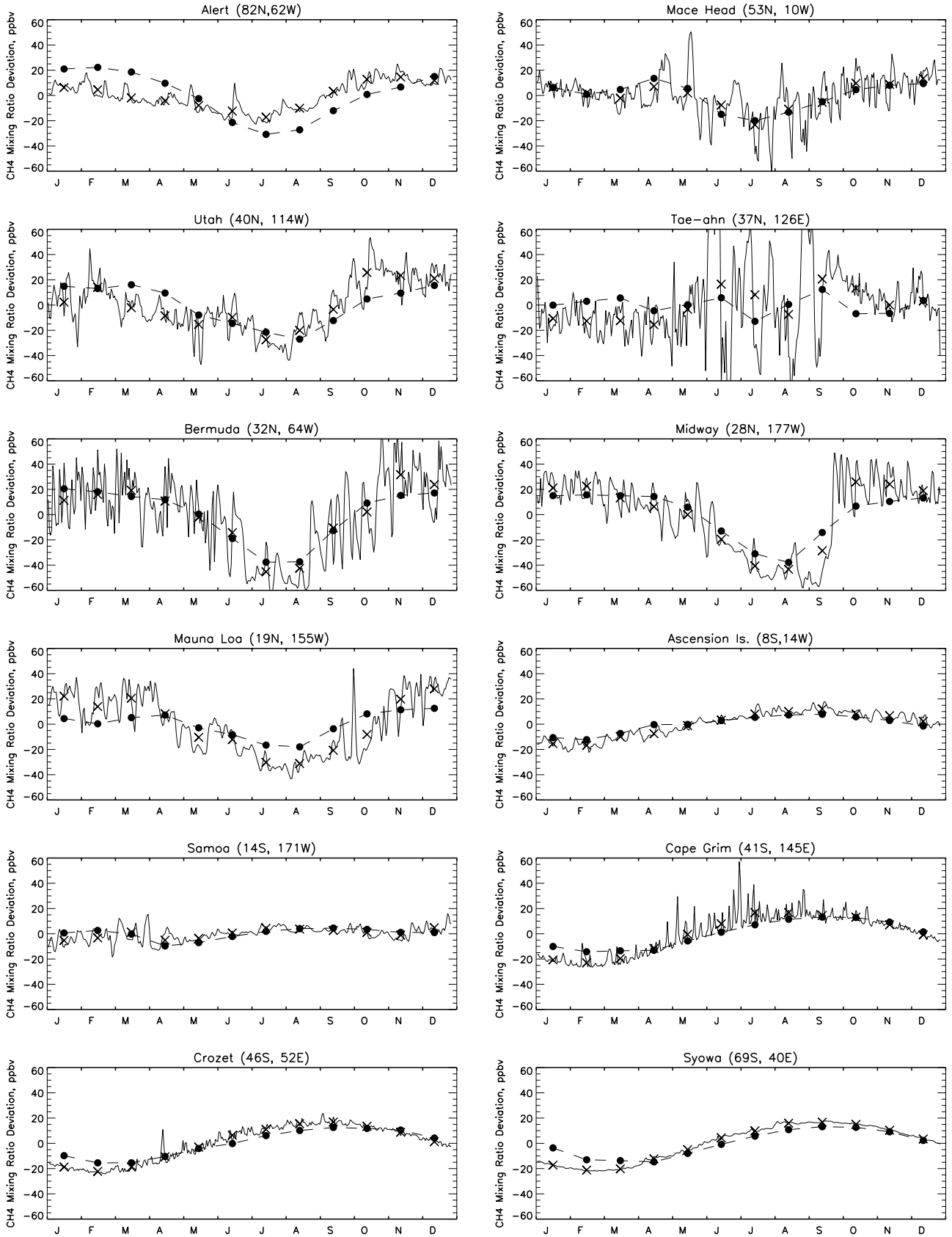


**Figure 18.** Calculated (solid line is day-to-day variation, and crosses denote monthly mean) and measured (by *Dlugokencky et al.* [1998] (solid circles) at the CMDL network stations) $CH_4$ mixing ratio deviation from annual mean (ppbv) at selected surface sites.

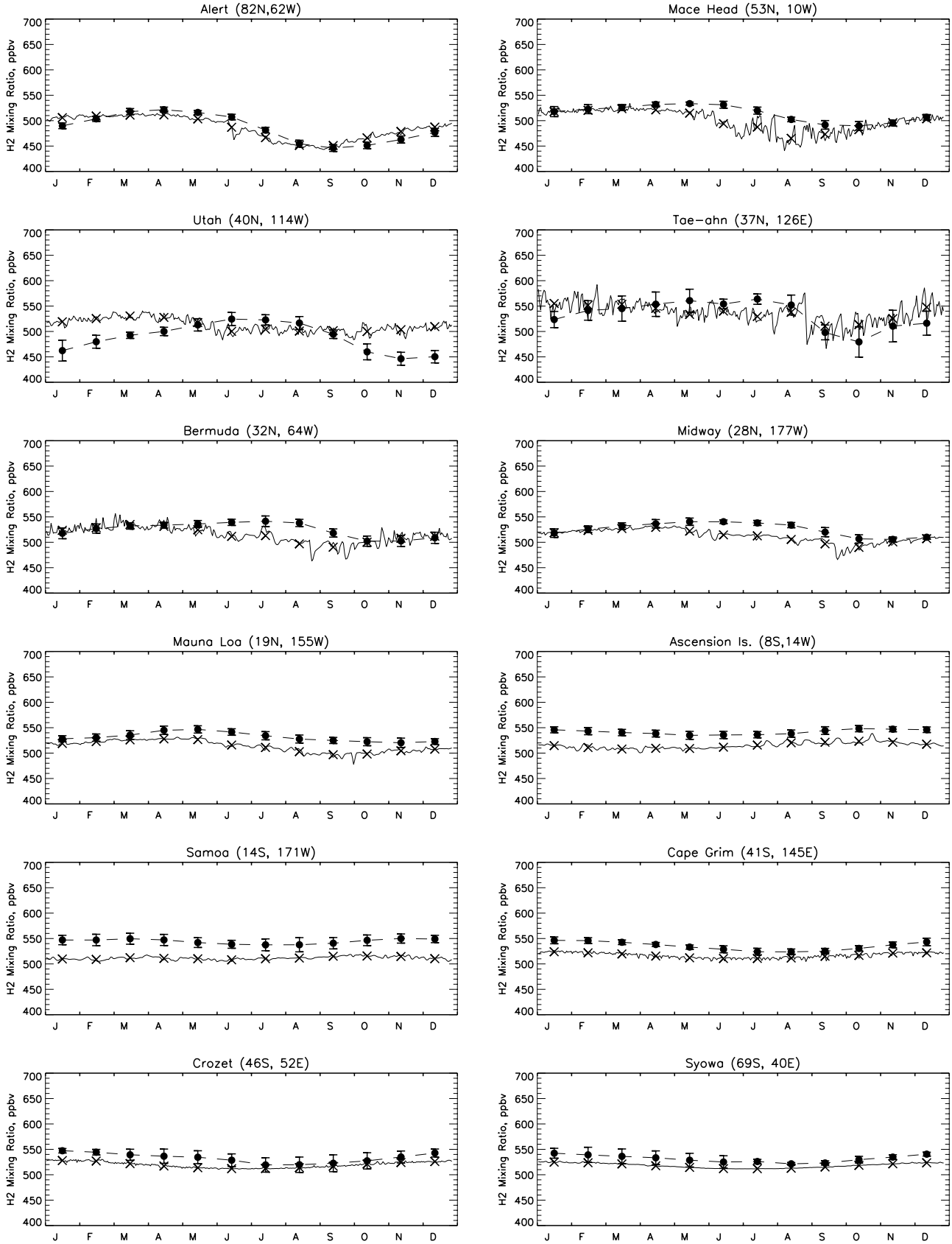


**Figure 19.** Calculated (solid line is day-to-day variation, and crosses denote monthly mean) and measured (by *Novelli et al.* [1999] (solid circles) at the CMDL network stations) $H_2$ mixing ratio (ppbv) at selected surface sites.

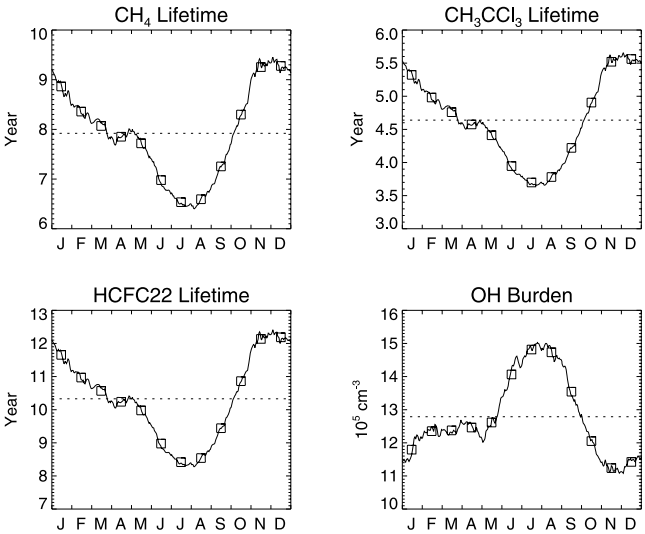


**Figure 20.** Seasonal cycle of methane, $CH_3CCl_3$, and HCFC22 global chemical lifetimes (years), and globally pressure-weighted OH concentration ($10^5$ molecules $cm^{-3}$).

Previous work has reported $CH_3CCl_3$ lifetimes against oxidation and derived from observations or from empirical OH fields of 5.5 and 6.0 years (*Spivakovsky et al.* [2000] and *Prinn et al.* [2001], respectively), or from global models of 5.1, 6.2, 7.3 years (from *Bey et al.* [2001], *Wang et al.* [1998], and *Mickley et al.* [1999], respectively). More recently values of 5.7 and 6.1 years have been reported by *Prather et al.* [2001] and *Montzka et al.* [2003], respectively. Comparison with these recent estimates of $CH_3CCl_3$ lifetime suggests that OH is too high by 19–25% in LMDz-INCA. As pointed out by *Lawrence et al.* [2001], different calculation methods for these numbers also lead to differences in the estimate reaching up 30% for the same metric. This feature has to be kept in mind when the comparison of our results with the previous estimates by *Prather et al.* [2001] and *Montzka et al.* [2003] is made. Additional information on OH, peroxides and formaldehyde is provided in the online auxiliary material.

### 3.3. Carbon Monoxide

[49] Figure 21 illustrates the monthly mean CO surface distribution for January and July conditions. Maximum

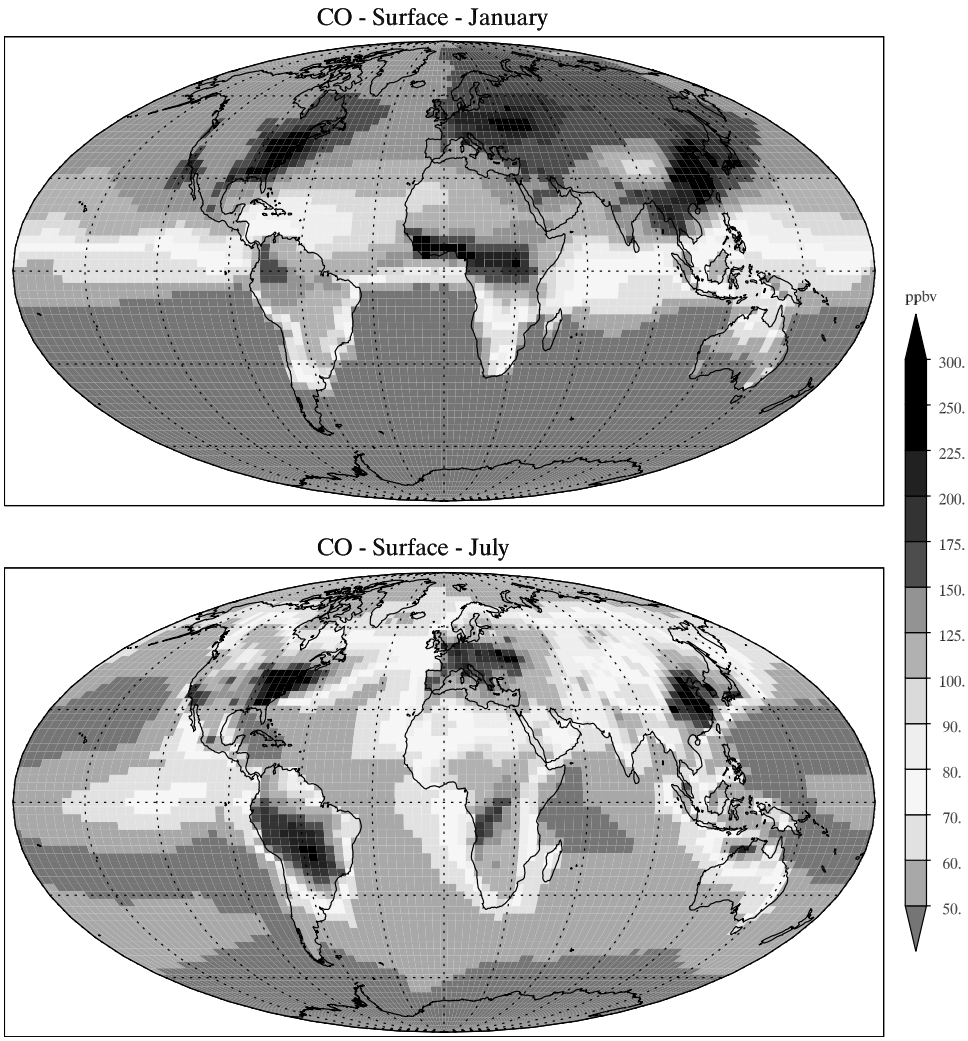


**Figure 21.** Distribution of carbon monoxide (CO) mixing ratio (ppbv) calculated at the surface in January and July. See color version of this figure at back of this issue.

mixing ratios reaching more than 300 ppbv are calculated over polluted regions in the Northern Hemisphere and over biomass burning areas in the tropics. A strong seasonal cycle associated with photochemical activity and consequent accumulation of CO during winter when its lifetime is longer is visible in the Northern Hemisphere. In tropical regions, the CO seasonal cycle is largely controlled by the location and timing of the burning season.

[50] Figure 22 provides an evaluation of the calculated CO surface distribution by comparing to the climatological measurements from CMDL at selected stations. The CO seasonal cycle simulated at the remote marine stations of Cape Grim, Crozet and Syowa agrees very well with the observations. Despite the lack of NMHCs, the model also simulates quite satisfactorily the mixing ratio over more polluted sites (Utah, Tae-ahn). At northern midlatitude stations (Mace Head, Bermuda), the model tends to underestimate CO by 10–20 ppbv during summer when photochemistry is more active. The underestimate is more pronounced and persists throughout the year at higher latitudes (Barrow). The model also tends to underestimate the CO mixing ratio by 10–30 ppbv at tropical stations (Samoa, Midway). This disagreement is mainly associated with the OH overestimate in the model leading to too much CO oxidation during its transport away from source regions. Figure 23 summarizes the comparison with most stations from the CMDL network and provides a scatter plot of model mixing ratios versus measurements. Overall, a fairly good correlation is reached ($r^2$ = 0.98). We note, however, that this good correlation is strongly driven by the good agreement obtained for low (remote stations) and high (polluted sites) CO mixing ratios. A large subsample of the data around 100 ppbv exhibits an underestimate of CO by 10–20 ppbv in LMDz-INCA. A very similar model-data comparison has been obtained by *Lawrence et al.* [1999]. Additional information on carbon monoxide evaluation is provided in the online auxiliary material.

### 3.4. Nitrogen Oxides

[51] Simulated monthly mean distributions of $NO_x$ are illustrated in Figure 24 for January and July. Maximum mixing ratios reaching more than 5 ppbv are calculated throughout the year over polluted regions (Northern America, Western Europe, and Southeast Asia). High mixing ratios reaching 2–3 ppbv are also calculated over biomass burning regions and exhibit a strong seasonal cycle following the burning season. Over the ocean, mixing ratios are generally in the range 10–25 pptv in the Southern Hemisphere. In the Northern Hemisphere, because of ship emissions, mixing rations are in the range 50–200 pptv over the northern Atlantic and Pacific. These values are in disagreement with most in-situ measurements made over the ocean. This feature has been discussed in detail by *Kasibhatla et al.* [2000], *Davis et al.* [2001], and *von Glasow et al.* [2002] and points toward missing processes as plume formation or heterogeneous reactions in the global models.

[52] Figure 25 compares the simulated profiles with the aircraft measurements from the data composites. The evaluation of simulated profiles with the data composites prepared by *Emmons et al.* [1997, 2000] is performed adopting the regions described by *Hauglustaine et al.* [1998] and averaging the model results over the given regions and during the duration of the campaigns. Table 6 provides a list of the regions used in this study with the corresponding latitude and longitude ranges. Considering the large variability in space and time, the calculated profiles show a general good agreement with the observations. The model reproduces the typical "C-shape" profiles with higher mixing ratios in the polluted boundary layer, decreasing mixing ratios as a function of altitude in the lower troposphere, and increase due to lightning emissions and stratospheric influence in the upper troposphere. We note however, an overestimate of the measurements collected during SONEX over the Atlantic and SUCCESS over the central United States in most of the troposphere.

[53] Previous work has emphasized the difficulty to simulate nitric acid in the models [*Hauglustaine et al.*, 1998; *Lawrence et al.*, 1999; *Bey et al.*, 2001]. The $HNO_3$ evaluation (Figure 26) confirms this difficulty over polluted regions. In these regions, the model tends to overestimate $HNO_3$ by a factor of 2 in the boundary layer (CITE and ABLE-3B campaigns) but also in the free troposphere (SONEX). This feature is also clear, but to a lesser extent, in regions affected by intense biomass burning activity. A much better agreement is obtained at more remote locations, and in particular during the PEM-West and PEM-Tropics campaigns. The overestimate over polluted regions is strongly dependent on the washout parameterization in the model [*Lawrence and Crutzen*, 1998; *Horowitz et al.*, 2003]. Gas phase nitric acid and aerosol nitrate partitioning and the role of heterogeneous processes are also potential reasons for this disagreement in the models [*Bauer et al.*, 2004]. In LMDz-INCA, the fact that PAN and other organic nitrates, which constitute a large fraction of the gas phase nitrogen present in the middle and upper troposphere, are not accounted for is also a plausible reason for the disagreement. As illustrated by *Bauer et al.* [2004], the PAN formation reduces $HNO_3$ by 10–25% over polluted regions. As illustrated in Figure 26 and already pointed out in the case of $^{210}Pb$, convective precipitation significantly affect $HNO_3$ at all locations. When only stratiform precipitation are considered, the $HNO_3$ mixing ratio increases by up to a factor of 8 in the tropical free troposphere.

[54] In order to investigate the contribution of each individual source to the $NO_x$ levels in the model, several sensitivity simulations have been performed. Instead of using tagged tracers as in the study by *Lamarque et al.* [1996], we run for each considered source of $NO_x$ a sensitivity simulation imposing a 10% increase in the source. The difference with the base case model results provides the sensitivity of the $NO_x$ distribution to the corresponding source ($\Delta NO_x/\Delta E_{NOx,i}$, where $E_{NOx,i}$ is the considered $NO_x$ emission), which can be extrapolated to account for the total (100%) emission (T. Berntsen, personal communication, 2002). This formulation is only valid to the extent that the 10% perturbation is small enough to avoid nonlinearities in the chemistry. The resulting zonal mean contribution of each source is depicted in Figure 27 for January and July conditions. Fossil fuel contributes to most of the $NO_x$ concentration throughout most of the troposphere north of about 50 degrees during northern winter. This contribution is reduced to 20–30% in July. Biomass burning (including biofuel) and soil emissions contribute to 20% and 10%, respectively, in tropical regions. Because of

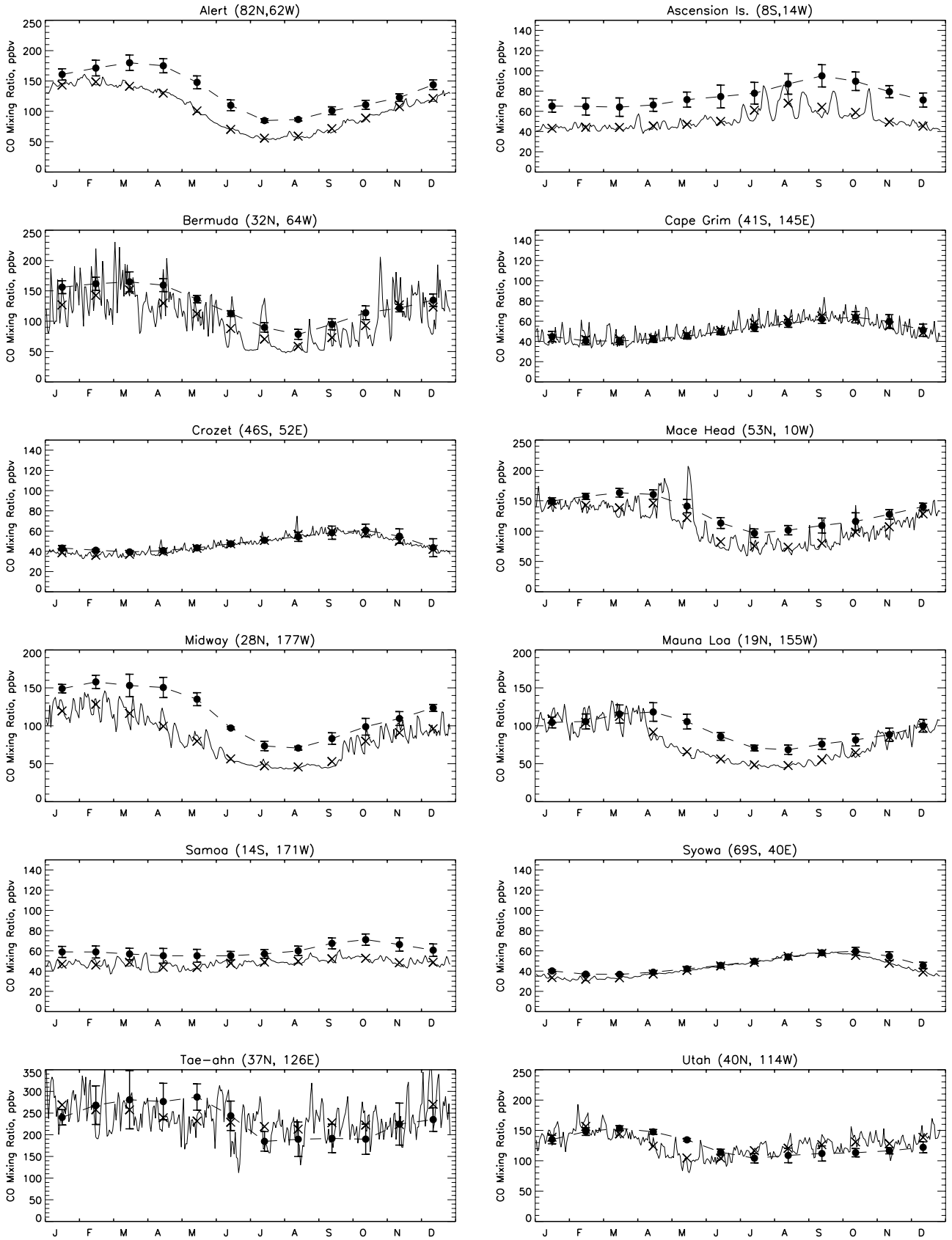


**Figure 22.** Calculated (solid line is day-to-day variation, and crosses denote monthly mean) and measured (by *Novelli et al.* [1994] (solid circles) at the CMDL network stations) CO mixing ratio ( ppbv) at selected surface sites.

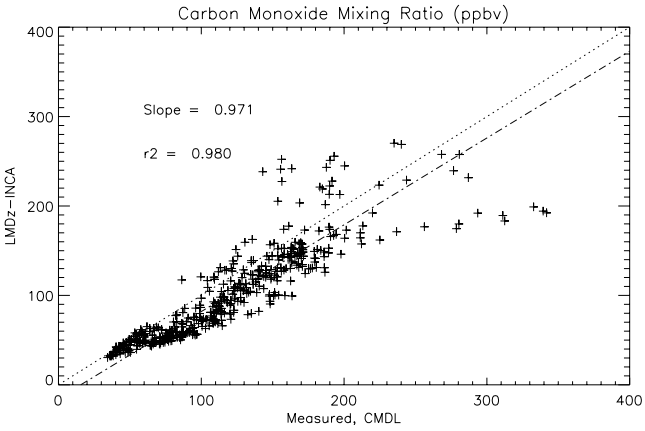


**Figure 23.** Scatterplot of CO calculated and measured at the CMDL stations (ppbv). The figure also shows the correlation coefficient ($r^2$) and slope of the linear regression (dash-dotted line). The dotted line denotes the 1:1 line.

rapid upward transport in the tropics, this contribution extends to the middle and upper troposphere. In July, biomass burning contributes to 20–30% to the nitrogen oxide levels in the southern tropics and boreal forest fires contribute to about 10% to $NO_x$ north of about 50°N. Lightning is a major contributor to $NO_x$ reaching more than 50% in the tropical upper troposphere during all seasons. In July, lightning contributes to 20–30% to the $NO_x$ levels in the Northern Hemisphere middle and upper troposphere. Stratospheric intrusion is also the other major contributor to $NO_x$ in the upper troposphere. At high latitudes in the Southern Hemisphere, this contribution extends down to the lower troposphere but remains confined to the upper troposphere in the Northern Hemisphere. Finally, aircraft emissions contribute to 40% to the $NO_x$ levels in the upper troposphere during the Northern Hemisphere winter. In July, when upward transport of surface sources and lightning are more intense, the relative contribution of aircraft decreases to 10%. Despite the simple approach adopted here to determine the relative individual contributions to the calculated $NO_x$ levels, these results provide a coherent view of the various processes involved and are consistent with the tagged tracer approach adopted in previous work. It should be noted that the contribution of several sources as fossil fuel or biomass burning will be affected when NMHCs and PAN formation are considered. As discussed by *Moxim et al.* [1996], PAN chemistry has little impact on the global-scale chemistry and contributes for about 10% to the $NO_x$ levels in the upper half of the troposphere where its lifetime is long. However, PAN can have regional and local influences. In particular, *Moxim et al.* [1996] indicate that $NO_x$ concentrations increase by up to a factor or 5 in the remote lower troposphere and show a spring maximum over areas of the North Atlantic and North Pacific oceans.

### 3.5. Ozone

[55] Figure 28 shows the ozone mixing ratio calculated at the surface level for January and July. As expected, maximum mixing ratios reaching 50–60 ppbv are calculated in summer over polluted regions in the Northern Hemisphere. This distribution is in agreement with previous modeling results [e.g., *Wang et al.*, 1998; *Hauglustaine et al.*, 1998; *Horowitz et al.*, 2003]. We note, however, that surface ozone is underestimated by 5–10 ppbv over the eastern United States where biogenic hydrocarbons contribute significantly to ozone formation during summer. The impact of biomass burning emissions is visible in the tropics and extends downwind of the source regions over the south Atlantic, the Indian and even Pacific oceans. Because of dry deposition at the surface and titration by NO, mixing ratios lower than 20 ppbv are calculated over the continents in the Northern Hemisphere during winter.

[56] Figure 29 provides an evaluation of the surface ozone mixing ratio by comparing with measurements at selected stations. For this specific comparison with surface measurements ozone has been averaged over the last five years of the simulation. The simulated seasonal cycle agrees fairly well with the observations showing a local springtime maximum at remote sites, a local summertime maximum at polluted sites and a peak during the biomass burning season in the tropics. The simulated mixing ratios reproduce generally well the observed values in extratropical and midlatitudes in the Northern Hemisphere (Mace Head, Bermuda, Hohenpeissenberg, Azores, Mauna Loa, Tateno). The model overestimates the springtime minimum observed at Barrow and attributed to bromine chemistry [*Barrie et al.*, 1988; *Wang et al.*, 1998]. In the Southern Hemisphere, the seasonal cycle is somewhat underestimated by LMDz-INCA at higher latitudes (Syowa, Cape Grim) and is in better agreement at lower latitudes (Samoa, Cape Point). In the tropics, the model tends to overestimate the observed mixing ratio at several stations (Cuiaba, Natal, Barbados) but not at Brazzaville. A similar disagreement has also been noted by *Wang et al.* [1998] and *Hauglustaine and Brasseur* [2001]. The origin of the disagreement is unclear and could be associated with a too weak ozone photochemical destruction over the ocean or surface dry deposition over the continents. As illustrated by *Wang and Shallcross* [2000] and *von Kuhlmann et al.* [2003], high isoprene concentrations tend to decrease ozone by 5–10 ppbv over South America and is another possible explanation for the overestimate obtained at some stations (Cuiaba, Natal) in LMDz-INCA.

[57] The zonal mean ozone distribution (Figure 30) shows higher ozone mixing ratios in the Northern Hemisphere. Minimum values lower than 15 ppbv are calculated in the lower troposphere at 50–60 in the Southern Hemisphere. In the tropics, advection and convective mixing transport ozone-poor air masses up to the middle and upper troposphere, and mixing ratios lower than 35 ppbv are calculated at 10–12 km. Intrusion from the stratosphere is visible along the isentropes across the subtropical tropopause discontinuity in both hemispheres. The vertical distribution of ozone simulated by LMDz-INCA is evaluated against ozone soundings in Figure 31 and 32. For this comparison with climatological ozone soundings, the model results have been averaged over the last 5 years of the simulation as was done for the comparison with surface $O_3$ measurements. The measurements are taken from the climatology described by *Logan* [1999]. The simulated vertical profiles (Figure 31) are close to the measurements or within their observed variability (±1 σ standard deviation) at many stations. At high northern latitudes (Alert, Churchill), the profiles are

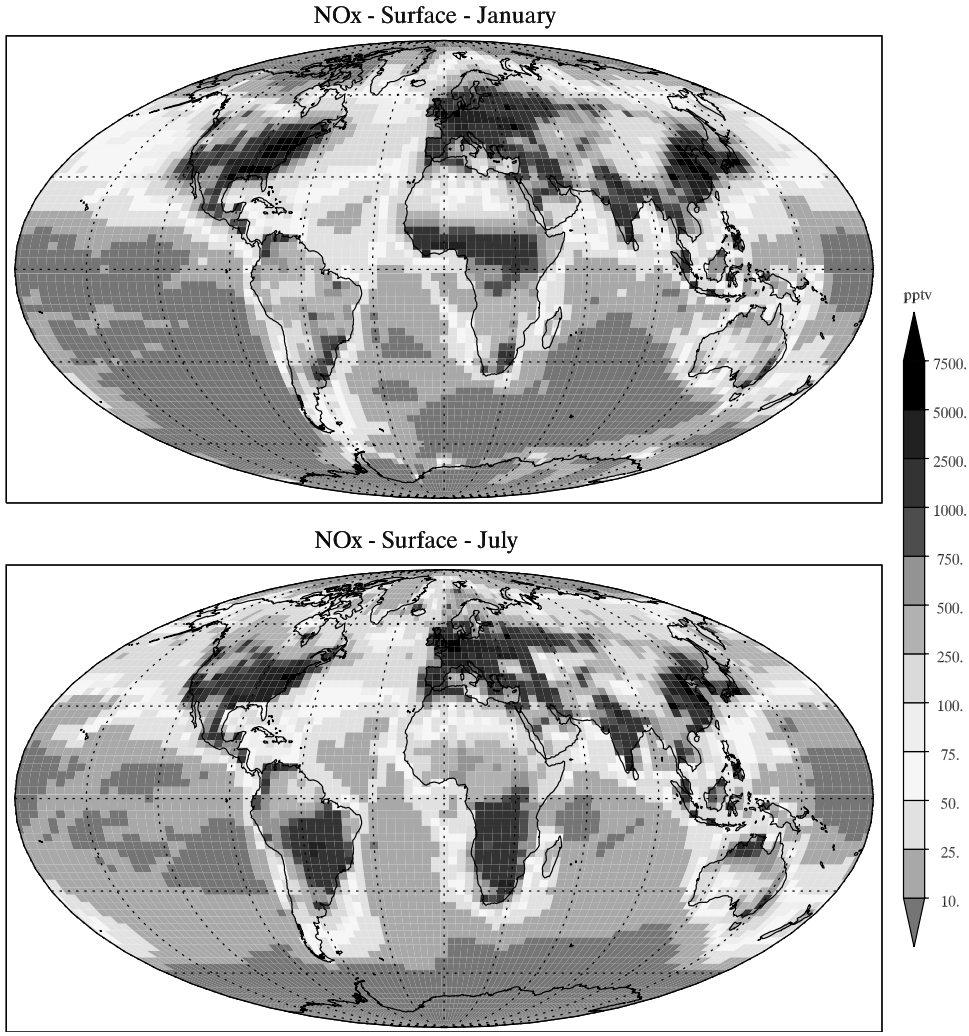


**Figure 24.** Distribution of $NO_x$ mixing ratio (pptv) calculated at the surface in January and July. See color version of this figure at back of this issue.

fairly well simulated during all seasons except during summer. During this period, as illustrated previously (Figure 16), the GCM overestimates the height of the tropopause and hence ozone is lower than the observations in the above 300 hPa. A similar problem associated with the tropopause location has also been encountered by *Shindell et al.* [2001]. This problem is still visible at some midlatitude stations to a much lesser extent (Hohenpeissenberg) but not at the Japanese stations (Sapporo). A good agreement is also obtained at several tropical and subtropical remote stations (Hilo, Samoa). The model tends, however, to underestimate ozone at stations affected by biomass burning emissions (Natal, Figure 32). At this station and others (Ascension, Pretoria, Brazzaville, not shown) the model also tends to smear out the vertical profiles and to underestimate ozone in the upper troposphere. These features suggest a strong convective diffusion in the GCM as already pointed out on the basis of the $^{222}$Rn evaluation. A closer insight into the simulated ozone seasonal cycle at selected stations is provided in Figure 33. On this figure, as was done by for instance by *Hein et al.* [2001], we illustrate the model variability by showing the day-to-day minimum and maximum ozone mixing ratio over the last five years of the simulation. This figure confirms the general good agreement with observations at most stations and the major discrepancies described above. At high northern latitudes, the model not only underestimates the monthly mean mixing ratio in summer in the upper troposphere but also underestimates the simulated variability at several stations (Alert, Resolute, Churchill). This low variability in simulated upper tropospheric ozone compared to observations has also been pointed out by *Law et al.* [2000] for several CTMs. In order to investigate the impact of different wind fields on the ozone variability, we have rerun LMDz-INCA nudging the wind horizontal components (u, v) toward the ECMWF assimilated winds with the technique described in section 2.1.1. For the results reported here we use the winds for year 1997. Several years have, however, been simulated (and reported, for example, by *Brunner et al.* [2003]) and lead to the similar following findings. As obvious from Figure 32, the nudging toward ECMWF winds provides a much larger day-to-day variability in simulated ozone in the upper troposphere (300 hPa). This feature is not only visible at high northern latitudes during spring (Alert, Resolute, Churchill) but also at midlatitude stations (Hohenpeissenberg, Sapporo). The constrained dynamics improves the

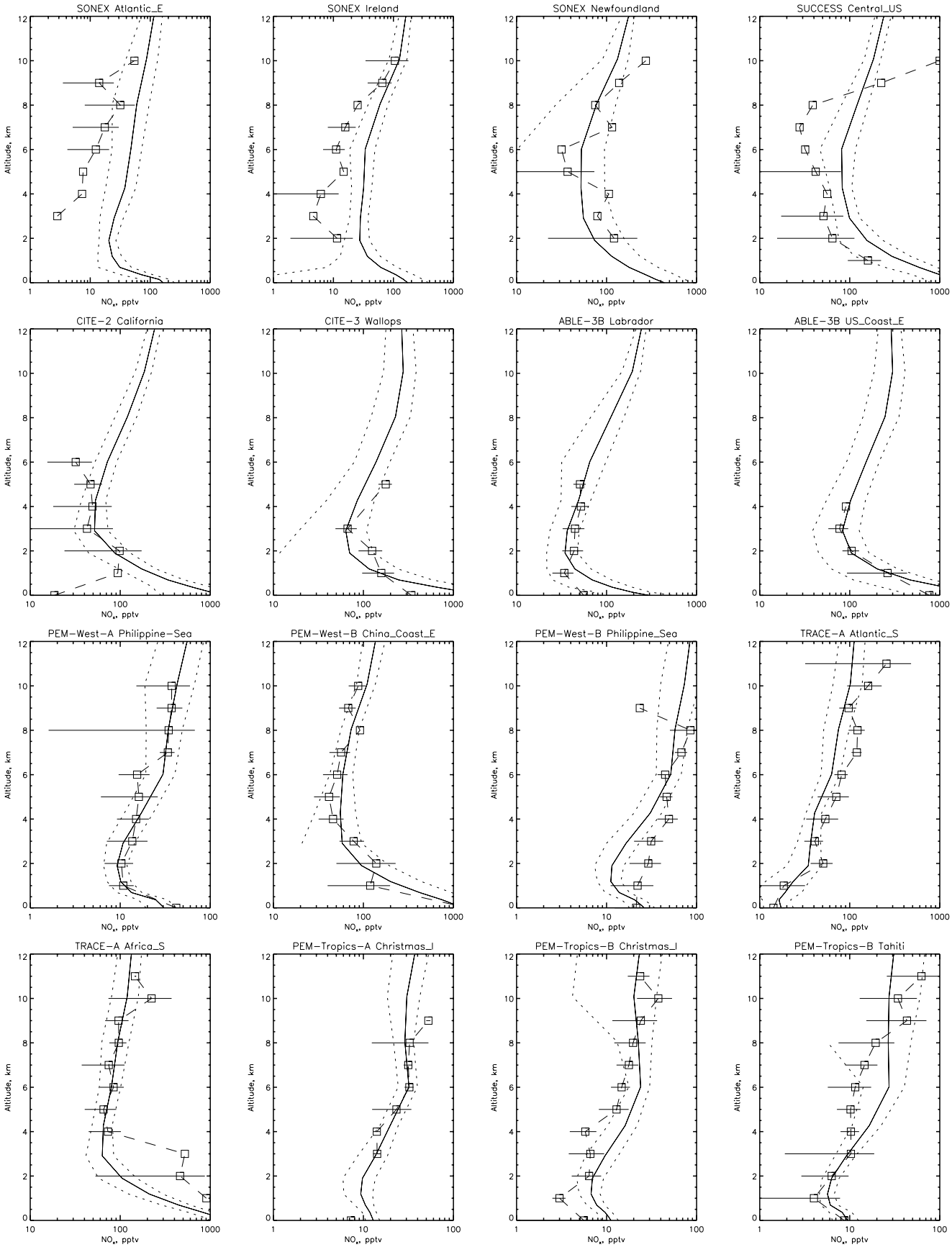


**Figure 25.** Calculated (solid and dashed lines are temporal mean and ±1σ standard deviation, respectively) and measured (during the GTE expeditions (squares)) $NO_x$ vertical profiles (pptv).

**Table 6.** Regions Used for the Vertical Profile Evaluation for $H_2O_2$, $CH_3OOH$, $CH_2O$, CO, NO, and $HNO_3$[a]

| Region | Latitude | Longitude | Expedition | Date |
|---|---|---|---|---|
| California | 35°N–45°N | 125°W–100°W | CITE-2 | 11 Aug. to 5 Sept. 1986 |
| Wallops | 30°N–40°N | 35°W–25°W | CITE-3 | 22 Aug. to 29 Sept. 1989 |
| U.S. coast East | 35°N–45°N | 80°W–70°W | ABLE 3B | 6 July to 15 Aug. 1990 |
| Labrador | 50°N–55°N | 60°W–45°W | ABLE 3B | 6 July to 15 Aug. 1990 |
| Pacific North | 15°N–35°N | 180°W–150°W | PEM-West A | 16 Sept. to 21 Oct. 1991 |
| Pacific Tropics West | 5°S–15°N | 155°E–165°E | PEM-West A | 16 Sept. to 21 Oct. 1991 |
| China coast East | 20°N–30°N | 115°E–130°E | PEM-West A | 16 Sept. to 21 Oct. 1991 |
| Japan coast East | 25°N–40°N | 135°E–150°E | PEM-West A | 16 Sept. to 21 Oct. 1991 |
| Philippine Sea | 5°N–20°N | 135°E–150°E | PEM-West A | 16 Sept. to 21 Oct. 1991 |
| China coast East | 20°N–30°N | 115°E–130°E | PEM-West B | 7 Feb. to 14 March 1994 |
| Japan coast East | 25°N–40°N | 135°E–150°E | PEM-West B | 7 Feb. to 14 March 1994 |
| Philippine Sea | 5°N–20°N | 135°E–150°E | PEM-West B | 7 Feb. to 14 March 1994 |
| Africa South | 25°S–5°S | 15°E–35°E | TRACE A | 21 Sept. to 26 Oct. 1992 |
| Atlantic South | 20°S–0° | 20°W–10°W | TRACE A | 21 Sept. to 26 Oct. 1992 |
| Africa coast West | 25°S–5°S | 0°–10°E | TRACE A | 21 Sept. to 26 Oct. 1992 |
| Brazil East | 15°S–5°S | 50°W–40°W | TRACE A | 21 Sept. to 26 Oct. 1992 |
| Brazil coast East | 35°S–25°S | 50°W–40°W | TRACE A | 21 Sept. to 26 Oct. 1992 |
| Central United States | 35°N–40°N | 100°W–95°W | SUCCESS | 15 April to 15 May 1996 |
| Fiji | 30°S–10°S | 170°E–170°W | PEM-Tropics A | 15 Aug. to 20 Sept. 1996 |
| Christmas Is. | 0°–10°N | 160°W–140°W | PEM-Tropics A | 15 Aug. to 20 Sept. 1996 |
| Hawaii | 10°N–30°N | 120°W–100°W | PEM-Tropics A | 15 Aug. to 20 Sept. 1996 |
| Tahiti | 20°S–0° | 160°W–130°W | PEM-Tropics A | 15 Aug. to 20 Sept. 1996 |
| Newfoundland | 45°N–55°N | 70°W–50°W | SONEX | 7 Oct. to 12 Nov. 1997 |
| Atlantic East | 35°N–45°N | 35°W–15°W | SONEX | 7 Oct. to 12 Nov. 1997 |
| Ireland | 50°N–60°N | 35°W–15°W | SONEX | 7 Oct. to 12 Nov. 1997 |
| Fiji | 30°S–10°S | 170°E–170°W | PEM-Tropics B | 6 March to 18 April 1999 |
| Christmas Is. | 0°–10°N | 160°W–140°W | PEM-Tropics B | 6 March to 18 April 1999 |
| Hawaii | 10°N–30°N | 170°W–150°W | PEM-Tropics B | 6 March to 18 April 1999 |
| Tahiti | 20°S–0° | 160°W–130°W | PEM-Tropics B | 6 March to 18 April 1999 |
| Easter Is. | 40°S–20°S | 120°W–100°W | PEM-Tropics B | 6 March to 18 April 1999 |

[a]Based on *Emmons et al.* [2000].

simulation of the tropopause height and higher ozone mixing ratios are calculated during summer at high-latitude locations. The use of assimilated winds does not necessarily improves the overall simulation of ozone in the model. The increased variability obtained in the upper troposphere results probably from noise introduced in the wind fields after the successive interpolations to the LMDz model grid and, as will be illustrated below, the global and annual ozone influx from the stratosphere to the troposphere is significantly increased by the nudged circulation.

[58] As described in section 2.2.5, a ''stratospheric ozone'' tracer has been included in LMDz-INCA in order to estimate the contribution of the stratospheric influx to the ozone levels calculated in the troposphere. Figure 33 provides such an estimate as a function of season in the lower and upper troposphere and for both the climatological and nudged simulations. In the upper troposphere (300 hPa), more ozone originating from the stratosphere is present in the nudged version at high northern latitudes in summer. The seasonal cycle of the stratospheric contribution and tropopause location is also modified with a more clearly pronounced maximum during springtime at high latitudes in the Northern Hemisphere. A similar finding is also obtained but to a lesser extent in the Southern Hemisphere. In the lower troposphere (800 hPa), a minimum contribution of stratospheric ozone of less than 20–25% is predicted during summer at midlatitudes in the Northern Hemisphere when photochemical production is at maximum. At high northern latitudes, a stratospheric contribution reaching more than 60% is calculated during spring. The effect of the nudging is still visible at this altitude with a stratospheric contribution larger by 10–15% in this case. In the Southern Hemisphere, the stratospheric contribution is generally larger than 40% all year round south of about 40 degrees. In the tropics, stratospheric ozone contributes for less than 30% during almost all the year.

[59] Table 7 provides the annual budget of ozone in the troposphere (defined as the domain extending from the surface up to 200 hPa) calculated with LMDz-INCA. This budget is calculated for total odd oxygen ($O_z = O_3 + O(^1D) + O(^3P) + OH + HO_2 + NO_2 + 2 \times NO_3 + 3 \times N_2O_5 + 2 \times HNO_3 + 2 \times HNO_4$) to account for cycling within the family. However, since $O_3$ is the most abundant component of $O_z$ in most of the considered domain, the $O_z$ and $O_3$ budgets can be viewed as equivalent. The global photochemical production and loss total 4486 and 3918 Tg/yr, respectively. More than 60% of the production occurs in the Northern Hemisphere. The difference between these two big numbers provides a net photochemical production of 567 Tg/yr. These estimates vary significantly among the models. Our esti-

**Figure 26.** Calculated (solid and dashed lines are temporal mean and ±1σ standard deviation, respectively) and measured (during the GTE expeditions (squares and triangles)) $HNO_3$ vertical profiles (pptv). Model results obtained when convective precipitation is suppressed are also shown for comparison (crosses and long-dashed line).

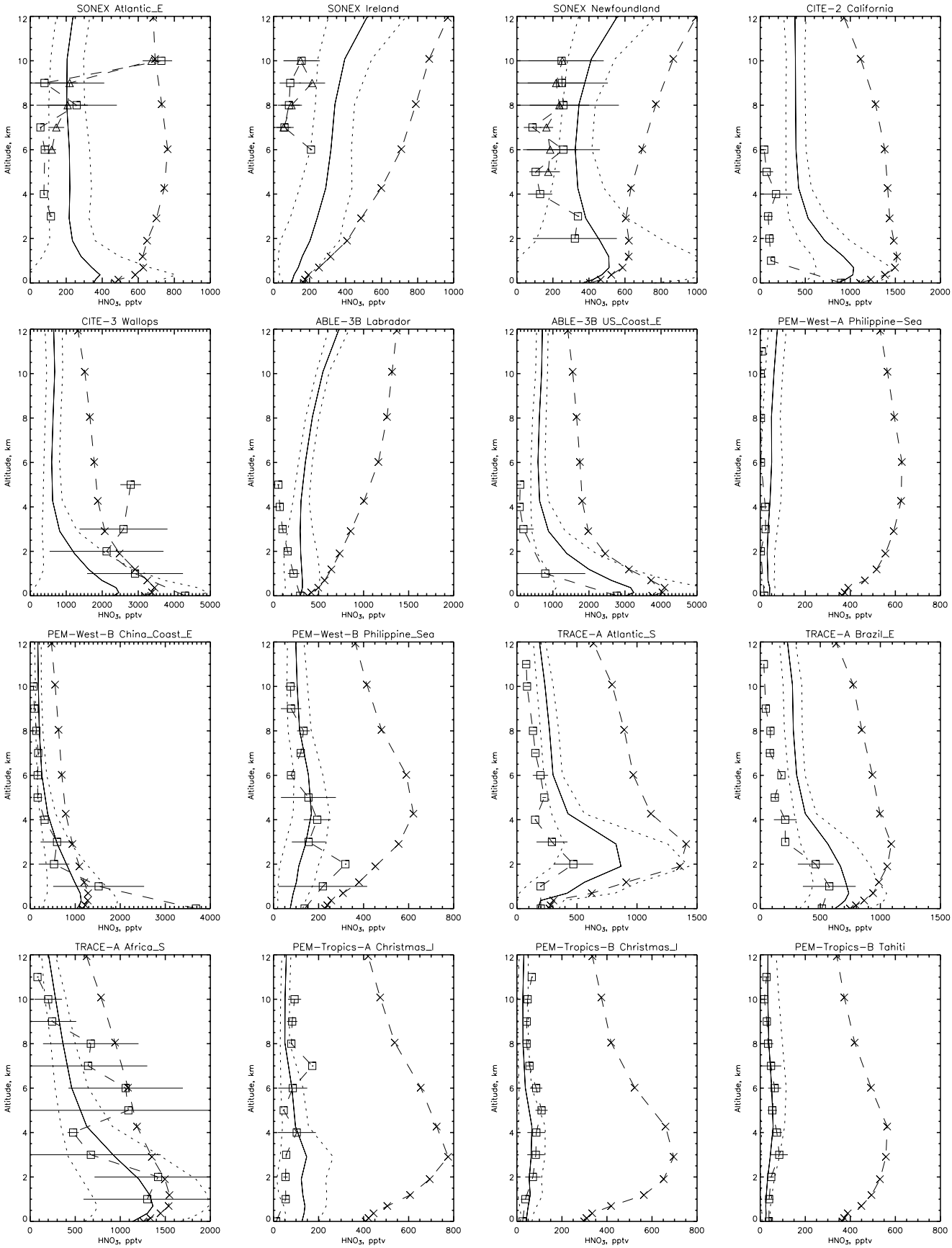
SONEX Atlantic_E
SONEX Ireland
SONEX Newfoundland
CITE-2 California
CITE-3 Wallops
ABLE-3B Labrador
ABLE-3B US_Coast_E
PEM-West-A Philippine-Sea
PEM-West-B China_Coast_E
PEM-West-B Philippine_Sea
TRACE-A Atlantic_S
TRACE-A Brazil_E
TRACE-A Africa_S
PEM-Tropics-A Christmas_I
PEM-Tropics-B Christmas_I
PEM-Tropics-B Tahiti
Altitude, km
HNO3, pptv

**Figure 26.**

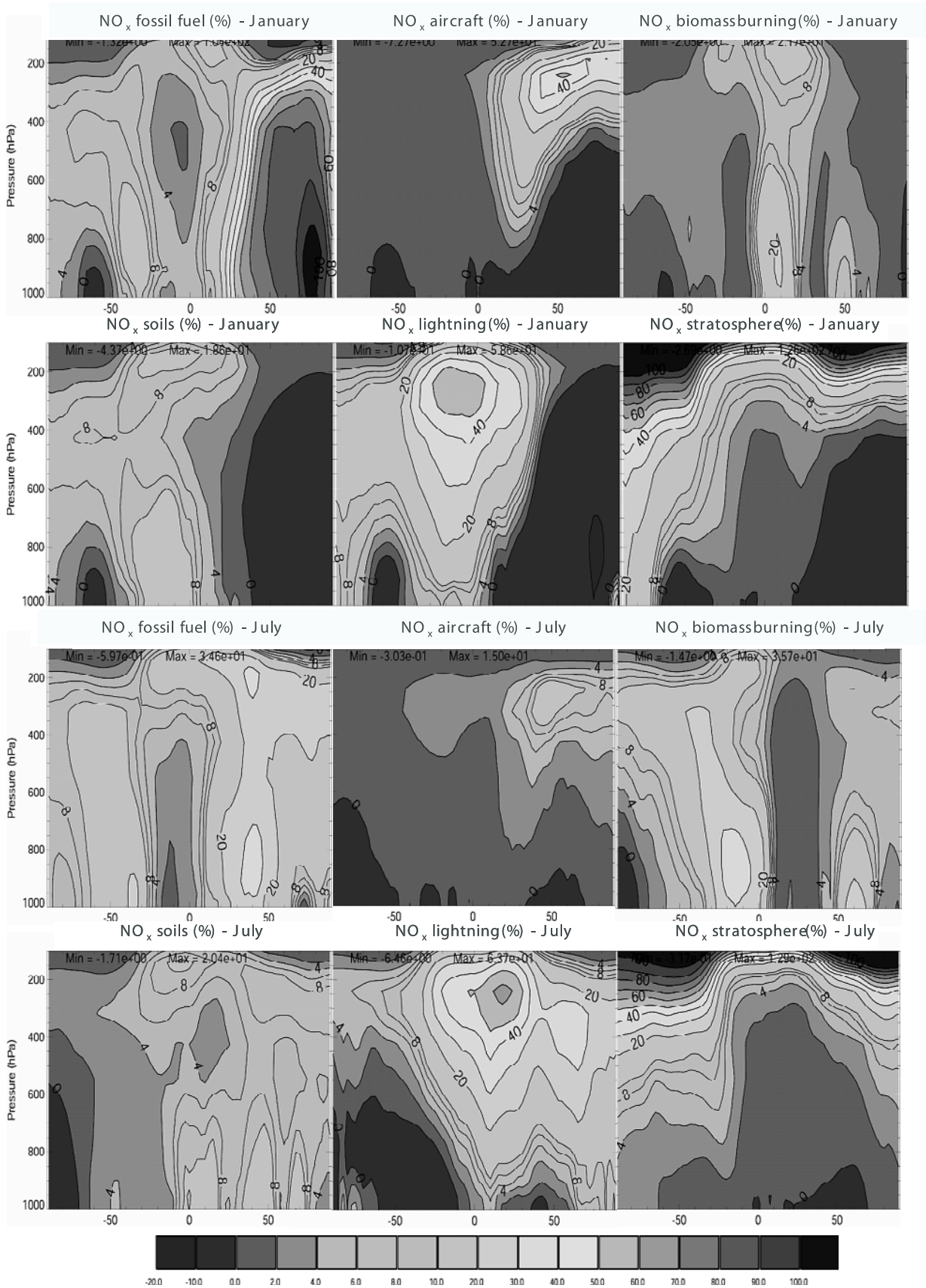


**Figure 27.** Percentage contribution of each individual source to the zonal mean $NO_x$ mixing ratio calculated for January and July conditions. See color version of this figure at back of this issue.

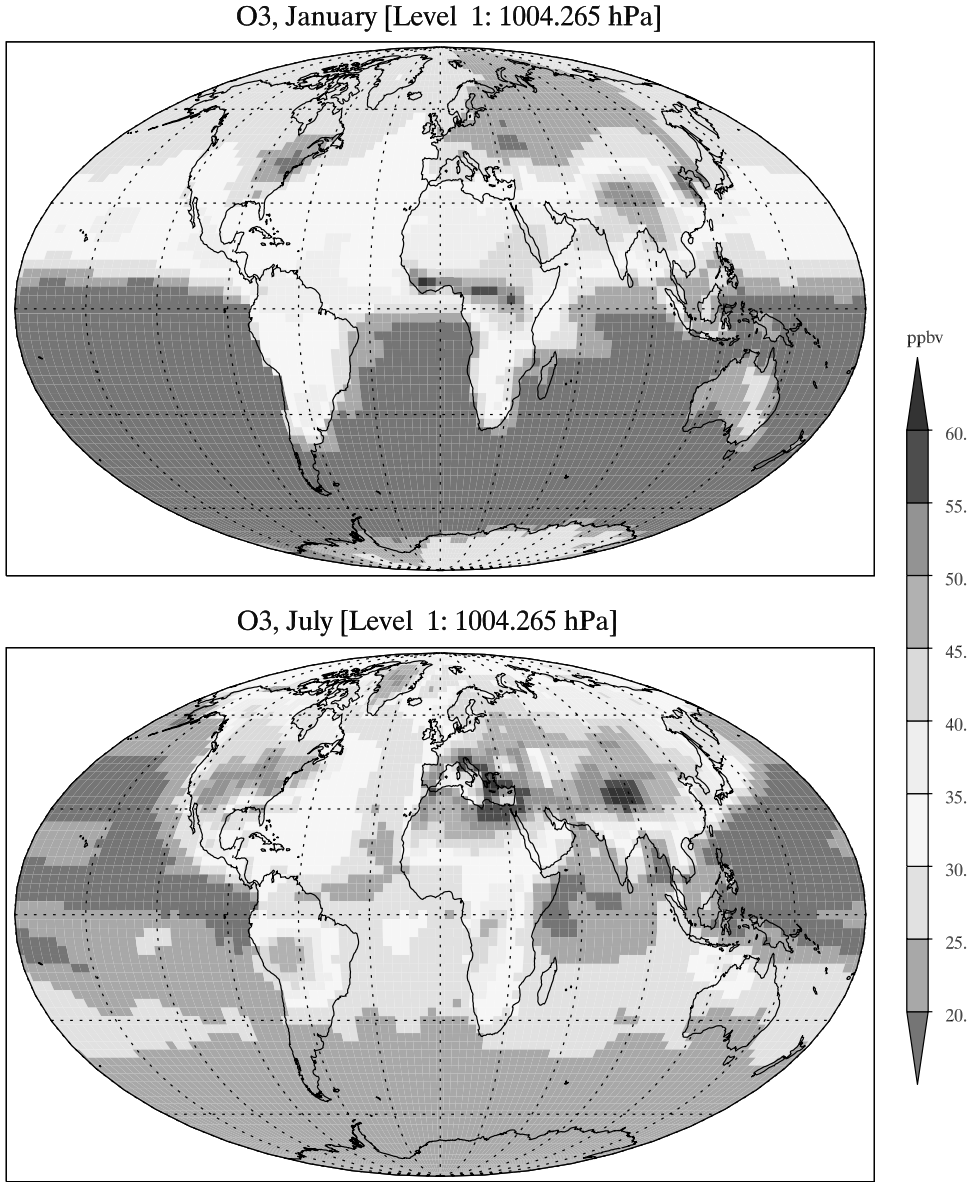


**Figure 28.** Distribution of $O_3$ mixing ratio (ppbv) calculated at the surface in January and July. See color version of this figure at back of this issue.

mate is in the range of the numbers compiled by *Prather et al.* [2001]. The stratospheric influx contributes for 523 Tg/yr. This value is in the range provided by previous estimates [*Murphy et al.*, 1993; *Gettelman et al.*, 1997; *McLinden et al.*, 2000; *Prather et al.*, 2001]. A slightly higher influx (53%) is calculated in the Southern Hemisphere. Dry deposition removes 1090 Tg/year. The photochemical ozone lifetime calculated on the basis of the tropospheric ozone burden of 296 Tg and the photochemical destruction is 27.6 days. These budget terms are given for the last year of the model simulation and vary only by 1–2% over the last five years of the simulation. The ozone production and destruction terms are in the range 4464–4531 and 3901–3962 Tg/yr, respectively, over the 5 years. The ozone burden ranges from 295 to 299 Tg over the same period. In the nudged version of the model, as a consequence of the larger variability illustrated above which indicates more stratospheric air intrusions into the troposphere, a larger influx of 783 Tg is calculated. Both the ozone photochemical production and destruction depend on the ozone background concentrations. In both hemispheres the photochemical loss is increased in the nudged version. The production slightly decreases in both hemispheres because

**Figure 29.** Observed (squares) and calculated (solid line is day-to-day variation, and crosses denote monthly mean) seasonal cycle of $O_3$ mixing ratio (ppbv) at selected surface stations. Measurements are taken from *Oltmans and Levy* [1994] and *Logan* [1999].

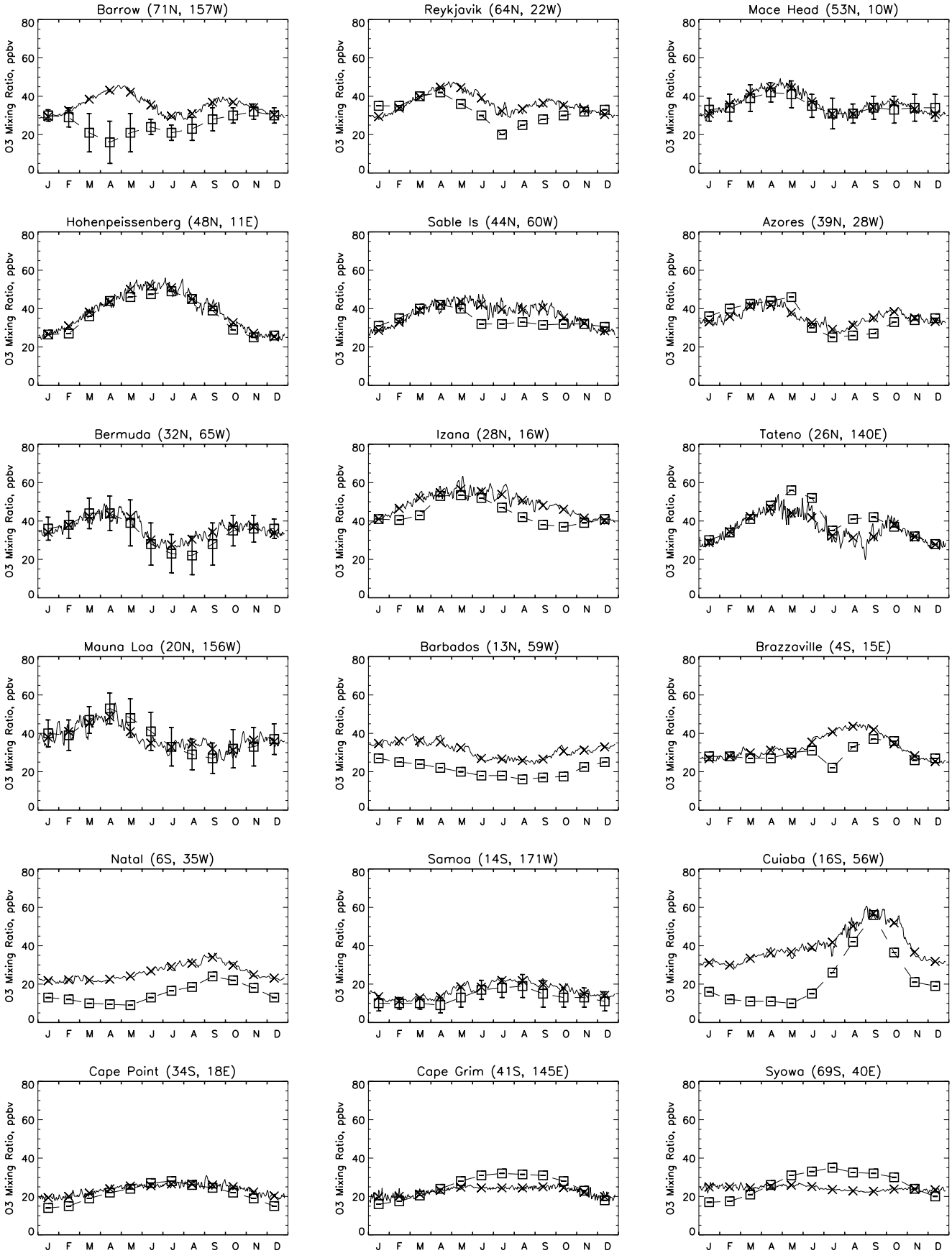
Barrow (71N, 157W)
Reykjavik (64N, 22W)
Mace Head (53N, 10W)
Hohenpeissenberg (48N, 11E)
Sable Is (44N, 60W)
Azores (39N, 28W)
Bermuda (32N, 65W)
Izana (28N, 16W)
Tateno (26N, 140E)
Mauna Loa (20N, 156W)
Barbados (13N, 59W)
Brazzaville (4S, 15E)
Natal (6S, 35W)
Samoa (14S, 171W)
Cuiaba (16S, 56W)
Cape Point (34S, 18E)
Cape Grim (41S, 145E)
Syowa (69S, 40E)
O3 Mixing Ratio, ppbv
0
20
40
60
80
J F M A M J J A S O N D

**Figure 29.**

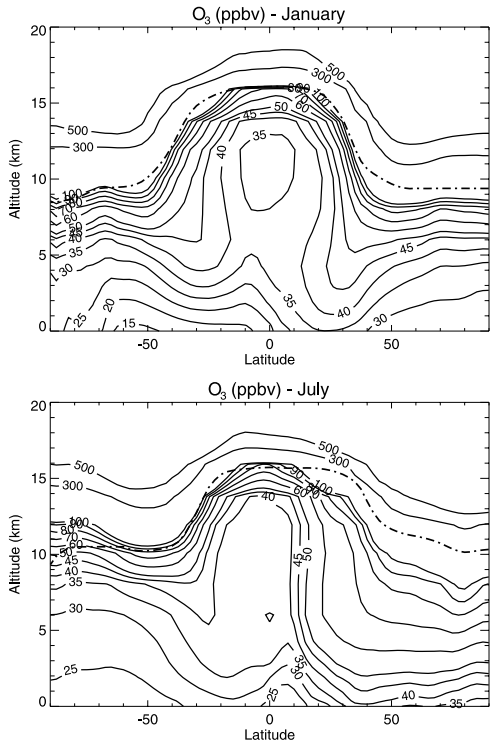


**Figure 30.** Zonally averaged $O_3$ mixing ratio (ppbv) cross sections calculated for January and July conditions. The dash-dotted line indicates the model tropopause.

of a lower $[NO]/[NO_2]$ concentration ratio at higher ozone background levels. Overall, the larger stratospheric influx leads to a decreased global net ozone photochemical production of 299 Tg.

## 4. Conclusion

[60] In this paper, we provide a first description and evaluation of the LMDz-INCA model. This model couples on-line the Laboratoire de Météorologie Dynamique general circulation model (LMDz) and the Interaction with Chemistry and Aerosols (INCA) model. The current version of LMDz-INCA runs with a horizontal resolution of 3.8 degrees in longitude and 2.5 degrees in latitude and 19 vertical levels from the surface to the level of 3 hPa. The model can be constrained by assimilated meteorology imposing a relaxation of the wind horizontal components toward ECMWF fields. In this first version of the model, a $CH_4-NO_x-CO-O_3$ chemical scheme representative of the background chemistry of the troposphere is considered. The model calculates the distribution of tropospheric ozone and its precursors as well as the main greenhouse gases and several inert tracers allowing the evaluation of transport and physical processes. Surface emissions are based on state-of-the-art inventories and include the contribution of fossil fuel and biofuel, biomass burning, and natural (oceanic, soil, continental biosphere) emissions. Lightning emissions and surface dry deposition velocities are calculated interactively. The model is run for climatological conditions and the results are evaluated by thorough comparison with available observations.

[61] Several inert or long-lived tracers ($CO_2$, $SF_6$, CFC-11, $^{85}Kr$) have been used to evaluate the interhemispheric exchange time. On the basis of these various tracers, we derive an exchange time in the range 1.13–1.38 years based on surface mixing ratios and of 0.70–0.82 years based on pressure-weighted hemispheric mean mixing ratios. The comparison with previous work indicates that the model provides an efficient large-scale transport and mixing and therefore underestimates the meridional gradient of tracers. The evaluation of $^{222}Rn$ with surface stations and selected vertical profiles indicates that the model reproduces most of the observed features during summer with a too efficient mixing out of the boundary layer during winter over continental stations. Sensitivity simulations performed in this study have confirmed the importance of convective and boundary layer mixing on the distribution of tracers. The model performance in terms of wet scavenging simulation has been investigated by comparing $^{210}Pb$ calculated concentrations with the measurements. This comparison reveals that the model captures fairly well the seasonal cycle observed at many sites. The model tends, however, to produce a too efficient wet scavenging during summer in the Northern Hemisphere. This feature is also confirmed by the comparison of simulated nitrogen wet deposition with surface network measurements and point toward overestimated precipitation during summer in the Northern Hemisphere in the GCM. Even if the general patterns of the nitrogen deposition are correctly reproduced by the model, scavenging of soluble species remains a major source of uncertainty in current global models. In particular, a sensitivity study performed with the model illustrates the key role played by convective precipitation on the global-scale distribution of soluble species.

[62] Calculated greenhouse gas distributions do not feedback on climate in this version of LMDz-INCA. The coupling will be considered in a future version of the model in order to investigate climate-chemistry interactions. The evaluation of long-lived greenhouse gas ($N_2O$, $CH_4$) distributions performed in this study indicates that the a priori surface emission inventories and oxidants considered in the present model version provide a reasonable agreement with observations as far the seasonal cycle and variability of these species are concerned. The global and annual mean methane (7.9 years) and methylchloroform (4.6 years) chemical lifetimes calculated with LMDz-INCA suggest that the global OH of $12.8 \times 10^5$ molecules $cm^{-3}$ is possibly too high by about 20% in the model. This disagreement with previous estimates is attributed to the missing nonmethane hydrocarbons in the model which tends to decrease the $OH/HO_2$ concentration ratio.

[63] Despite the lack of NMHCs, the model simulates quite satisfactorily the distribution and seasonal cycle of CO at remote marine sites and at more polluted continental locations. The model tends, however, to underestimate CO in tropical regions and during summer in the Northern Hemisphere. We attribute this discrepancy to the uncertainty associated with the estimate of indirect CO surface emissions from biogenic and biomass burning NMHCs as well as the high OH simulated in LMDz-INCA. The comparison with observed vertical profiles indicates that $NO_x$ concentrations are generally well simulated by the model. The evaluation of $HNO_3$ reveals an overestimate of the measure-

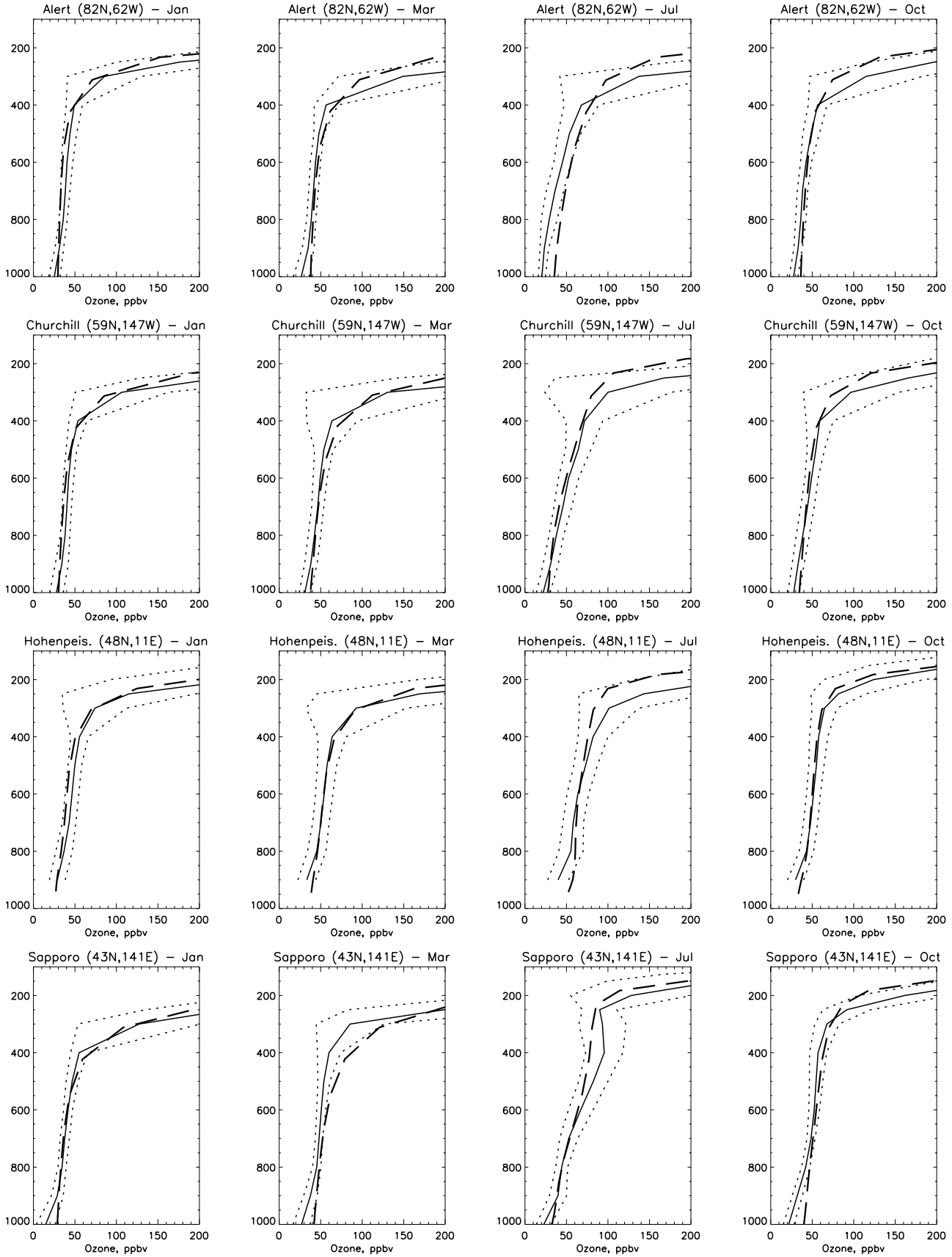


**Figure 31.** Model-calculated (long-dashed line) and measured (solid and dotted lines are temporal mean and ±1σ standard deviation, respectively) ozone vertical profiles (ppbv) at eight stations for January, March, July, and October. Observations were compiled by *Logan* [1999].

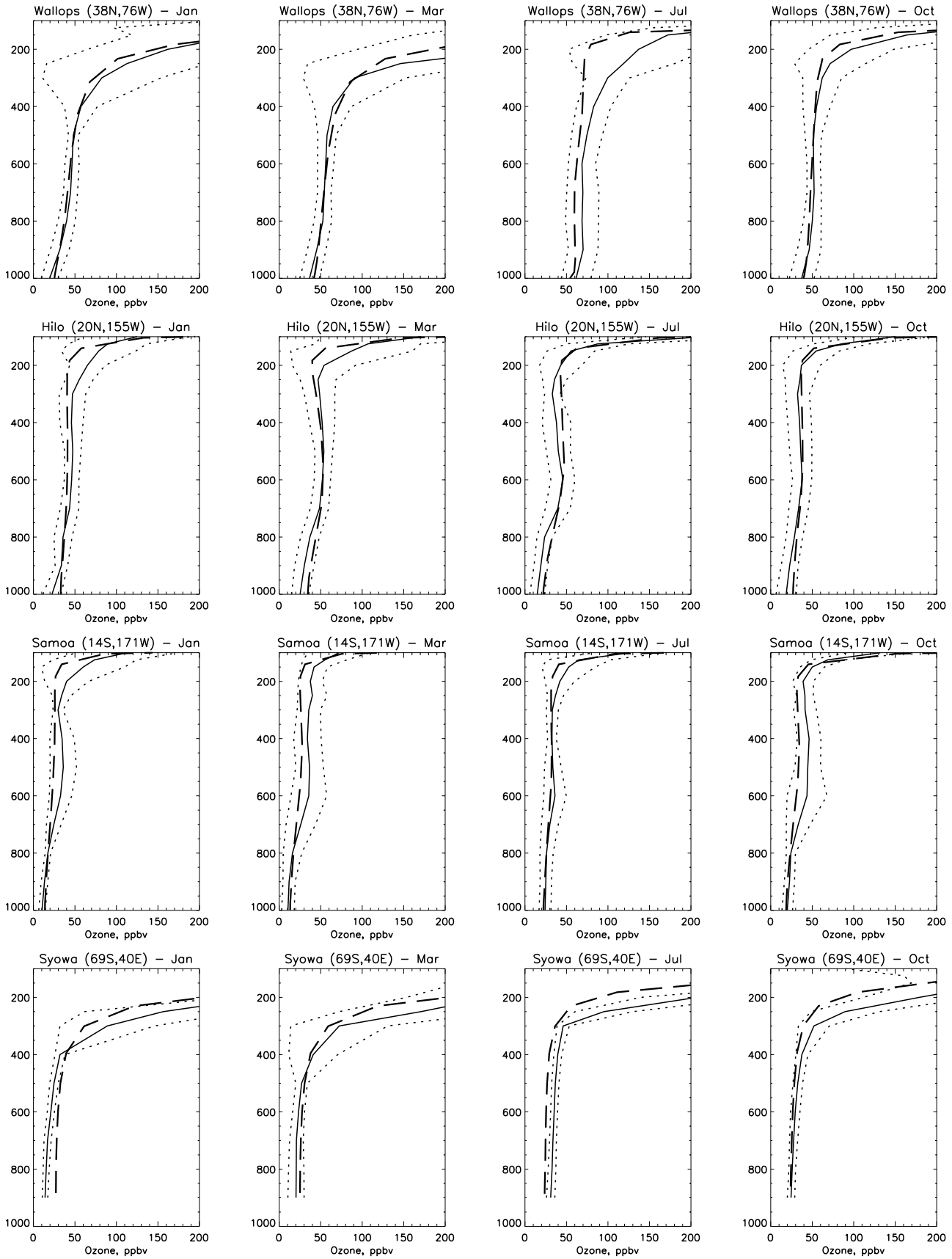


**Figure 31.** (continued)

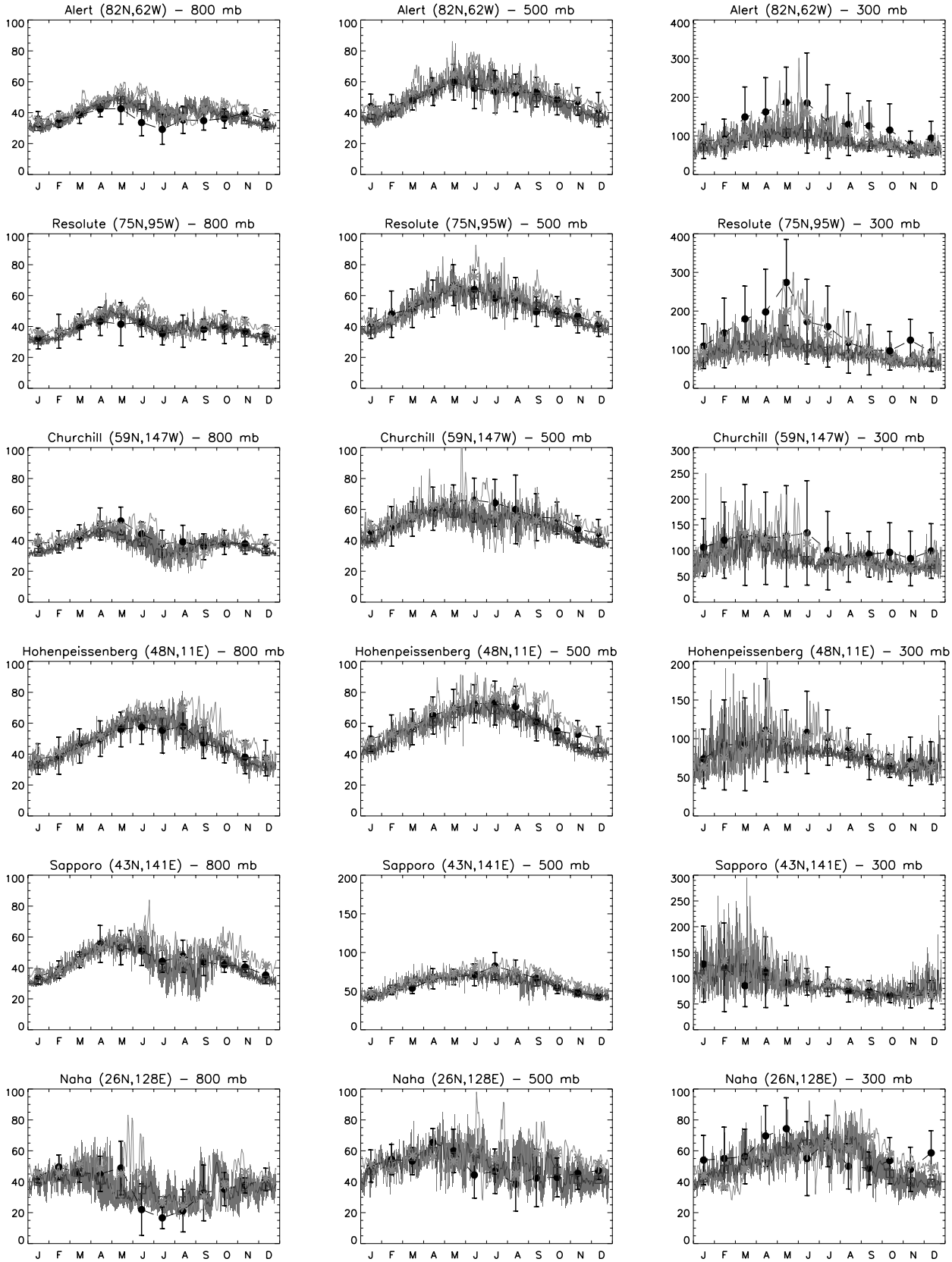


**Figure 32.** Measured (solid circles) and calculated (solid line is day-to-day variation, and crosses denote monthly mean) seasonal cycle of $O_3$ mixing ratio ( ppbv) at 12 stations and at 800, 500, and 300 hPa. Blue, base case model simulation; red, simulation with the nudged GCM (year 1997). The shaded blue area provides the day-to-day minimum and maximum ozone mixing ratio over the last 5 years of the simulations. Observations were compiled by *Logan* [1999]. See color version of this figure at back of this issue.

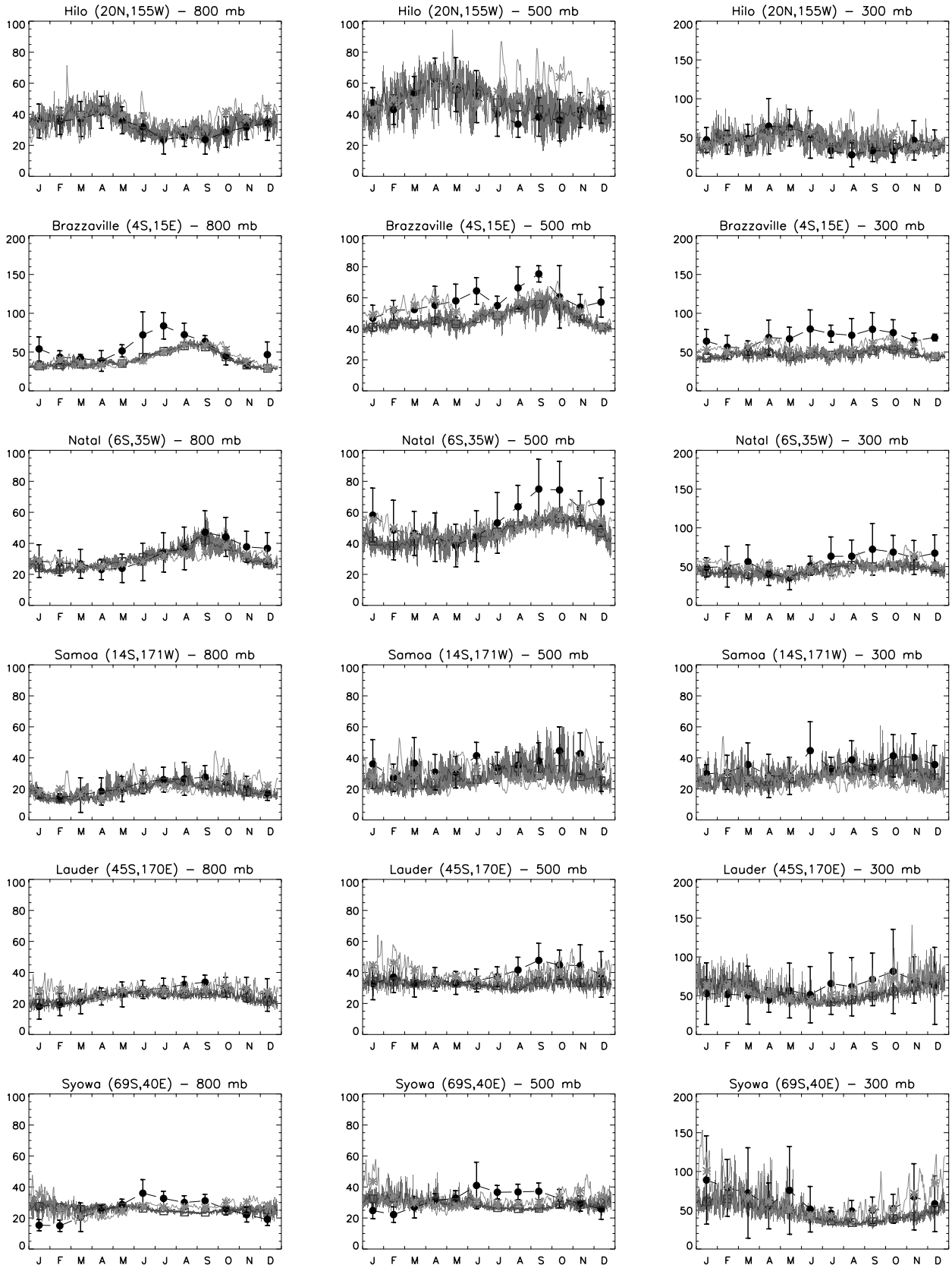


**Figure 32.** (continued)

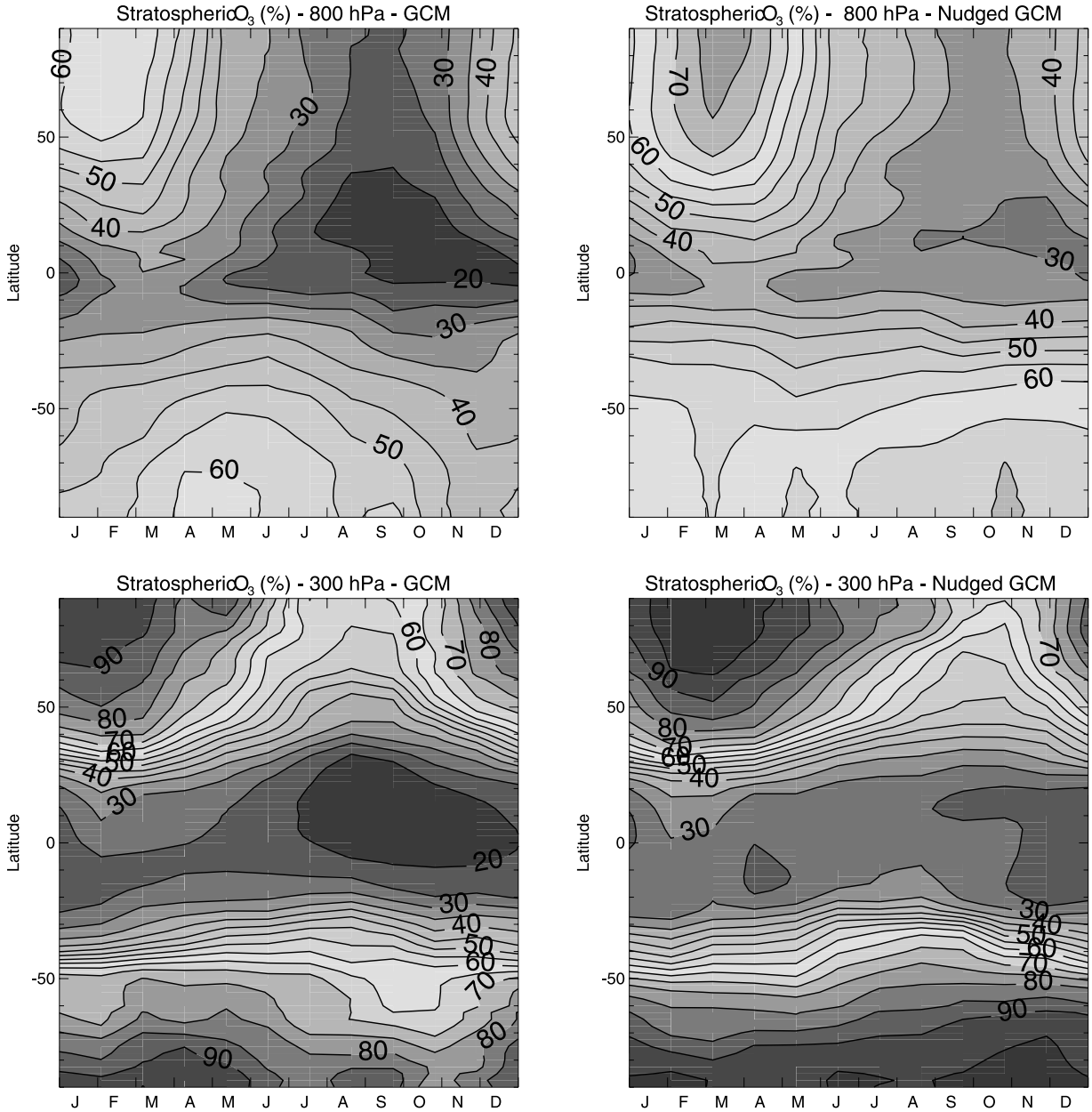


**Figure 33.** Stratospheric contribution to the zonally averaged ozone mixing ratio at 800 and 300 hPa as a function of month (%). (left) Base case GCM simulation; (right) nudged version of the GCM (year 1997). See color version of this figure at back of this issue.

ments by a factor of 2 in the model in the polluted boundary layer. In LMDz-INCA, the fact that PAN and other organic nitrates are not accounted for is a plausible reason for this disagreement. The performed sensitivity studies confirm the importance of lightning as a source of $NO_x$ contributing to 50% to the $NO_x$ levels in the tropics.

[64] The model reproduces fairly well the distribution of ozone throughout most of the troposphere. The main disagreement appears in the Northern Hemisphere upper troposphere during summer. During this period, LMDz simulates a cold upper troposphere and overestimates the height of the tropopause by 30–40 hPa. As a consequence, ozone is too low at 200 hPa during this season. This problem is partially resolved in the version of the model constrained by ECMWF reanalyzed winds. In this case, the temperature bias in the cold upper troposphere is reduced and ozone is significantly increased by comparison with the base case simulation. In this nudged version of the model, the simulated variability of ozone in the upper troposphere is also higher, reflecting more frequent stratospheric intrusions. In the base case simulation, we calculate a stratospheric influx of 523 Tg/yr in the range of recent estimates. In the nudged version of the model, a higher influx of 783 Tg/yr is obtained.

[65] In summary, LMDz-INCA provides an overall good representation of the main transport, physical, and chemical processes controlling the composition of the troposphere. More detailed versions of INCA including NMHCs, differ-

**Table 7.** Global Tropospheric Ozone Budget in LMDz-INCA[a]

| | Global | Northern Hemisphere | Southern Hemisphere |
|---|---|---|---|
| Photochemical production | 4486 [4463] | 2779 [2775] | 1706 [1688] |
| Stratospheric influx | 523 [783] | 245 [378] | 278 [405] |
| Photochemical destruction | 3918 [4164] | 2328 [2487] | 1591 [1677] |
| Dry deposition | 1090 [1082] | 695 [679] | 395 [403] |
| Net photochemistry | 567 [299] | 451 [288] | 116 [11] |
| Burden, Tg | 296 [321] | 171 [185] | 125 [136] |

[a]Values are given in Tg/yr. Values in brackets denote the budget calculated with the nudged version of the model.

ent types of aerosols and stratospheric polar chemistry are currently under development and evaluation. Results from these new versions of INCA coupled with more complex versions of the LMDz GCM providing interactions between climate, chemistry, aerosols, the continental biosphere and the ocean will be reported in forthcoming studies.

[66] **Acknowledgments.** We thank A. Bouwman, D. Brunner, F. Dentener, L. Emmons, P. Hess, C. Liousse, M. Ramonet, K. Shine, J. Sulzman, and N. Viovy for providing access to their data and software. Helpful discussions and comments on this work by Y. Balkanski, O. Boucher, L. Fairhead, G. Folberth, A. Klonecki, J. Lathière, and M. Schulz are gratefully acknowledged. This work was partly funded by the European Commission under contracts EVK2-CT-1999-00030 and EVK2-CT-1999-00021. Computer resources provided by Institut du Développement et des Ressources en Informatique Scientifique (IDRIS) under project 1167 and Commissariat á l'Energie Atomique (CEA) under project p24. The National Center for Atmospheric Research is operated by the University Corporation for Atmospheric Research under sponsorship of the National Science Foundation.

## References

Allen, D. J., and K. E. Pickering (2002), Evaluation of lightning flash rate parameterizations for use in a global chemical transport model, *J. Geophys. Res.*, *107*(D23), 4711, doi:10.1029/2002JD002066.

Andreae, M. O., and P. Merlet (2001), Emissions of trace gases and aerosols from biomass burning, *Global Biogeochem. Cycles*, *15*, 955–966.

Austin, J., N. Butchart, and J. Knight (2001), Three-dimensional chemical model simulations of the ozone layer: 2015–2055, *Q. J. R. Meteorol. Soc.*, *127*, 959–974.

Balkanski, Y. J., D. J. Jacob, G. M. Gardner, W. C. Graustein, and K. K. Turekian (1993), Transport and residence times of tropospheric aerosols inferred from a global three-dimensional simulation of $^{210}$Pb, *J. Geophys. Res.*, *98*, 20,573–20,586.

Barrie, L. A., J. W. Bottenheim, R. C. Schnell, P. J. Crutzen, and R. A. Rasmussen (1988), Ozone destruction and photochemical reactions at polar sunrise in the lower Arctic atmosphere, *Nature*, *334*, 138–140.

Bauer, S. E., Y. Balkanski, M. Schulz, D. Hauglustaine, and F. Dentener (2004), Global modeling of heterogeneous chemistry on mineral aerosol surfaces: Influence on tropospheric ozone chemistry and comparison to observations, *J. Geophys. Res.*, *109*, D02304, doi:10.1029/2003JD003868.

Berntsen, T. K., and I. S. A. Isaksen (1997), A global three-dimensional chemical transport model for the troposphere: 1. Model description and CO and ozone results, *J. Geophys. Res.*, *102*, 21,239–21,280.

Berntsen, T. J., G. Myhre, F. Stordal, and I. S. A. Isaksen (2000), Time evolution of tropospheric ozone and its radiative forcing, *J. Geophys. Res.*, *105*, 8915–8930.

Bey, I., et al. (2001), Global modeling of tropospheric chemistry with assimilated meteorology: Model description and evaluation, *J. Geophys. Res.*, *106*, 23,073–23,096.

Bird, R. B., W. E. Steward, and E. N. Lightfoot (1960), *Transport Phenomena*, John Wiley, New York.

Boucher, O., and T. L. Anderson (1995), General circulation model assessment of the sensitivity of direct climate forcing by anthropogenic sulfate aerosols to aerosol size and chemistry, *J. Geophys. Res.*, *100*, 26,117–26,134.

Boucher, O., and M. Pham (2002), History of sulfate aerosol radiative forcings, *Geophys. Res. Lett.*, *29*(9), 1308, doi:10.1029/2001GL014048.

Boucher, O., M. Pham, and C. Venkataraman (2002), Simulation of the atmospheric sulfur cycle in the Laboratoire de Météorologie Dynamique general circulation model: Model description, model evaluation, and global and European budgets, *IPSL Tech. Note 23*, Inst. Pierre Simon Laplace, Paris.

Bouwman, A. F., and J. A. Taylor (1996), Testing high-resolution nitrous oxide emission estimates against observations using an atmospheric transport model, *Global Biogeochem. Cycles*, *10*, 307–318.

Brasseur, G. P., D. A. Hauglustaine, and S. Walters (1996), Chemical compounds in the remote Pacific troposphere: Comparison between MLOPEX measurements and chemical transport model calculations, *J. Geophys. Res.*, *101*, 14,795–14,813.

Brasseur, G. P., D. A. Hauglustaine, S. Walters, P. J. Rasch, J.-F. Müller, C. Granier, and X. X. Tie (1998a), MOZART, a global chemical transport model for ozone and related chemical tracers: 1. Model description, *J. Geophys. Res.*, *103*, 28,265–28,289.

Brasseur, G. P., J. T. Kiehl, J.-F. Müller, T. Schneider, C. Granier, X. X. Tie, and D. Hauglustaine (1998b), Past and future changes in global tropospheric ozone: Impact on radiative forcing, *Geophys. Res. Lett.*, *25*, 3807–3810.

Brasseur, G. P., J. J. Orlando, and G. S. Tyndall (1999), *Atmospheric Chemistry and Global Change*, Oxford Univ. Press, New York.

Brunner, D., et al. (2003), An evaluation of the performance of chemistry transport models by comparison with research aircraft observations. Part 1: Concepts and overall model performance, *Atmos. Chem. Phys.*, *3*, 1609–1631.

Burden, R. L., and J. D. Faires (1985), *Numerical Analysis*, PWS, Boston, Mass.

Chalita, S., D. A. Hauglustaine, and J.-F. Müller (1996), Radiative forcing due to increased tropospheric ozone concentrations, *Atmos. Environ.*, *30*, 1641–1646.

Chandra, S., J. R. Ziemke, W. Min, and W. G. Read (1998), Effects of 1997–1998 El Nino on tropospheric ozone and water vapor, *Geophys. Res. Lett.*, *25*, 3867–3870.

Chang, J. S., R. A. Brost, I. S. A. Isaksen, S. Madronich, P. Middleton, W. R. Stockwell, and C. J. Walcek (1987), A three-dimensional Eulerian acid deposition model: Physical concepts and formulation, *J. Geophys. Res.*, *92*, 14,681–14,700.

Christian, H. J., et al. (2003), Global frequency and distribution of lightning as observed from space by the Optical Transient Detector, *J. Geophys. Res.*, *108*(D1), 4005, doi:10.1029/2002JD002347.

Corbett, J. J., P. S. Fischbeck, and S. N. Pandis (1999), Global nitrogen and sulfur inventories for oceangoing ships, *J. Geophys. Res.*, *104*, 3457–3470.

Dameris, M., V. Grewe, R. Hein, C. Schnadt, C. Bruhl, and B. Steil (1998), Assessment of the future development of the ozone layer, *Geophys. Res. Lett.*, *25*, 3579–3582.

Davis, D. D., et al. (2001), Impact of ship emissions on marine boundary layer $NO_x$ and $SO_2$ distributions over the Pacific basin, *Geophys. Res. Lett.*, *28*, 235–238.

De Fries, R. S., and J. R. Townshend (1994), NDVI-derived land classification at global scales, *Int. J. Remote Sens.*, *15*, 3567–3586.

DeMore, W. B., S. P. Sander, D. M. Golden, R. F. Hampson, M. J. Kurylo, C. J. Howard, A. R. Ravishankara, C. E. Kolb, and M. J. Molina (1997), Chemical kinetics and photochemical data for use in stratospheric modeling, *JPL Publ., 97-4*.

Denning, A. S., et al. (1999), Three-dimensional transport and concentration of $SF_6$ A model intercomparison study (TransCom 2), *Tellus, Ser. B*, *51*, 266–297.

Dentener, F. J., and P. J. Crutzen (1993), Reaction of $N_2O_5$ on tropospheric aerosols: Impact on the global distributions of $NO_x$, $O_3$, and OH, *J. Geophys. Res.*, *98*, 7149–7163.

Dentener, F., J. Feichter, and A. Jeuken (1999), Simulation of the transport of Rn222 using on-line and off-line global models at different horizontal resolutions: A detailed comparison with measurements, *Tellus, Ser. B*, *51*, 573–602.

Dibb, J. E., R. W. Talbot, K. I. Klemm, G. L. Gregory, H. B. Singh, J. D. Bradshaw, and S. T. Sandholm (1996), Asian influence over the western North Pacific during the fall season: Inferences from lead 210, soluble ionic species and ozone, *J. Geophys. Res.*, *101*, 1779–1792.

Dibb, J. E., R. W. Talbot, B. L. Lefer, E. Scheuer, G. L. Gregory, E. V. Browell, J. D. Bradshaw, S. T. Sandholm, and H. B. Singh (1997), Distributions of $^7$Be, $^{210}$Pb, and soluble aerosol-associated ionic species over the western Pacific: PEM West B, February–March 1994, *J. Geophys. Res.*, *102*, 28,287–28,302.

Dlugokencky, E. J., K. A. Masarie, P. M. Lang, and P. P. Tans (1998), Continuing decline in the growth rate of the atmospheric methane burden, *Nature*, *393*, 447–450.

Dufresne, J.-L., P. Friedlingstein, M. Berthelot, L. Bopp, P. Ciais, L. Fairhead, H. Le Treut, and P. Monfray (2002), On the magnitude of positive feedback between future climate change and the carbon cycle, *Geophys. Res. Lett.*, *29*(10), 1405, doi:10.1029/2001GL013777.

Emmons, L. K., et al. (1997), Climatologies of $NO_x$ and $NO_y$: A comparison of data and models, *Atmos. Environ.*, *31*, 1851–1904.

Emmons, L. K., D. A. Hauglustaine, J. F. Müller, M. A. Carroll, G. P. Brasseur, D. Brunner, J. Stahelin, V. Thouret, and A. Marenco (2000), Data composites of airborne observations of tropospheric ozone and its precursors, *J. Geophys. Res.*, *105*, 20,497–20,538.

Erickson, D. J., III, and J. A. Taylor (1992), 3-D tropospheric CO modeling: The possible influence of the ocean, *Geophys. Res. Lett.*, *19*, 1955–1958.

Erisman, J. W., C. Beier, G. Graaijers, and S. Lindberg (1994), Review of deposition monitoring methods, *Tellus, Ser. B*, *46*, 79–93.

Feichter, J., and P. J. Crutzen (1990), Parameterization of vertical tracer transport due to deep cumulus convection in a global transport model and its evaluation with $^{222}$Radon measurements, *Tellus, Ser. B*, *42*, 100–117.

Feichter, J., E. Kjellstrom, H. Rodhe, F. Dentener, J. Lelieveld, and G.-J. Roelofs (1996), Simulation of the tropospheric sulfur cycle in a global climate model, *Atmos. Environ.*, *30*, 1693–1707.

Fouquart, Y., and B. Bonnel (1980), Computations of solar heating of the Earth's atmosphere: A new parameterization, *Contrib. Atmos. Phys.*, *53*, 35–62.

Friedlingstein, P., L. Bopp, P. Ciais, J.-L. Dufresne, L. Fairhead, H. Le Treut, P. Monfray, and J. Orr (2001), Positive feedback between future climate change and the carbon cycle, *Geophys. Res. Lett.*, *28*, 1543–1546.

Fuglestvedt, J. S., T. K. Berntsen, I. S. A. Isaksen, H. Mao, X.-Z. Liang, and W.-C. Wang (1999), Climatic forcing of nitrogen oxides through changes in tropospheric ozone and methane: Global 3D model studies, *Atmos. Environ.*, *33*, 961–977.

Fung, I., J. John, J. Lerner, E. Matthews, M. J. Prather, L. P. Steele, and P. J. Fraser (1991), Global budgets of atmospheric methane: Results from a three-dimensional global model synthesis, *J. Geophys. Res.*, *96*, 13,033–13,065.

Galloway, J. N., H. Levy II, and P. S. Kasibhatla (1994), Year 2020: Consequences of population growth and development on deposition of oxidized nitrogen, *Ambio*, *23*, 120–123.

Ganzeveld, L., and J. Lelieveld (1995), Dry deposition parameterization in a chemistry general circulation model and its influence on the distribution of reactive trace gases, *J. Geophys. Res.*, *100*, 20,999–21,012.

Gardner, R. M., et al. (1998), ANCAT/EC2 global aircraft emission inventories for 1991/92 and 2015: Report by the ECAC/ANCAT and EC Working Group, Def. Eval. and Res. Agency, Farnborough, UK.

Genthon, C., and A. Armengaud (1995), Radon 222 as a comparative tracer of transport and mixing in two general circulation models of the atmosphere, *J. Geophys. Res.*, *100*, 2849–2866.

Gettelman, A., J. R. Holton, and K. H. Rosenlof (1997), Mass fluxes of $O_3$, $CH_4$, $N_2O$, and $CF_2Cl_2$ in the lower stratosphere calculated from observational data, *J. Geophys. Res.*, *102*, 19,149–19,159.

Giorgi, F., and W. L. Chameides (1985), The rainout parameterization in a photochemical model, *J. Geophys. Res.*, *90*, 7872–7880.

Guelle, W., Y. J. Balkanski, M. Schulz, F. Dulac, and P. Monfray (1998a), Wet deposition in a global size-dependent aerosol transport model: 1. Comparison of a 1 year $^{210}$Pb simulation with ground measurements, *J. Geophys. Res.*, *103*, 11,429–11,445.

Guelle, W., Y. J. Balkanski, J. E. Dibb, M. Schulz, and F. Dulac (1998b), Wet deposition in a global size-dependent aerosol transport model: 2. Influence of the scavenging scheme on $^{210}$Pb vertical profiles, surface concentrations, and deposition, *J. Geophys. Res.*, *103*, 28,875–28,891.

Guenther, A., C. N. Hewitt, T. Pierce, B. Lamb, P. Harley, and R. Fall (1995), A global model of natural volatile organic compound emissions, *J. Geophys. Res.*, *100*, 8873–8892.

Gurney, K., R. Law, P. Rayner, and A. S. Denning (2000), TransCom 3 experimental protocol, *Pap. 707*, Dep. of Atmos. Sci., Colo. State Univ., Boulder.

Hall, B. D., et al. (2001), Halocarbons and other atmospheric trace species, in *Climate Monitoring and Diagnostics Laboratory Summary Report 25, 1998–1999*, edited by R. C. Schnell, D. B. King, and R. M. Rosson, pp. 91–131, NOAA Off. of Oceanic and Atmos. Res., Boulder, Colo.

Hallquist, M., D. J. Stewart, J. Baker, and R. A. Cox (2000), Hydrolysis of $N_2O_5$ on submicron sulfuric acid aerosols, *J. Phys. Chem. A*, *104*, 3984–3990.

Hänel, G. (1976), The properties of atmospheric aerosol particles as functions of the relative humidity at thermodynamic equilibrium with the surrounding moist air, *Adv. Geophys.*, *19*, 73–188.

Hansen, J., et al. (2002), Climate forcings in Goddard Institute for Space Studies SI2000 simulations, *J. Geophys. Res.*, *107*(D8), 4347, doi:10.1029/2001JD001143.

Hao, W. M., and M.-H. Liu (1994), Spatial distribution of tropical biomass burning in 1980 with 5° × 5° resolution, *Global Biogeochem. Cycles*, *8*, 495–503.

Hartley, D. E., D. L. Williamson, P. J. Rasch, and R. G. Prinn (1994), Examination of tracer transport in the NCAR CCM2 by comparison of CFCL3 simulations with ALE/GAGE observations, *J. Geophys. Res.*, *99*, 12,885–12,896.

Harzallah, A., and R. Sadourny (1995), Internal versus SST-forced atmospheric variability as simulated by atmospheric general circulation model, *J. Clim.*, *8*, 474–495.

Hauglustaine, D. A., and G. P. Brasseur (2001), Evolution of tropospheric ozone under anthropogenic activities and associated radiative forcing of climate, *J. Geophys. Res.*, *106*, 32,337–32,360.

Hauglustaine, D. A., and D. H. Ehhalt (2002), A three-dimensional model of molecular hydrogen in the troposphere, *J. Geophys. Res.*, *107*(D17), 4330, doi:10.1029/2001JD001156.

Hauglustaine, D. A., C. Granier, G. P. Brasseur, and G. Mégie (1994), The importance of atmospheric chemistry in the calculation of radiative forcing on the climate system, *J. Geophys. Res.*, *99*, 1173–1186.

Hauglustaine, D. A., G. P. Brasseur, S. Walters, P. J. Rasch, J.-F. Müller, L. K. Emmons, and M. A. Carroll (1998), MOZART, a global chemical transport model for ozone and related chemical tracers: 2. Model results and evaluation, *J. Geophys. Res.*, *103*, 28,291–28,335.

Hein, R., P. J. Crutzen, and M. Heimann (1997), An inverse modeling approach to investigate the global atmospheric methane cycle, *Global. Biogeochem. Cycles*, *11*, 43–76.

Hein, R., et al. (2001), Results of an interactive coupled atmospheric chemistry-general circulation model: Comparison with observations, *Ann. Geophys.*, *19*, 435–457.

Hess, P. G., S. Flocke, J.-F. Lamarque, M. C. Barth, and S. Madronich (2000), Episodic modeling of the chemical structure of the troposphere as revealed during the spring MLOPEX 2 intensive, *J. Geophys. Res.*, *105*, 26,809–26,839.

Hesstvedt, E., Ö. Høv, and I. S. A. Isaksen (1978), Quasi-steady-state approximations in air pollution modeling: Comparison of two numerical schemes for oxidant prediction, *Int. J. Chem. Kinet.*, *10*, 971–994.

Highwood, E. J., K. P. Shine, M. D. Hurley, and T. J. Wallington (1999), Estimation of direct radiative forcing due to non-methane hydrocarbons, *Atmos. Environ.*, *33*, 759–767.

Hoinka, K. (1998), Statistics of the global tropopause pressure, *Mon. Weather Rev.*, *126*, 3303–3325.

Holland, E. A., et al. (1997), Variations in the predicted spatial distribution of atmospheric nitrogen deposition and their impact on carbon uptake by terrestrial ecosystems, *J. Geophys. Res.*, *102*, 15,849–15,866.

Holland, E. A., F. J. Dentener, B. H. Braswell, and J. Sulzman (1999), Contemporary and pre-industrial global reactive nitrogen budgets, *Biogeochemistry*, *46*, 7–43.

Horowitz, L. W., et al. (2003), A global simulation of tropospheric ozone and related tracers: Description and evaluation of MOZART, version 2, *J. Geophys. Res.*, *108*(D24), 4784, doi:10.1029/2002JD002853.

Hourdin, F., and A. Armengaud (1999), The use of finite-volume methods for atmospheric advection of trace species: 1. Test of various formulations in a general circulation model, *Mon. Weather Rev.*, *127*, 822–837.

Hourdin, F., and J. P. Issartel (2000), Sub-surface nuclear tests monotoring through the CTBT xenon network, *Geophys. Res. Lett.*, *27*, 2245–2248.

Hourdin, F., P. Le Van, F. Forget, and O. Talagrand (1993), Meteorological variability and the annual surface pressure cycle on Mars, *J. Atmos. Sci.*, *50*, 3625–3640.

Houweling, S., F. Dentener, J. Lelieveld, B. Walter, and E. Dlugokencky (2000), The modeling of tropospheric methane: How well can point measurements be reproduced by a global model?, *J. Geophys. Res.*, *105*, 8981–9002.

Jacob, D. (2000), Heterogeneous chemistry and tropospheric ozone, *Atmos. Environ.*, *34*, 2131–2159.

Jacob, D. J., and M. J. Prather (1990), Radon-222 as a test of convective transport in a general circulation model, *Tellus, Ser. B*, *42*, 118–134.

Jacob, D. J., M. J. Prather, S. C. Wofsy, and M. B. McElroy (1987), Atmospheric distribution of $^{85}$Kr simulated with a general circulation model, *J. Geophys. Res.*, *92*, 6614–6626.

Jacob, D. J., et al. (1993), Simulation of summertime ozone over North America, *J. Geophys. Res.*, *98*, 14,797–14,816.

Jacob, D. J., et al. (1997), Evaluation and intercomparison of global atmospheric transport models using 222Rn and other short-lived tracers, *J. Geophys. Res.*, *102*, 5953–5970.

Johnson, C. E., D. S. Stevenson, W. J. Collins, and R. G. Derwent (2001), Role of climate feedback on methane and ozone studied with a coupled ocean-atmosphere-chemistry model, *Geophys. Res. Lett.*, *28*, 1723–1726.

Jourdain, L., and D. A. Hauglustaine (2001), The global distribution of lightning $NO_x$ simulated on-line in a general circulation model, *Phys. Chem. Earth, Part B: Hydrol. Oceans Atmos.*, *26*, 585–591.

Kasibhatla, P., et al. (2000), Do emissions from ships have a significant impact on concentrations of nitrogen oxides in the marine boundary layer?, *Geophys. Res. Lett.*, *27*, 2229–2232.

Kjellström, E., J. Feichter, and G. Hoffman (2000), Transport of $SF_6$ and $^{14}CO_2$ in the atmospheric general circulation model ECHAM4, *Tellus, Ser. B*, *52*, 1–18.

Koch, D. M., D. J. Jacob, and W. C. Graustein (1996), Vertical transport of tropospheric aerosols as indicated by $^{7}Be$ and $^{210}Pb$ in a chemical tracer model, *J. Geophys. Res.*, *101*, 18,651–18,666.

Koch, D., D. Jacob, I. Tegen, D. Rind, and M. Chin (1999), Tropospheric sulfur simulation and sulfate direct radiative forcing in the Goddard Institute for Space Studies general circulation model, *J. Geophys. Res.*, *104*, 23,799–23,822.

Kraus, A. B., F. Rohrer, E. S. Grobler, and D. H. Ehhalt (1996), The global tropospheric distribution of $NO_x$ estimated by a three-dimensional chemical tracer model, *J. Geophys. Res.*, *101*, 18,587–18,604.

Kritz, M. A., S. W. Rosner, and D. Z. Stockwell (1998), Validation of an off-line three dimensional chemical transport model using observed radon profiles: 1. Observations, *J. Geophys. Res.*, *103*, 8425–8432.

Kroeze, C., A. Mosier, and L. Bouwman (1999), Closing the global $N_2O$ budget: A retrospective analysis 1500–1994, *Global Biogeochem. Cycles*, *13*, 1–8.

Lacis, A. A., D. J. Wuebbles, and J. A. Logan (1990), Radiative forcing of climate by changes in the vertical distribution of ozone, *J. Geophys. Res.*, *95*, 9971–9981.

Lamarque, J.-F., G. P. Brasseur, P. G. Hess, and J.-F. Müller (1996), Three-dimensional study of the relative contributions of the different nitrogen sources in the troposphere, *J. Geophys. Res.*, *101*, 22,955–22,968.

Lamb, D., and J. Van Bowersox (2000), The National Atmospheric Deposition Program: An overview, *Atmos. Environ.*, *34*, 1661–1663.

Law, K. S., et al. (1998), Evaluation of modeled $O_3$ using Measurements of Ozone by Airbus In-Service Aircraft (MOZAIC) data, *J. Geophys. Res.*, *103*, 25,721–25,737.

Law, K. S., et al. (2000), Comparison between global chemistry transport model results and Measurement of Ozone and Water Vapor by Airbus In-Service Aircraft (MOZAIC) data, *J. Geophys. Res.*, *105*, 1503–1526.

Lawrence, M. G., and P. J. Crutzen (1998), The impact of cloud particle gravitational settling on soluble trace gas distributions, *Tellus, Ser. B*, *50*, 263–289.

Lawrence, M. G., P. J. Crutzen, P. J. Rasch, B. E. Eaton, and N. M. Mahowald (1999), A model for studies of tropospheric photochemistry: Description, global distributions, and evaluation, *J. Geophys. Res.*, *104*, 26,245–26,277.

Lawrence, M. G., P. Jockel, and R. von Kuhlmann (2001), What does the global mean OH concentration tell us?, *Atmos. Chem. Phys.*, *1*, 37–49.

Lee, D. S., I. Köhler, E. Grobler, F. Rohrer, R. Sausen, L. Gallardo-Klenner, J. G. J. Olivier, F. J. Dentener, and A. F. Bouwman (1997), Estimations of global $NO_x$ emissions and their uncertainties, *Atmos. Environ.*, *31*, 1735–1749.

Lee, H. N., and J. Feichter (1995), An intercomparison of wet precipitation scavenging schemes and the emission rates of $^{222}Rn$ for the simulation of global transport and deposition of $^{210}Pb$, *J. Geophys. Res.*, *100*, 23,253–23,270.

Lelieveld, J., and F. J. Dentener (2000), What controls tropospheric ozone?, *J. Geophys. Res.*, *105*, 3531–3551.

Le Treut, H., and Z. X. Li (1991), Sensitivity of an atmospheric general circulation model to prescribed SST changes: Feedback effects associated with the simulation of cloud optical properties, *Clim. Dyn.*, *5*, 175–187.

Le Treut, H., Z. X. Li, and M. Forichon (1994), Sensitivity of the LMD general circulation model to greenhouse forcing associated with two different cloud water parametrizations, *J. Clim.*, *7*, 1827–1841.

Le Treut, H., M. Forichon, O. Boucher, and Z.-X. Li (1998), Sulfate aerosol indirect effect and $CO_2$ greenhouse forcing: Equilibrium response of the LMD GCM and associated cloud feedbacks, *J. Clim.*, *11*, 1673–1684.

Levin, I., and V. Hesshaimer (1996), Refining of atmospheric transport model entries by the globally observed passive tracer distributions of $^{85}Kr$ and sulfur hexafluoride ($SF_6$), *J. Geophys. Res.*, *101*, 16,745–16,755.

Li, D., and K. P. Shine (1995), A 4-D ozone climatology for UGAMP models, UGAMP internal report, U. K. Univ. Global Atmos. Model. Programme, Swindon.

Li, Q., et al. (2002), Transatlantic transport of pollution and its effects on surface ozone in Europe and North America, *J. Geophys. Res.*, *107*(D13), 4166, doi:10.129/2001JD001422.

Liu, H., D. J. Jacob, I. Bey, and R. M. Yantosca (2001), Contraints from $^{210}Pb$ and $^{7}Be$ on wet deposition and transport in a global three-dimensional chemical transport model driven by assimilated meteorological fields, *J. Geophys. Res.*, *106*, 12,109–12,128.

Liu, S. C., J. R. McAfee, and R. J. Cicerone (1984), $^{222}Radon$ and tropospheric vertical transport, *J. Geophys. Res.*, *89*, 7291–7297.

Logan, J. (1999), An analysis of ozonesonde data for the troposphere: Recommendations for testing 3D-models and development of a gridded climatology for tropospheric ozone, *J. Geophys. Res.*, *104*, 16,115–16,149.

Madronich, S., and S. Flocke (1997), Theoretical estimation of biologically effective UV radiation at the Earth's surface, in *Solar Ultraviolet Radiation: Modeling, Measurements and Effects*, *NATO ASI Ser., Ser. I*, vol. 52, edited by C. S. Zerefos, and A. F. Bais, pp. 23–48, Springer-Verlag, New York.

Mahowald, N. M., R. G. Prinn, and P. J. Rasch (1997a), Deducing $CCl_3F$ emissions using an inverse method and chemical transport models with assimilated winds, *J. Geophys. Res.*, *102*, 28,153–28,168.

Mahowald, N. M., P. J. Rasch, B. E. Eaton, S. Whittlestone, and R. G. Prinn (1997b), Transport of $^{222}Radon$ to the remote troposphere using MATCH and assimilated winds from ECMWF and NCEP/NCAR, *J. Geophys. Res.*, *102*, 28,139–28,152.

Maiss, M., L. P. Steele, R. J. Francey, P. J. Fraser, R. L. Langenfels, N. B. A. Trivett, and I. Levin (1996), Sulfur hexafluoride: A new atmospheric tracer, *Atmos. Environ.*, *30*, 1621–1629.

Mari, C., D. J. Jacob, and P. Bechtold (2000), Transport and scavenging of soluble gases in a deep convective cloud, *J. Geophys. Res.*, *105*, 22,255–22,268.

McLinden, C. A., S. C. Olsen, B. Hannegan, O. Wild, M. J. Prather, and J. Sundet (2000), Stratospheric ozone in 3-D models: A simple chemistry and the cross-tropopause flux, *J. Geophys. Res.*, *105*, 14,653–14,665.

Mickley, L. J., P. P. Murti, D. J. Jacob, J. A. Logan, D. M. Koch, and D. Rind (1999), Radiative forcing from tropospheric ozone calculated with a unified chemistry-climate model, *J. Geophys. Res.*, *104*, 30,153–30,172.

Montzka, S. A., et al. (2003), Controlled substances and other source gases, in *Scientific Assessment of Ozone Depletion: 2002, Rep. 47*, chap. 1, pp. 1.1–1.71, World Meteorol. Organ., Geneva.

Moore, H. E., S. E. Poet, and E. A. Martell (1973), $^{222}Rn$, $^{210}Pb$, $^{210}Bi$, and $^{210}Po$ profiles and aerosol residence times versus altitude, *J. Geophys. Res.*, *78*, 7065–7075.

Morcrette, J.-J. (1991), Radiation and cloud radiative properties in the European Centre for Medium Range Weather Forecasts forecasting system, *J. Geophys. Res.*, *96*, 9121–9132.

Moxim, W. J., H. Levy II, and P. S. Kasibhatla (1996), Simulated global tropospheric PAN: Its transport and impact on $NO_x$, *J. Geophys. Res.*, *101*, 12,621–12,638.

Müller, J.-F. (1992), Geographical distribution and seasonal variation of surface emissions and deposition velocities of atmospheric trace gases, *J. Geophys. Res.*, *97*, 3787–3804.

Müller, J.-F., and G. Brasseur (1995), IMAGES: A three-dimensional chemical transport model of the global troposphere, *J. Geophys. Res.*, *100*, 16,445–16,490.

Murphy, D. M., D. W. Fahey, M. H. Proffitt, S. C. Liu, K. R. Chan, C. S. Eubank, S. R. Kawa, and K. K. Kelly (1993), Reactive nitrogen and its correlation with ozone in the lower stratosphere and upper troposphere, *J. Geophys. Res.*, *98*, 8751–8773.

Nagashima, T., M. Takahashi, M. Takigawa, and H. Akiyoshi (2002), Future development of the ozone layer calculated by a general circulation model with fully interactive chemistry, *Geophys. Res. Lett.*, *29*(8), 1162, doi:10.1029/2001GL014026.

Nesmes-Ribes, E., E. N. Ferreira, R. Sadourny, H. Le Treut, and Z.-X. Li (1993), Solar dynamics and its impact on solar irradiance and the terrestrial climate, *J. Geophys. Res.*, *98*, 18,923–18,935.

Nevison, C. D., and R. F. Weiss (1995), Global oceanic emissions of nitrous oxide, *J. Geophys. Res.*, *100*, 15,809–15,820.

Novelli, P. C., J. E. Collins Jr., R. C. Myers, G. W. Sachsem, and H. E. Scheel (1994), Reevaluation of the NOAA/CMDL carbon monoxide reference scale and comparisons to CO reference gases at NASA-Langley and the Fraunhofer Institute, *J. Geophys. Res.*, *99*, 12,833–12,839.

Novelli, P. C., P. M. Lang, K. A. Masarie, D. F. Hurst, R. Myers, and J. W. Elkins (1999), Molecular hydrogen in the troposphere: Global distribution and budget, *J. Geophys. Res.*, *104*, 30,427–30,444.

Olivier, J. G. J., and J. J. M. Berdowski (2001), Global emission sources and sinks, in *The Climate System*, edited by J. Berdowski, R. Guicherit, and B. Heij, pp. 33–77, Swets and Zeitlinger B. V., Lisse, Netherlands.

Oltmans, S. J., and H. Levy II (1994), Surface ozone measurements from a global network, *Atmos. Environ.*, *28*, 9–24.

Penner, J. E., C. S. Atherton, J. Dignon, S. J. Ghan, J. J. Walton, and S. Hameed (1991), Tropospheric nitrogen: A three-dimensional study of sources, distributions, and deposition, *J. Geophys. Res.*, *96*, 959–990.

Pickering, K. E., Y. Wang, W. K. Tao, C. Price, and J.-F. Müller (1998), Vertical distributions of lightning $NO_x$ for use in regional and global chemical transport models, *J. Geophys. Res.*, *103*, 31,203–31,216.

Prather, M. J., M. B. McElroy, S. C. Wofsy, G. Russel, and D. Rind (1987), Chemistry of the global troposphere: Fluorocarbons as tracers of air motion, *J. Geophys. Res.*, *92*, 6579–6613.

Prather, M., et al. (2001), Atmospheric chemistry and greenhouse gases, in *Climatic Change 2001: The Scientific Basis*, edited by J. T. Houghton et al., chap. 4, pp. 241–290, Cambridge Univ. Press, New York.

Price, C., and D. Rind (1992), A simple lightning parameterization for calculating global lightning distributions, *J. Geophys. Res.*, *97*, 9919–9933.

Price, C., J. Penner, and M. Prather (1997), $NO_x$ from lightning: 1. Global distribution based on lightning physics, *J. Geophys. Res.*, *102*, 5929–5941.

Prinn, R. G., et al. (2000), A history of chemically and radiatively important gases in air deduced from ALE/GAGE/AGAGE, *J. Geophys. Res.*, *105*, 17,751–17,792.

Prinn, R. G., et al. (2001), Evidence for substantial variations of atmospheric hydroxyl radicals in the past two decades, *Science*, *292*, 1882–1888.

Ramaswamy, V., et al. (2001), Radiative forcing of climate change, in *Climatic Change 2001: The Scientific Basis*, edited by J. T. Houghton, et al., chap. 6, pp. 351–418, Cambridge Univ. Press, New York.

Randel, W. J., F. Wu, and D. Gaffen (2000), Interannual variability of the tropical tropopause derived from radiosonde data and NCEP reanalyses, *J. Geophys. Res.*, *105*, 15,509–15,523.

Rasch, P. J., B. A. Boville, and G. P. Brasseur (1995), A three-dimensional general circulation model with coupled chemistry for the middle atmosphere, *J. Geophys. Res.*, *100*, 9041–9071.

Rasch, P. J., M. C. Barth, J. T. Kiehl, S. E. Schwartz, and C. Benkovitz (2000), A description of the global sulfur cycle and its controlling processes in the National Center for Atmospheric Research Community Climate Model, version 3, *J. Geophys. Res.*, *105*, 1367–1385.

Rayner, N. A., E. B. Horton, D. E. Parker, C. K. Folland, and R. B. Hackett (1996), Version 2.2 of the global sea-ice and sea-surface temperature data set, 1903–1994, *CRTN 74*, Hadley Cent., Meteorol. Off., Bracknell, UK.

Rayner, P. J., and R. M. Law (1995), A comparison of modelled responses to prescribed $CO_2$ sources, *CSIRO Aust. Div. Atmos. Res. Tech. Pap. 36*, 1–82, Commonw. Sci. and Ind. Res. Organ., Melbourne, Victoria, Australia.

Rehfeld, S., and M. Heimann (1995), Three dimensional atmospheric transport simulation of the radioactive tracers $^{210}$Pb, $^{7}$Be, $^{10}$Be, and $^{90}$Sr, *J. Geophys. Res.*, *100*, 26,141–26,161.

Rind, D., and J. Lerner (1996), Use of on-line tracers as a diagnostic tool in general circulation model development: 1. Horizontal and vertical transport in the troposphere, *J. Geophys. Res.*, *101*, 12,667–12,683.

Rodhe, H., F. Dentener, and M. Schulz (2002), The global distribution of acidifying wet deposition, *Environ. Sci. Technol.*, *36*, 4382–4388.

Roelofs, G.-J., and J. Lelieveld (1995), Distribution and budget of $O_3$ in the troposphere calculated with a chemistry general circulation model, *J. Geophys. Res.*, *100*, 20,983–20,998.

Roelofs, G.-J., and J. Lelieveld (1997), Model study of the influence of cross-tropopause $O_3$ transports on tropospheric $O_3$ levels, *Tellus, Ser. B*, *49*, 38–55.

Roelofs, G. J., J. Lelieveld, and L. Ganzeveld (1998), Simulation of global sulfate distribution and the influence on effective cloud drop radii with a coupled photochemistry-sulfur cycle model, *Tellus, Ser. B*, *50*, 224–242.

Sadourny, R., and K. Laval (1984), January and July performance of the LMD general circulation model, in *New Perspectives in Climate Modelling*, edited by A. Berger and C. Nicolis, pp. 173–198, Elsevier Sci., New York.

Sander, S. P., et al. (2000), Chemical kinetics and photochemical data for use in stratospheric modeling, supplement to evaluation 12: Update of key reactions, *JPL Publ., 00-3*.

Sander, S. P., et al. (2002), Chemical kinetics and photochemical data for use in stratospheric modeling: Evaluation 14, *JPL Publ., 02-25*.

Sanderson, M. G., W. J. Collins, R. G. Derwent, and C. E. Johnson (2003), Simulation of global hydrogen levels using a Lagrangian three-dimensional model, *J. Atmos. Chem.*, *46*, 15–28.

Sandu, A., J. G. Verwer, J. G. Blom, E. J. Spee, and G. R. Carmichael (1996), Benchmarking stiff ODE solvers for atmospheric chemistry problems. II: Rosenbrock solvers, *Rep. Comput. Math. 90/1996*, Univ. of Iowa, Ames.

Seinfeld, J. H., and S. N. Pandis (1998), *Atmospheric Chemistry and Physics*, John Wiley, New York.

Shimazaki, T. (1985), *Minor Constituents in the Middle Atmosphere*, Terra Sci., Tokyo.

Shindell, D. T., D. Rind, and P. Lonergan (1998), Increased polar stratospheric ozone losses and delayed eventual recovery owing to increasing greenhouse-gas concentrations, *Nature*, *392*, 589–592.

Shindell, D. T., J. L. Grenfell, D. Rind, V. Grewe, and C. Price (2001), Chemistry-climate interactions in the Goddard Institute for Space Studies general circulation model: 1. Tropospheric chemistry model description and evaluation, *J. Geophys. Res.*, *106*, 8047–8075.

Sinha, A., and R. Toumi (1996), A comparison of climate forcings due to chlorofluorocarbons and carbon monoxide, *Geophys. Res. Lett.*, *23*, 65–68.

Solomon, S., R. W. Portmann, R. W. Sanders, J. S. Daniel, W. Madsen, B. Bartman, and E. G. Dutton (1999), On the role of nitrogen dioxide in the absorption of solar radiation, *J. Geophys. Res.*, *104*, 12,047–12,058.

Spivakovsky, C. M., et al. (2000), Three-dimensional climatological distribution of tropospheric OH: Update and evaluation, *J. Geophys. Res.*, *105*, 8931–8980.

Steil, B., M. Dameris, C. Bruhl, P. J. Crutzen, V. Grewe, M. Ponater, and R. Sausen (1998), Development of a chemistry module for GCMs: First results of a multiannual integration, *Ann. Geophys.*, *16*, 205–228.

Stevenson, D. S., W. J. Collins, C. E. Johnson, and R. G. Derwent (1998), Intercomparison and evaluation of atmospheric transport in a Lagrangian model (STOCHEM), and an Eulerian model (UM), using $^{222}$Rn as a short-lived tracer, *Q. J. R. Meteorol. Soc.*, *124*, 2477–2491.

Stevenson, D. S., C. E. Johnson, W. J. Collins, R. G. Derwent, and J. M. Edwards (2000), Future estimates of tropospheric ozone radiative forcing and methane turnover: The impact of climate change, *Geophys. Res. Lett.*, *27*, 2073–2076.

Taguchi, S., T. Iida, and J. Moriizumi (2002), Evaluation of the atmospheric transport model NIRE-CTM-96 by using measured radon-222 concentrations, *Tellus, Ser. B*, *54*, 2050–2068.

Tett, S. F. B., et al. (2002), Estimation of natural and anthropogenic contributions to twentieth century temperature change, *J. Geophys. Res.*, *107*(D16), 4306, doi:10.1029/2000JD000028.

Tiedtke, M. (1989), A comprehensive mass flux scheme for cumulus parameterization in large-scale models, *Mon. Weather Rev.*, *117*, 1779–1800.

Van Leer, B. (1977), Towards the ultimate conservative difference scheme. Part IV: A new approach to numerical convection, *J. Comput. Phys.*, *23*, 276–299.

van Leeuwen, E. P., G. P. J. Draaijers, and J. W. Erisman (1996), Mapping wet deposition of acidifying components and base cations over Europe using measurements, *Atmos. Environ.*, *30*, 2495–2511.

von Glasow, R., M. G. Lawrence, R. Sander, and P. J. Crutzen (2002), Modeling the chemical effects of ship exhaust in the cloud-free marine boundary layer, *Atmos. Chem. Phys. Discuss.*, *2*, 525–575.

von Kuhlmann, R., M. G. Lawrence, U. Pöschl, and P. J. Crutzen (2003), Sensitivities in global scale modeling of isoprene, *Atmos. Chem. Phys. Discuss.*, *3*, 3095–3134.

Walcek, C. J., R. A. Brost, J. S. Chang, and M. L. Wesely (1986), $SO_2$, sulfate and $HNO_3$ deposition velocities computed using regional landuse and meteorological data, *Atmos. Environ.*, *20*, 949–964.

Wang, K.-Y., and D. E. Shallcross (2000), Modelling terrestrial biogenic isoprene fluxes and their potential impact on global chemical species using a coupled LSM-CTM model, *Atmos. Environ.*, *34*, 2909–2925.

Wang, Y., and D. J. Jacob (1998), Anthropogenic forcing on tropospheric ozone and OH since preindustrial times, *J. Geophys. Res.*, *103*, 31,123–31,135.

Wang, Y., J. A. Logan, D. J. Jacob, and C. M. Spivakovsky (1998), Global simulation of tropospheric $O_3$-$NO_x$-hydrocarbon chemistry: 2. Model evaluation and global ozone budget, *J. Geophys. Res.*, *103*, 10,727–10,755.

Waugh, D. W., et al. (1997), Three-dimensional simulations of long-lived tracers using winds from MACCM2, *J. Geophys. Res.*, *102*, 21,493–21,513.

Weiss, W., A. Sittkus, H. Stockburger, and H. Sartorius (1983), Large-scale atmospheric mixing derived from meridional profiles of krypton 85, *J. Geophys. Res.*, *88*, 8574–8578.

Wesely, M. L. (1989), Parametrization of surface resistances to gaseous dry deposition in regional-scale numerical models, *Atmos. Environ.*, *23*, 1293–1304.

World Meteorological Organization (WMO) (1992), *International Meteorological Vocabulary*, *WMO Publ. 182*, 2nd ed., Geneva.

Yienger, J. J., and H. Levy II (1995), Empirical model of global soil-biogenic NOx emissions, *J. Geophys. Res.*, *100*, 11,447–11,464.

Zeng, G., and J. A. Pyle (2003), Changes in tropospheric ozone between 2000 and 2100 modeled in a chemistry-climate model, *Geophys. Res. Lett.*, *30*(7), 1392, doi:10.1029/2002GL016708.

M.-A. Filiberti, Institut Pierre Simon Laplace, Université de Paris 6, boîte 101, F-75252 Paris Cedex 05, France. (filiberti@ipsl.jussieu.fr)

D. A. Hauglustaine, Laboratoire des Sciences du Climat et de l'Environnement, Bât. 709, Orme des Merisiers, F-91191 Gif-sur-Yvette Cedex, France. (hauglustaine@cea.fr)

E. A. Holland, J.-F. Lamarque, and S. Walters, National Center for Atmospheric Research, P. O. Box 3000, Boulder, CO 80307, USA. (eholland@acd.ucar.edu; lamar@acd.ucar.edu; stacy@acd.ucar.edu)

F. Hourdin, Laboratoire de Météorologie Dynamique, Université de Paris 6, boîte 99, F-75252, Paris Cedex 05, France. (hourdin@lmd.jussieu.fr)

L. Jourdain, Service d'Aéronomie, Université de Paris 6, boîte 102, F-75252 Paris Cedex 05, France. (jourdain@aero.jussieu.fr)

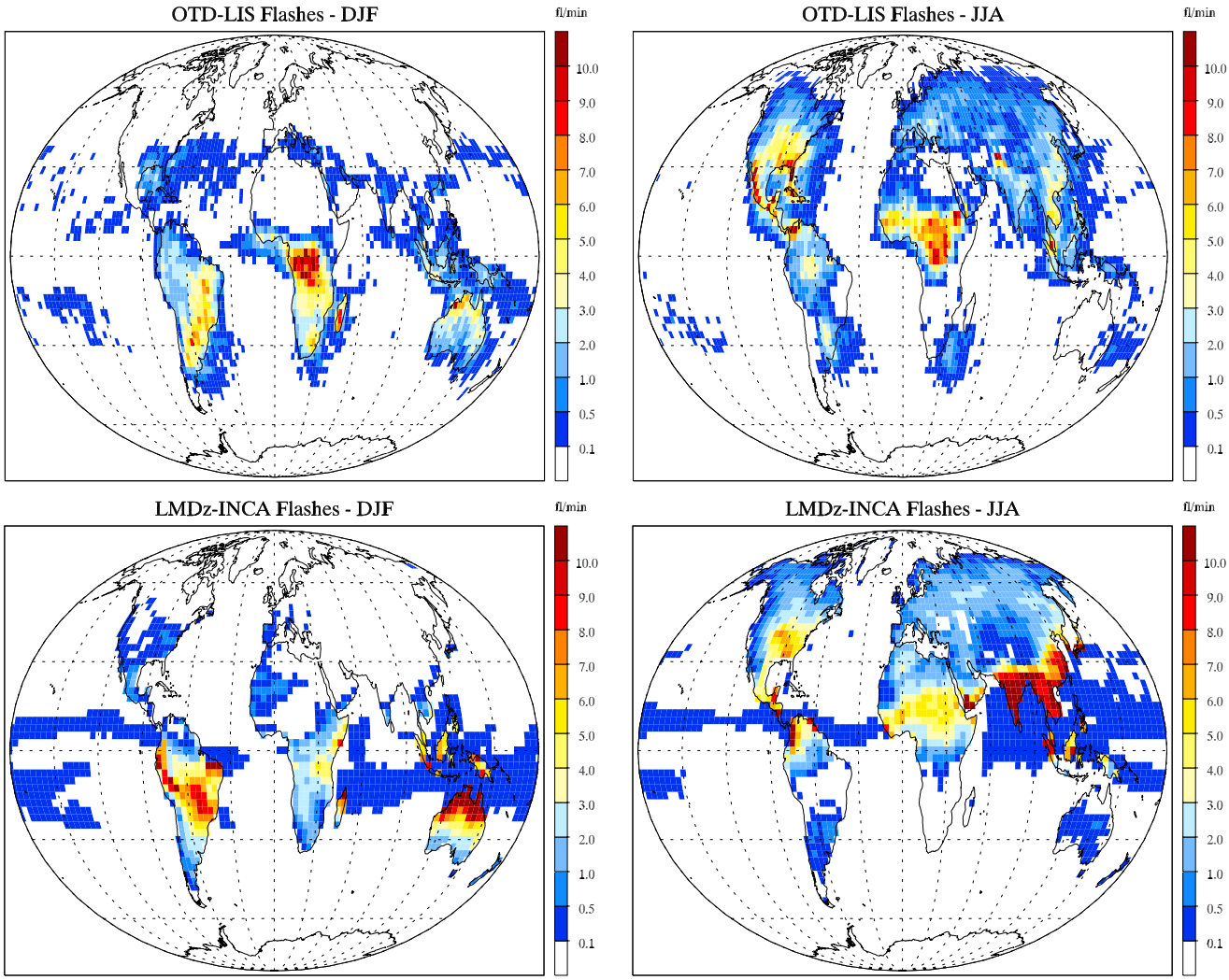


**Figure 8.** Gridded composite of lightning flashes (flashes/min) detected by the LIS (December 1997 to November 2000) and OTD (April 1995 to March 2000) instruments (version 0.1 prepared by *Christian et al.* [2003]) for DJF and JJA conditions (upper panels) and lightning flashes calculated by LMDz-INCA (lower panels).

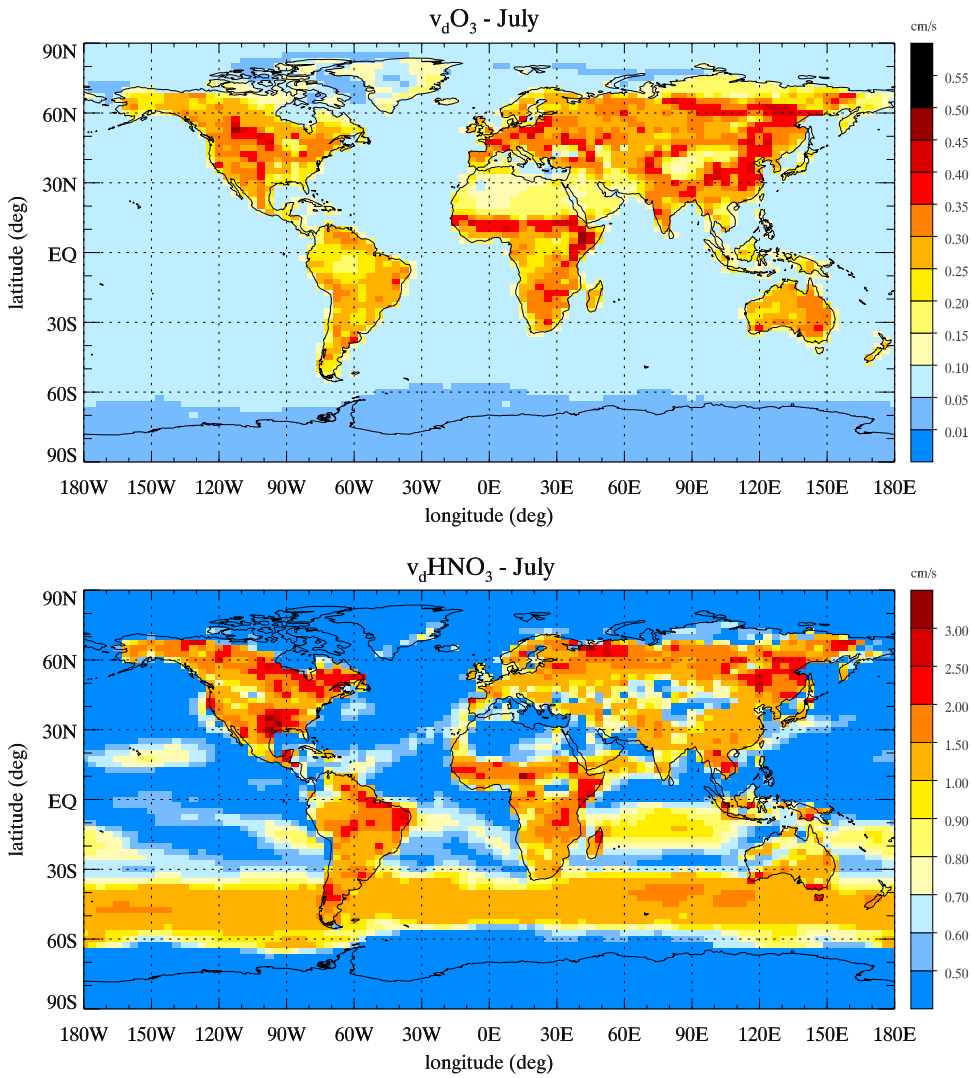


**Figure 9.** Monthly mean $O_3$ and $HNO_3$ surface dry deposition velocity (cm/s) calculated in LMDz-INCA for July conditions.

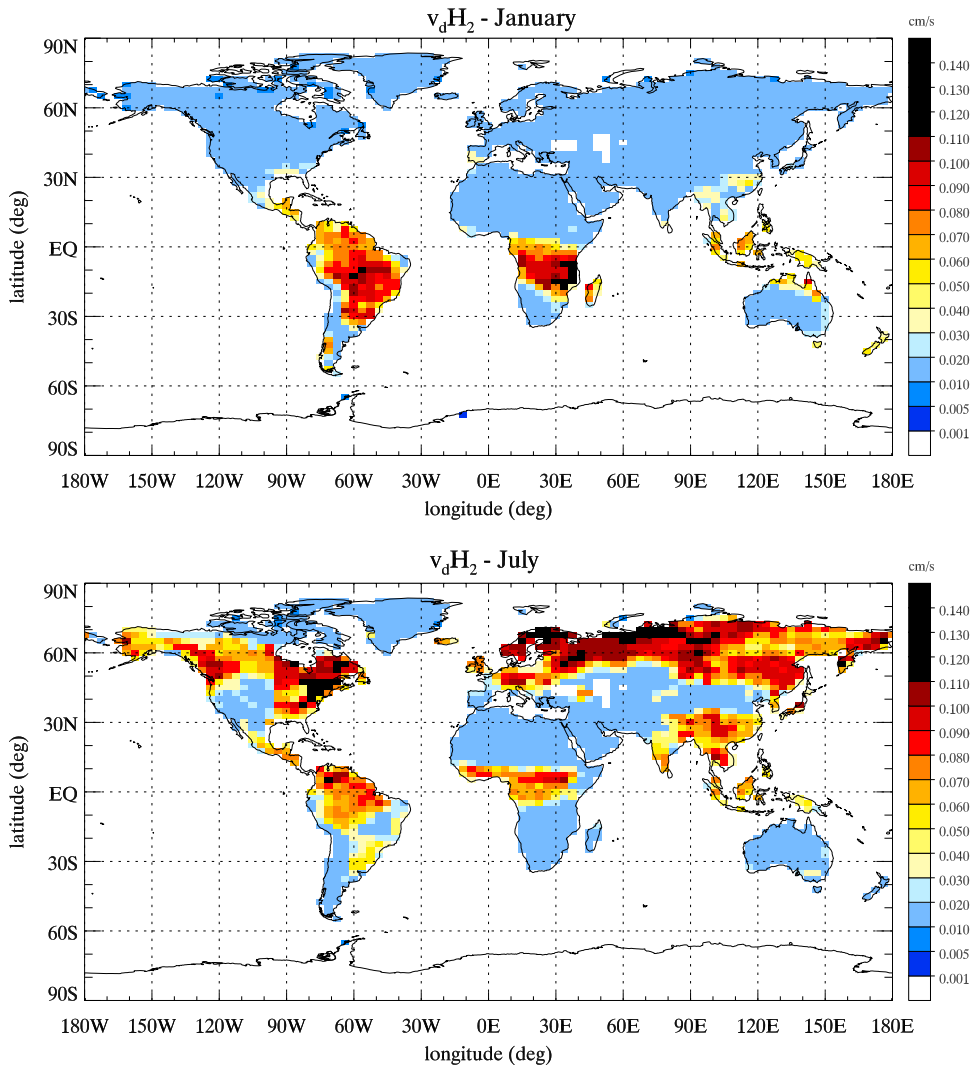


**Figure 10.** Monthly mean $H_2$ surface dry deposition velocity (cm/s) calculated in LMDz-INCA for January and July conditions.

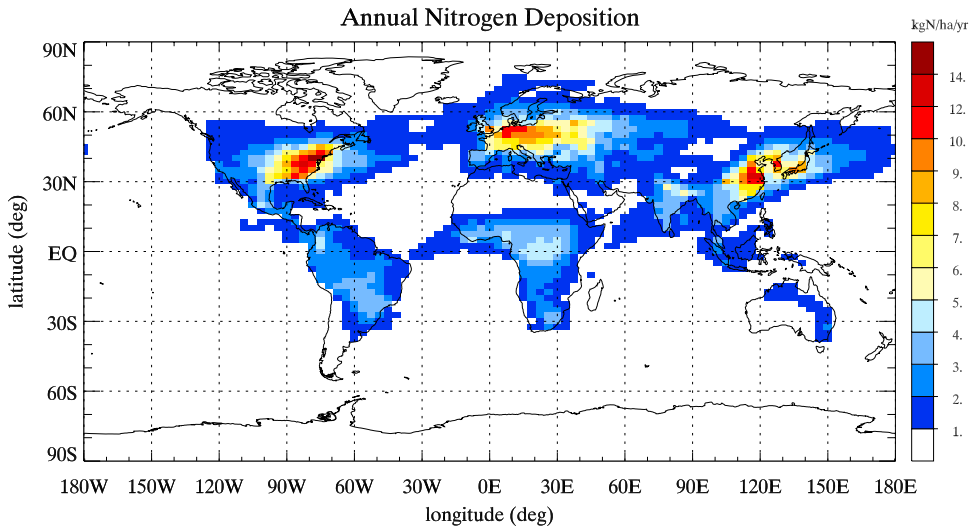


**Figure 14.** Annual and total (wet + dry) nitrogen deposition calculated with LMDz-INCA (kgN/ha/yr).

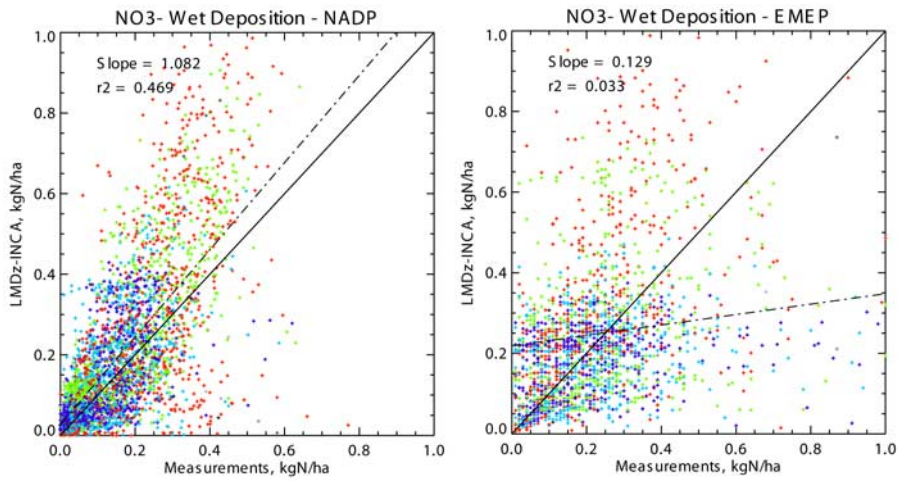


**Figure 15.** Correlation between $NO_3^-$ wet deposition (kgN/ha) calculated with LMDz-INCA and measured from surface networks (measurements reported by Holland et al. (submitted manuscript, 2003)). (left) Northern United States NADP network and (right) Europe EMEP network. The correlation coefficients ($r^2$) and slopes of the linear fit (dashed line) are provided for both regions. Solid line denotes the 1:1 line. Red crosses, summer (JJA) data; light blue, fall (SON); dark blue, winter (DJF); and green, spring (MAM).

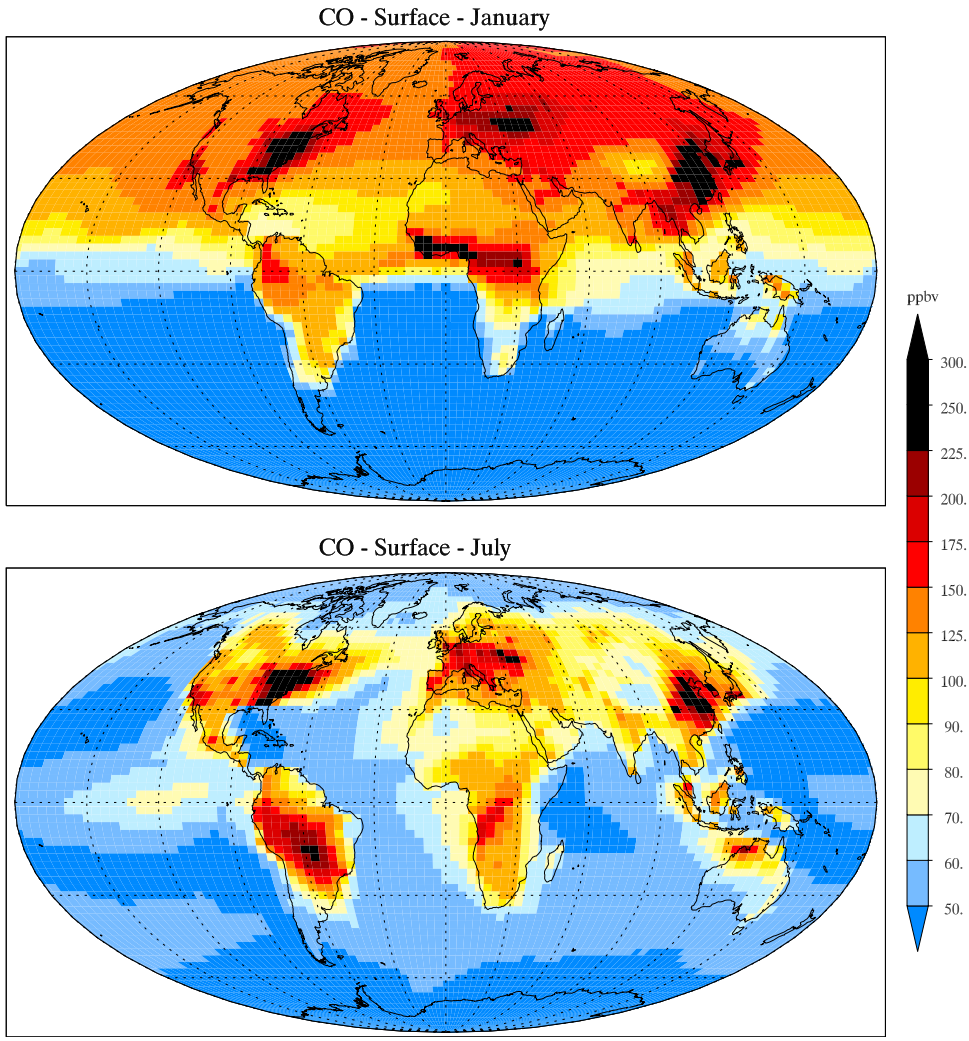


**Figure 21.** Distribution of carbon monoxide (CO) mixing ratio (ppbv) calculated at the surface in January and July.

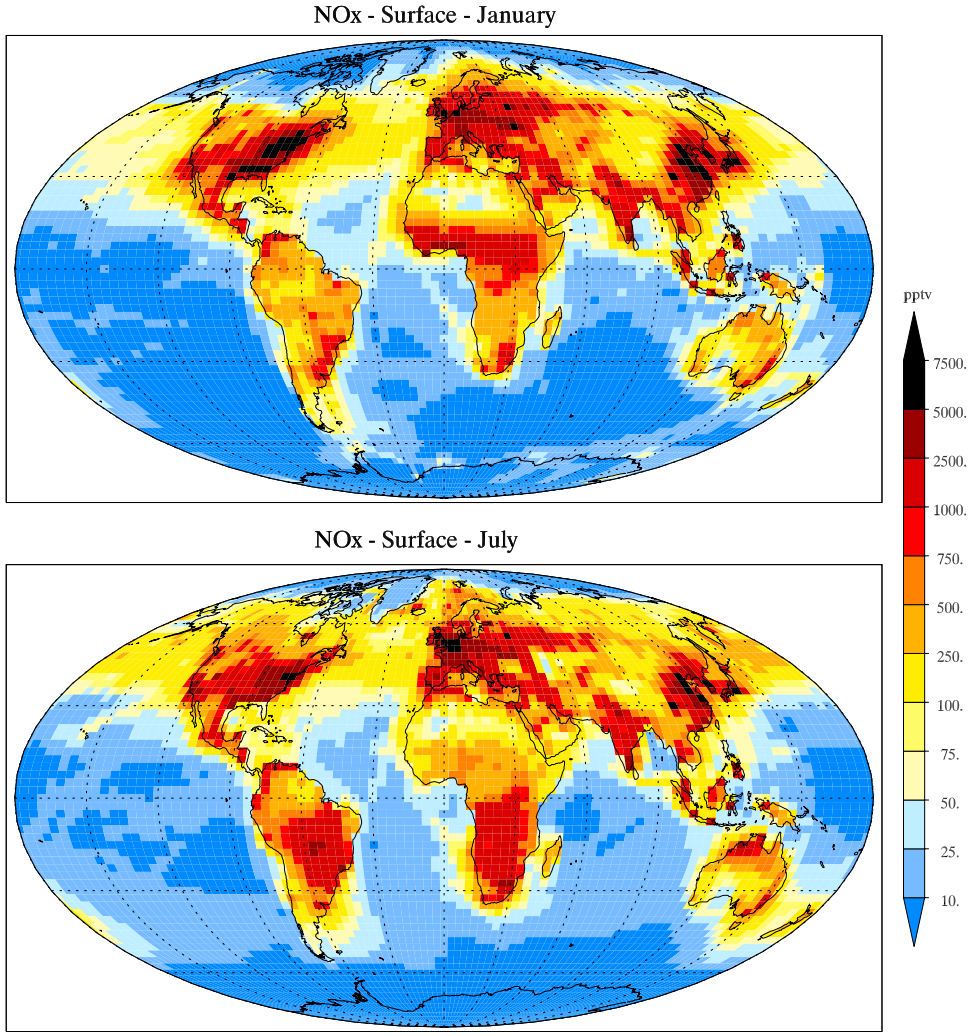


**Figure 24.** Distribution of $NO_x$ mixing ratio (pptv) calculated at the surface in January and July.

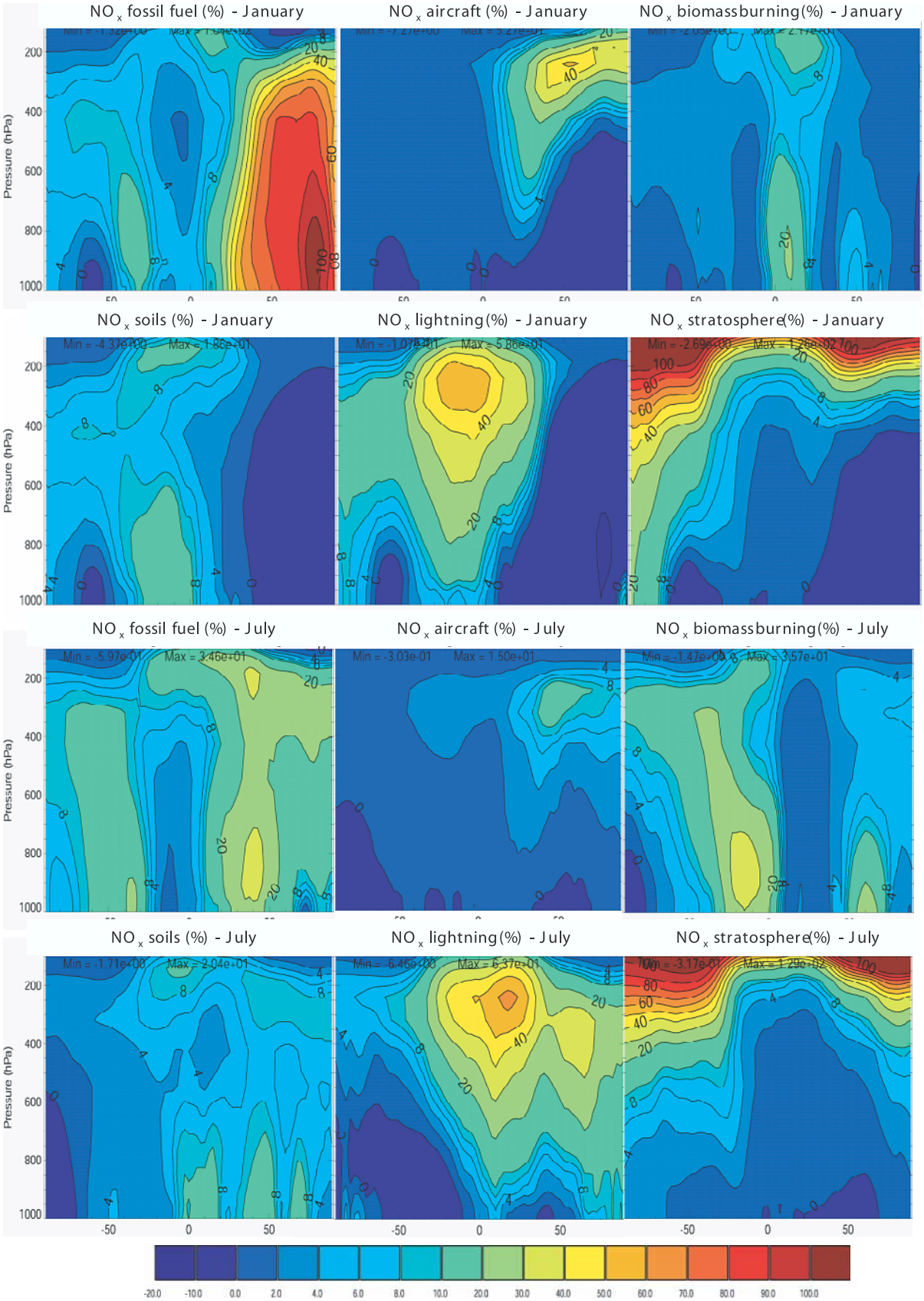


**Figure 27.** Percentage contribution of each individual source to the zonal mean $NO_x$ mixing ratio calculated for January and July conditions.

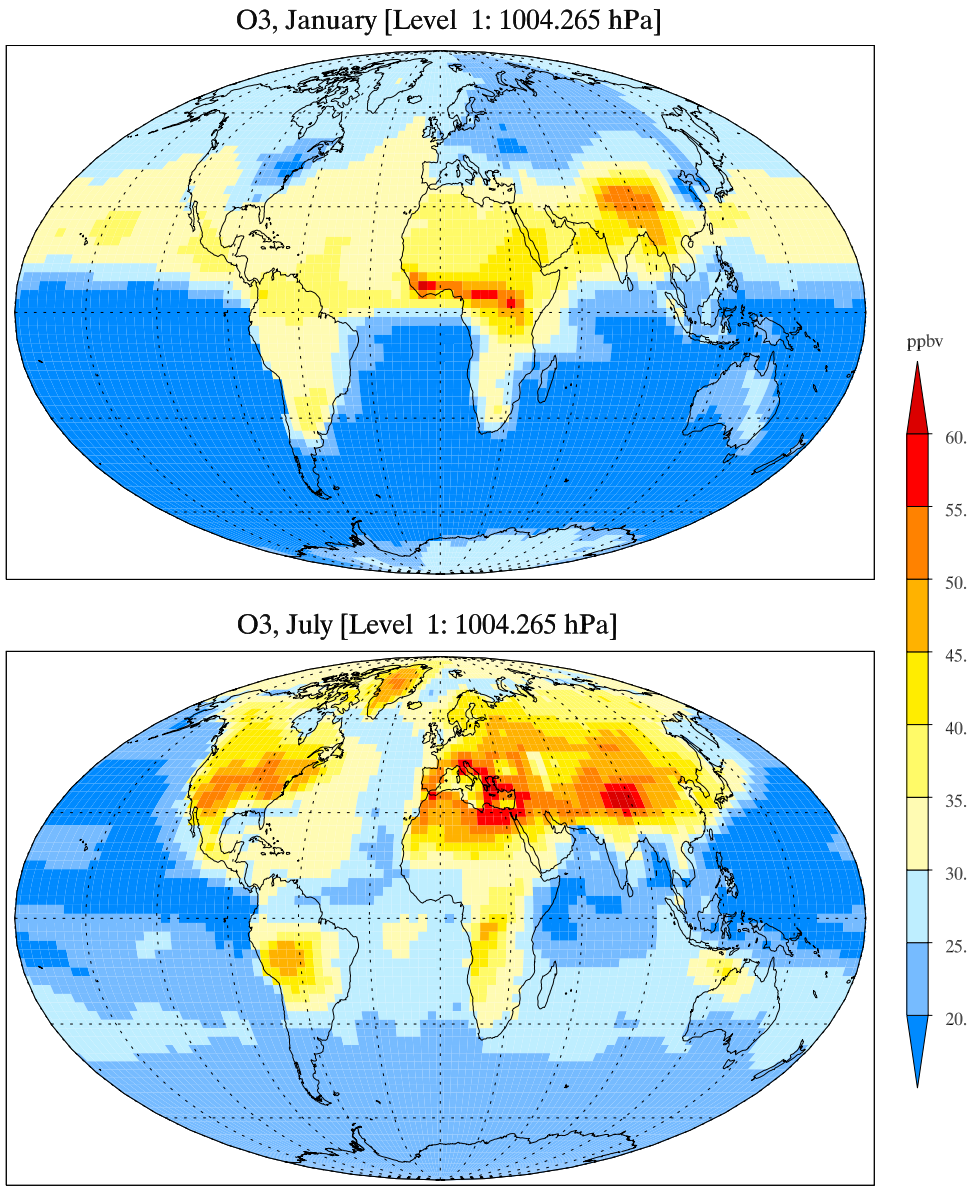


**Figure 28.** Distribution of $O_3$ mixing ratio (ppbv) calculated at the surface in January and July.

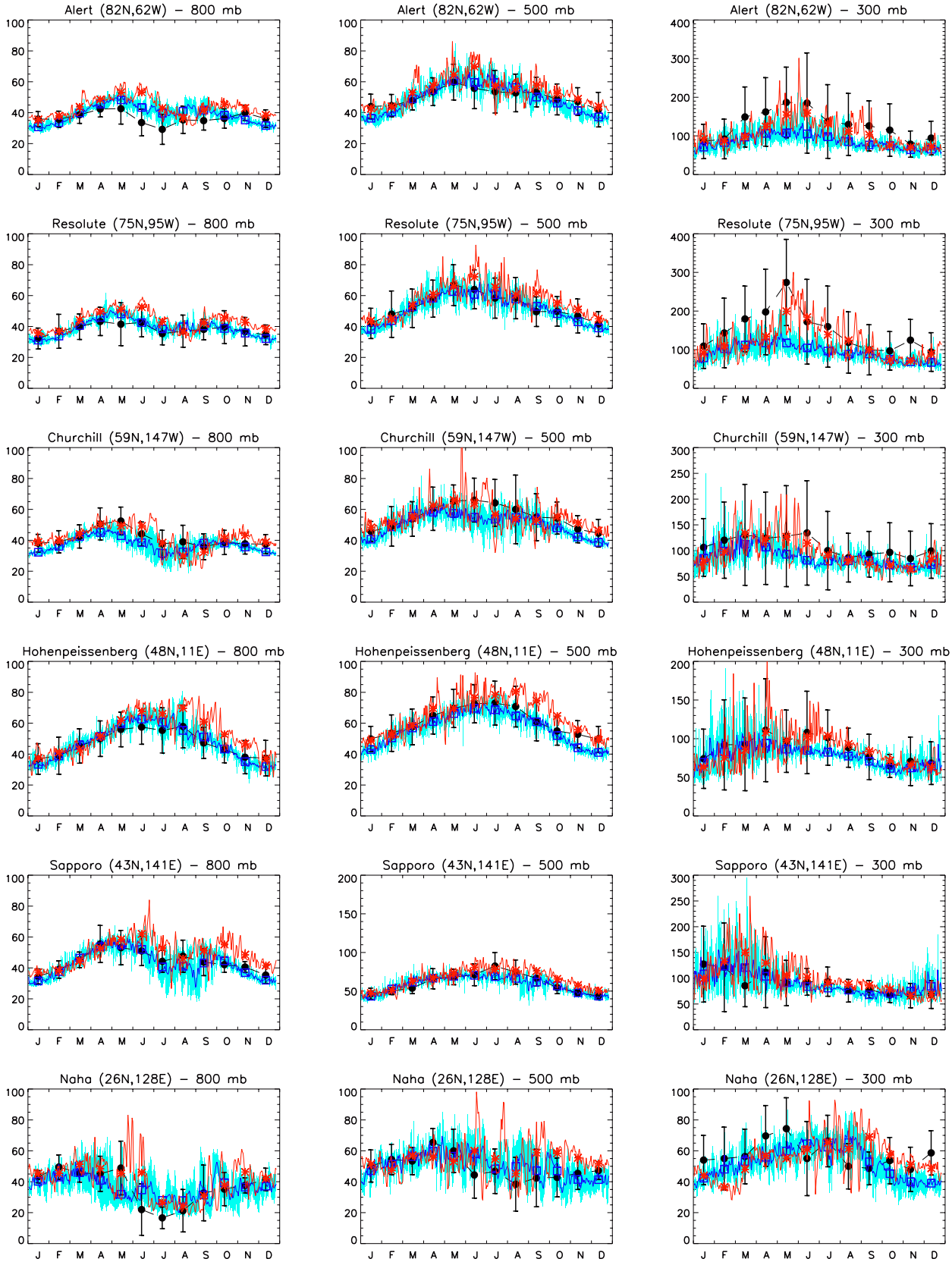


**Figure 32.** Measured (solid circles) and calculated (solid line is day-to-day variation, and crosses denote monthly mean) seasonal cycle of $O_3$ mixing ratio (ppbv) at 12 stations and at 800, 500, and 300 hPa. Blue, base case model simulation; red, simulation with the nudged GCM (year 1997). The shaded blue area provides the day-to-day minimum and maximum ozone mixing ratio over the last 5 years of the simulations. Observations were compiled by *Logan* [1999].

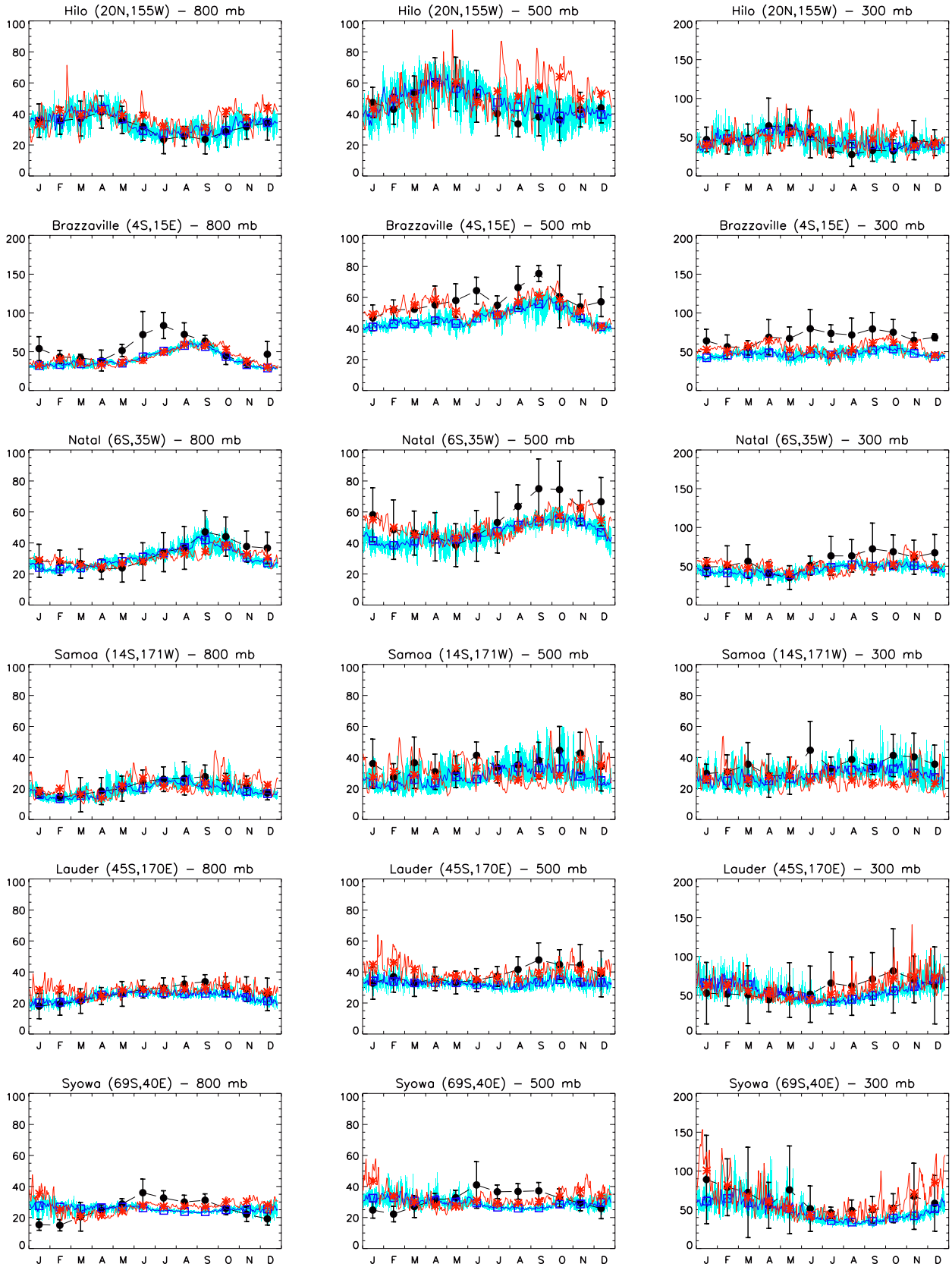


**Figure 32.** (continued)

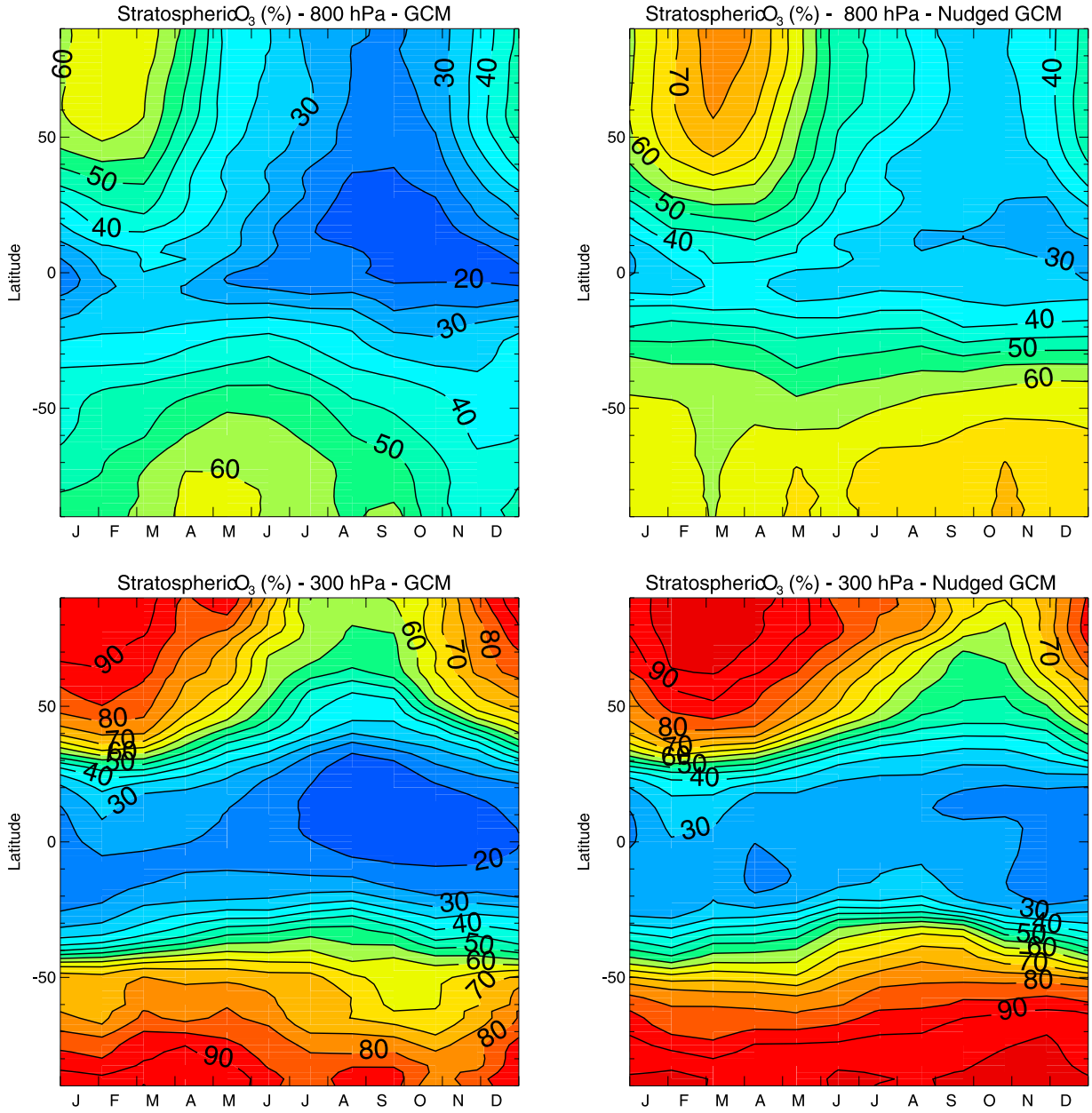


**Figure 33.** Stratospheric contribution to the zonally averaged ozone mixing ratio at 800 and 300 hPa as a function of month (%). (left) Base case GCM simulation; (right) nudged version of the GCM (year 1997).